Dissertation for the Degree of Doctor of Philosophy

A Study on Improving Electrical Characteristics of 2G HTS Field Coils by Metal Insulation Winding Technology for 10 MW Class Wind Generator

Huu Luong Quach

Major of Electrical Engineering
Faculty of Applied Energy System

GRADUATE SCHOOL
JEJU NATIONAL UNIVERSITY

February 2022

A Study on Improving Electrical Characteristics of 2G HTS Field Coils by Metal Insulation Winding Technology for 10 MW Class Wind Generator

Huu Luong Quach
(Supervised by Professor Ho Min Kim)

A dissertation submitted in partial fulfillment of the requirements for the degree of Doctor of Philosophy
2021. 12

This dissertation has been examined and approved

....

Dissertation director, Se Ho Kim, Prof. of Electrical Engineering

Prof. Ho Chan Kim..

Prof. Yeong-Jun Choi...

Dr. Yeong-Hwan Kim...

Prof. Ho Min Kim...

Major of Electrical Engineering
Faculty of Applied Energy System
GRADUATE SCHOOL
JEJU NATIONAL UNIVERSITY

ACKNOWLEDGEMENTS

I would first like to express my deepest gratitude and appreciation to my research supervisor, Prof. Ho Min Kim, for giving me the opportunity to study on the field of superconducting magnet. He has provided consistent support, enthusiastic encouragement, and invaluable guidance during my Ph.D course. His warm advice and motivation have encouraged me during my academic research and writing this dissertation.

I would like to thank the dissertation committee members, Prof. Se Ho Kim, Prof. Ho Chan Kim, Prof. Yeong-Jun Choi, and Dr. Yeong-Hwan Kim who generously reviewed and offered invaluable comments to improve this dissertation.

I would like to extend my thanks to all Professors at the Department of Electrical Engineering, Jeju National University, for giving the background knowledge and sharing their expertise through the amazing and meaningful lectures.

I would also like to acknowledge to my excellent colleagues at the Applied Superconductivity Laboratory, Dr. Ji Hyung Kim, Chang Ju Hyeon, Yoon Seok Chae, Jae Hyung Moon, Jung Hyup Ko, Jung Hyun Hong and Hong Bi Jin, for their valuable discussions and supports. Special thanks to Dr. Ji Hyung Kim and Yoon Seok Chae who always give me useful advices, kind comments, and generous encouragements in both research and life with warm heart. It is a great honour and pleasure for me to work with a team that has tremendous understanding and encouragement during my Ph.D course. I also appreciate staffs and friends in other laboratories at the Department of Electrical Engineering for providing academic information from university and helping me in personal life in Korea.

I am very grateful to all Vietnamese friends in Jeju National University for their helping and spending an interesting time that will be wonderful memories during my Ph.D course in Korea. Special thanks go to my dear friends, Thanh Dung Le and Ngo Phong Nguyen, for their discussions, motivations and encouragements.

Finally, I would like to express my profound gratitude to my parents and sisters for their generous support, love, motivation, and encouragement. Furthermore, I would like to thank my parents–in–law for supporting and taking care of my daughter. Especially, great thanks to my wife, Kim Tuyen Nguyen, who always supports and encourages me with her love to complete this dissertation.

CONTENTS

ACKNOWLEDGEMENTS .... **i**

CONTENTS .... **iii**

ABSTRACT .... **v**

LIST OF FIGURES .... **ix**

LIST OF TABLES .... **xi**

LIST OF ABBREVIATIONS .... **xii**

Chapter 1. Introduction **1**

1.1 . Background and motivation of the study 1

1.2 . Objectives of the study 7

1.3 . Outline of the study 8

Chapter 2. Winding Technology and Equivalent Circuit Model for 2G HTS Magnet ... **10**

2.1. Winding technology for 2G HTS magnet 10

2.1.1. No–insulation winding technique 11

2.1.2. Partial insulation winding technique 14

2.1.3. Metal cladding winding technique 16

2.2. Metal insulation winding technique 17

2.3. Equivalent circuit model for 2G HTS magnet 19

2.3.1. Steady state characteristic analysis 21

2.3.2. Transient state characteristic analysis 26

Chapter 3. Fabrication and Experiment of 2G HTS Magnet **28**

3.1. Fabrication and experiment of NI pancake coil 28

3.1.1. Experiment setup 29

3.1.2. Results and discussion 32

3.2. Fabrication and experiment of NI and MI–SS racetrack coil 39

3.2.1. Experiment setup 42

3.2.2. Results and discussion 42

3.3. Fabrication and experiment of MI–SS racetrack coils according to various winding tension and stainless steel insulation thickness 51

3.3.1. Experiment setup 51

3.3.2. Results and discussion 54

3.4. Fabrication and experiment of MI–SS racetrack coil according to various AC rotating magnetic field and cryogenic cooling system 66

3.4.1. Experiment setup 67

3.4.2. Results and discussion 72

Chapter 4. Analysis on Electrical Characteristics of MI–SS 2G HTS Field Coils for 10 MW Class Wind Generator 87

4.1. Parameters of 2G HTS field coil 87

4.2. Results and discussion 88

4.2.1. Charging test 88

4.2.2. Overcurrent test 90

Chapter 5. Conclusions 93

REFERENCES 96

CURRICULUM VITAE 103

ABSTRACT

A Study on Improving Electrical Characteristics of 2G HTS Field Coils by Metal Insulation Winding Technology for 10 MW Class Wind Generator

Second generation (2G) high temperature superconducting (HTS) coils have recently attracted increasing attention of many researchers in developing high performance superconducting application because they possess high current density under high magnetic field and high stability margin compared with their low temperature counterparts. This technology could be considered as an effective solution to develop large–scale offshore wind turbine generators. The 2G HTS magnets for wind turbine generators, in form of racetrack type coils, can achieve higher magnetic field than permanent or resistive magnets. However, protection of the 2G HTS coil is well known to be one of the challenging problems for reliability of operation of HTS magnet applications because of the low normal zone propagation velocities that is incurred by the low index numbers and large specific heat.

The no–insulation (NI) winding technique has been introduced to develop 2G HTS magnets with significantly enhanced thermal stability resulting from self–protection characteristic. The main idea behind this technique is based on the elimination of the turn–to–turn insulation layers in the HTS coil. During quenching, excessive current can be automatically diverted through neighboring turns; thus, a 2G HTS magnet can remain stable at a higher current density. However, the decay time constant can be a major challenge for the NI coil due to the bypass current phenomenon, which is caused by the absence of insulation resistance. The bypass current flows through the turn–to–turn contact under time–varying condition, leading to a slow charging delay time (τ_d) of the NI coil. As a result, the application of the NI winding technique is limited to devices that require fast electromagnetic responses, such as superconducting rotating machines and superconducting magnetic energy storage systems.

Recently, the metal insulation (MI) winding technique, which employs metal insulation between the turn–to–turn layers, has been suggested as a promising solution to overcome the drawback in slow τ_d of NI winding technique. Several research groups have been studied MI coil in the steady and transient states to investigate the electromagnetic response and thermal stability, respectively. The results demonstrated that the MI coil achieved both fast τ_d under time–varying condition and high thermal stability during the overcurrent test. However, these studies have been performed mostly in pancake type coils. Therefore, to utilize the MI winding technique for the field coils of superconducting rotating machines, it is necessary to estimate the τ_d as well as thermal stability behaviors of the MI winding technique which is wound in form of racetrack type coils.

In this dissertation, the electrical characteristics of MI–SS racetrack coil under the steady and transient states were estimated in both experiment and simulation. In addition, the effects of stainless steel thickness, winding tension, cooling approach, and rotating magnetic field on the τ_d and thermal stability were also investigated. The results of this dissertation can be used as a technical reference for development the potential 2G HTS field coils, i.e., enhancing τ_d as well as thermal stability, of a 10 MW class HTS generator used in offshore wind turbine environment. First, an electrical equivalent circuit model was proposed to numerically analyze the characteristics of the NI 2G HTS coil in steady and transient states. A steady state was performed under rated operating current shooting to estimate the magnetic field response performance of the NI HTS coil. The transient state was conducted under an overcurrent shooting to analyze the thermal quench behavior. The simulation results of the NI HTS coil were discussed and compared with the experimental ones to validate the simulation approach based on the proposed equivalent circuit model. Then, the NI and MI–SS racetrack coils were performed in both experiment and simulation to estimate the magnetic field response in the steady state and thermal stability in the transient state. The results demonstrated that the MI–SS racetrack coil can be charged considerably faster than that of NI racetrack coil. During the overcurrent, the MI–SS racetrack coil operated successfully to protect the test coil from burn–

out because a portion of excessive current can automatically diverted through the stainless steel tape layers. The stainless steel thickness and winding tension are identified as the factors affecting the τ_d and thermal stability of MI–SS coils. To verify these characteristics, three types of MI–SS racetrack coils were fabricated with various SS thicknesses and winding tensions: 100–μm SS thickness and 10–kgf winding tension; 100–μm SS thickness and 5–kgf winding tension; and 50–μm SS thickness and 10–kgf winding tension. Three MI–SS racetrack coils were characterized by sudden discharging, charging, and overcurrent tests. The sudden discharging and charging tests were performed in a steady state to investigate the decay time constant of the center magnetic field discharging the coils and the delay time of the magnetic field charging the test coils, respectively. To estimate the thermal stability of the three MI–SS coils, overcurrent tests were conducted in a transient state. In addition, the MI–SS racetrack coil was tested under various cryogenic cooling conditions and rotating magnetic fields to analyze the electrical and thermal characteristics because the 2G HTS field coils can be exposed to rotating magnetic fields in practical wind generator application which caused by unsynchronized armature windings during electrical or mechanical load fluctuations. The cooling and vacuum tests were conducted to setup operating temperature for the conduction cooling system at 35 and 77 K. Then, the charging and discharging tests were carried out to investigate the effect of cooling approaches, i.e, LN2 bath and conduction cooling conditions, to the characteristic resistance and magnetic field response performance. To evaluate the effect of external magnetic field on I_c and thermal stability characteristics of the MI–SS racetrack coil, the transient test was performed under rotating magnetic field, which was generated by armature windings of 75 kW class induction motor, and conduction cooling system of 35 K. Furthermore, based on the experimental results of small–scale MI–SS racetrack coils, the total contact resistance between turn–to–turn layers of the test coils was calculated and applied to design the field windings using 2G HTS tape for the 10 MW class HTS generator used in offshore wind turbine environment. Subsequently, a proposed equivalent circuit model was utilized to analyze the electromagnetic response and thermal stability characteristics of MI–

SS 2G HTS field coils for the 10 MW class HTS generator. Finally, the τ_d and thermal stability of these MI–SS 2G HTS field coils were compared and analyzed in detail.

LIST OF FIGURES

Fig. 1.1. Critical surface condition of superconductor. 1

Fig. 1.2. Magnetization of external magnetic field for Type I and II superconductors. 3

Fig. 1.3. The chronological discovery of superconductors and their critical temperature. 4

Fig. 2.1. Structure of 2G HTS coated conductor. 10

Fig. 2.2. Current flowing characteristic during quench. 12

Fig. 2.3. Experiment results for INS (coil 1) and NI (coil 2). 13

Fig. 2.4. Current flowing characteristic of PI HTS coil during quench. 15

Fig. 2.5. Experiment results of NI (coil 1), PI every five turns (coil 2), and INS (coil 3). 15

Fig. 2.6. Schematic drawings of (a) 2G HTS and (b) MC 2G HTS tapes. 16

Fig. 2.7. Experimental results of MC, PI 3, PI 6, and PI 9 HTS coils. 17

Fig. 2.8. Schematic drawings of the MI HTS pancake coil. 18

Fig. 2.9. Experiment results of INS, MI, and NI HTS coils. 18

Fig. 2.10. Equivalent circuit model for HTS coils. 20

Fig. 2.11. Two sections of input current during the charging test process. 23

Fig. 3.1. HTS winding machine. 31

Fig. 3.2. Photographs of the NI SPC. 31

Fig. 3.3. Critical current test of NI HTS coil. 32

Fig. 3.4. Results of normalized B_z and I_t during sudden discharging test. 33

Fig. 3.6. Results of V_t, B_z, and current in the transient state. 37

Fig. 3.7. Experimental and simulation results of heat generation. 38

Fig. 3.8. (a) Design model of racetrack bobbin; photograph of (b) NI and (c) MI–SS coils. .40

Fig. 3.9. I–V characteristics at 77 K with current ramp rate of 0.5 A/s. 43

Fig. 3.10. Sudden discharging test results at 0.7 I_c with charging rate of 1 A/s. 44

Fig. 3.11. Charging test results of NI coil at 0.6 I_c with charging rate of 1 A/s. 46

Fig. 3.12. Charging test results of MI–SS coil at 0.6 I_c with charging rate of 1 A/s. 47

Fig. 3.13. Overcurrent test results of NI coil at 1.1 I_c with charging rate of 0.5 A/s. 49

Fig. 3.14. Overcurrent test results of MI–SS coil at 1.1 I_c with charging rate of 0.5 A/s. 50

Fig. 3.15. Photograph of MI–SS racetrack coils. 52

Fig. 3.16. Critical current values at 77 K with current ramp rate of 1 A/s............................55

Fig. 3.17. Sudden discharging tests at 0.7 I_c with current ramp rate of 1 A/s. 56

Fig. 3.18. Charging tests at 0.6 I_c with current ramp rate of 1 A/s. 58

Fig. 3.19. Charging tests at 0.6 I_c with current ramp rate of 5 A/s. 60

Fig. 3.20. Charging tests at 0.8 I_c with current ramp rate of 1 A/s. 62

Fig. 3.21. Overcurrent tests at 1.1 and 1.05 I_c with current ramp rate of 1 A/s.....................64

Fig. 3.22. Photographs of MI–SS racetrack coil. 69

Fig. 3.23. Photographs of assembly MI-SS racetrack coil into conduction cooling system...70

Fig. 3.24. Schematic drawings of cryostat part with position of temperature sensors. 70

Fig. 3.25. Photographs of assembly cryostat part into induction motor. 71

Fig. 3.26. Photographs of experiment setup. 71

Fig. 3.27. Experiment results under cooling and vacuum tests...72

Fig. 3.28. Critical current results of MI–SS racetrack coil. 74

Fig. 3.29. Reduction of I_c value according to perpendicular flux density 76

Fig. 3.30. Simulation critical current results of MI–SS racetrack coil. 76

Fig. 3.31. Time constant results of MI–SS racetrack coil at 221 A. 78

Fig. 3.32. Charging delay time results of MI–SS racetrack coil at 221 A. 80

Fig. 3.33. Temperature results of MI–SS racetrack coil at 221 A. 81

Fig. 3.34. Test results of MI–SS racetrack coil under external magnetic field. 83

Fig. 3.35. Temperature results of MI–SS racetrack coil under external magnetic field. 84

Fig. 4.1. Charging test at 0.6 I_c with current ramp rate of 1 A/s. 89

Fig. 4.2. Overcurrent tests at 1.2 I_c with current ramp rate of 1 A/s....................................91

LIST OF TABLES

Table 3.1. Parameters of 2G HTS tape and NI HTS coil. 30

Table 3.2. Parameters of 2G HTS tape and two racetrack coils. 41

Table 3.3. Parameters of 2G HTS tape and three racetrack type coils. 53

Table 3.4. Effects of winding tension and SS thickness on the charging time of MI–SS racetrack coils. 59

Table 3.5. Effects of current ramp rate on charging time of MI–SS racetrack coils. 61

Table 3.6. Effects of current amplitude on charging time of MI–SS racetrack coils. 63

Table 3.7. Effects of winding tension and SS thickness on the thermal stability of MI–SS racetrack coils. 65

Table 3.8. Parameters of REBCO tape and MI–SS racetrack coil. 68

Table 3.9. Experiment results of the test coil under LN2 and conduction cooling. 79

Table 3.10. Temperature results of MI–SS racetrack coil under external magnetic field. 86

Table 4.1. Key parameters of three HTS field coils. 88

LIST OF ABBREVIATIONS

LTS	Low temperature superconducting
HTS	High temperature superconducting
1G	First generation
2G	Second generation
PIT	Powder in tube
LN2	Liquid nitrogen
SMES	Superconducting magnetic energy storage
NMR	Nuclear magnetic resonance
MRI	Magnetic resonance imaging
NZPV	Normal zone propagation velocity
INS	Insulation
NI	No–insulation
PI	Partial insulation
MC	Metal cladding
MI	Metal insulation
SS	Stainless steel
REBCO	Rare–earth barium copper oxide
DC	Direct current
SPC	Single pancake coil
DAQ	Data–acquisition
FEA	Finite element analysis

Chapter 1. Introduction

1.1. Background and motivation of the study

Superconductivity is a phenomenon in which the electrical resistivity of specific material abruptly drops to zero at its critical temperature (T_c). In 1911, Kamerlingh Onnes experimentally discovered this phenomenon in mercury at liquid helium temperature of 4.2 K. In addition to T_c, superconductivity is also governed by two other parameters, such as critical current density (J_c) and critical magnetic field (H_c). Fig. 1.1 demonstrates the typical critical surface condition in phase space of a superconductor [1]. A material remains only in the superconducting state when these three critical factors are presented by points within the boundary region below the critical surface (gray color area in Fig. 1.1) and the superconductor reverts to its normal state outside this region.

Based on the magnetic behavior, superconductors can be classified into Types I and II. Type I superconductors are usually pure metal and generally characterized by an abrupt transition

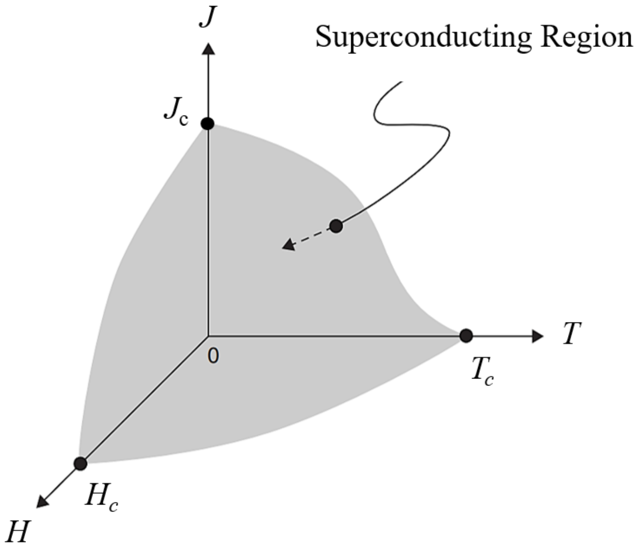

Fig. 1.1. Critical surface condition of superconductor.

from the superconducting state to the normal state. Type I superconductors, also known as soft superconductors, have only one H_c. If the external magnetic field $H < H_c$, the superconductor is perfect diamagnetism and the magnetization is equal and opposite in direction to the external magnetic field. Thus, the magnetic field inside the superconductor is zero. When the external magnetic field increases to the H_c and beyond, the superconductor returns into the normal state. On the other hand, type II superconductors are alloys and compounds which have two critical magnetic fields, such as lower critical magnetic field H_{c1} and upper critical magnetic field H_{c2}. As the applied magnetic field is smaller than H_{c1}, the characteristics are similar to that of type I superconductors. Above H_{c1}, the type II superconductors are in the mixed state where there is a partial flux that can penetrate inside the superconductor. For the applied field higher than H_{c2}, the type II superconductors are locally destroyed and the material completely enters to the normal state. Fig. 1.2 illustrates the plots of magnetization (M) as a function of external magnetic field for Type I (solid curve) and Type II (dashed curve). Type I superconductors are not useful for the practical electric power applications due to low H_c, typically less than 0.1 T. Unlike the type I superconductors, the type II superconductors have high values of the H_{c2}, making them widely used in manufacturing for superconducting magnetic applications [2]–[4]. Type II superconductors are classified into low–temperature superconductors (LTS) and high–temperature superconductors (HTS) according to their critical temperature. The first of HTS conductors began in the 1986 with the famous discovery of superconductivity at 35 K by Muller and Bednorz in the system Ba–La–Cu–O. Then, the compound Y–Ba–Cu–O was found to become superconducting at 93 K by group researcher led by Paul Chu from the University of Houston in 1987. The detail timeline of T_c development in superconducting materials are shown in Fig. 1.3 [5]. The discovery of HTS superconductors presented a huge challenge but also the opportunity of applying superconductivity to electric power and electronics industries which are not possible with conventional technology. HTS conductors refer to Bi–based and Re–based materials which correspond to first generation (1G) and second generation (2G) HTS conductors, respectively. The 1G HTS conductors are fabricated by adding interstitial

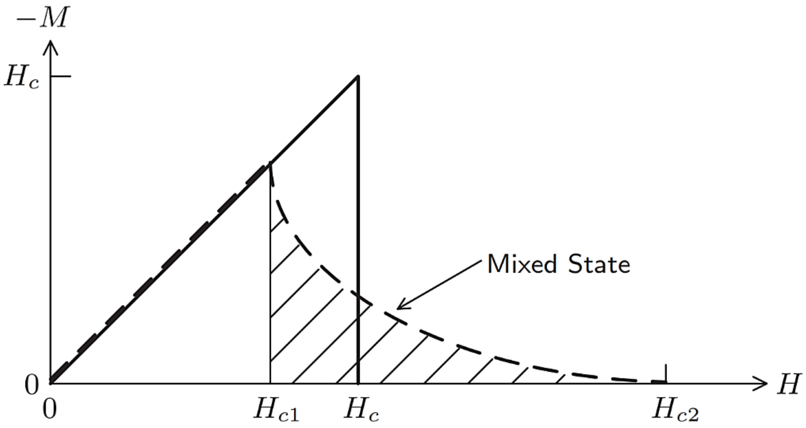

Fig. 1.2. Magnetization of external magnetic field for Type I and II superconductors.

oxygen atoms to the copper oxide plane which can be done into wires via the Powder In Tube (PIT) technology. Unlike the 1G HTS, the coated conductor technology, i.e., deposition of 2G HTS materials on metal tapes coated with buffering metal oxides, is utilized to manufacture 2G HTS conductors because the PIT technology does not produce good results. HTS conductors exhibit superconducting behavior at much higher temperature than LTS conductors. Therefore, HTS conductors require less cooling and can operate at the temperature of 77 K, which is achieved with inexpensive liquid nitrogen (LN2). Furthermore, HTS conductors have the ability to sustain high current densities in high magnetic fields. The promise of high current densities of HTS conductors as well as reasonably priced refrigeration systems have been proposed this technology to power applications, such as superconducting magnetic energy storage (SMES) systems, transformers, power cables, fault current limiters, superconducting machines, nuclear magnetic resonance (NMR), and magnetic resonance imaging (MRI) systems [1]–[5].

Wind turbines with large power capacity, high reliability, and low cost have been required to meet the rapidly increasing demand for clean energy across the market. With high wind energy absorption at the sea level, the huge speed–up gearbox is a complex problem of offshore wind turbines which causes serious difficulties in both energy wasting mechanical part and stability degradation. Direct–drive train wind turbines are considered as the most promising

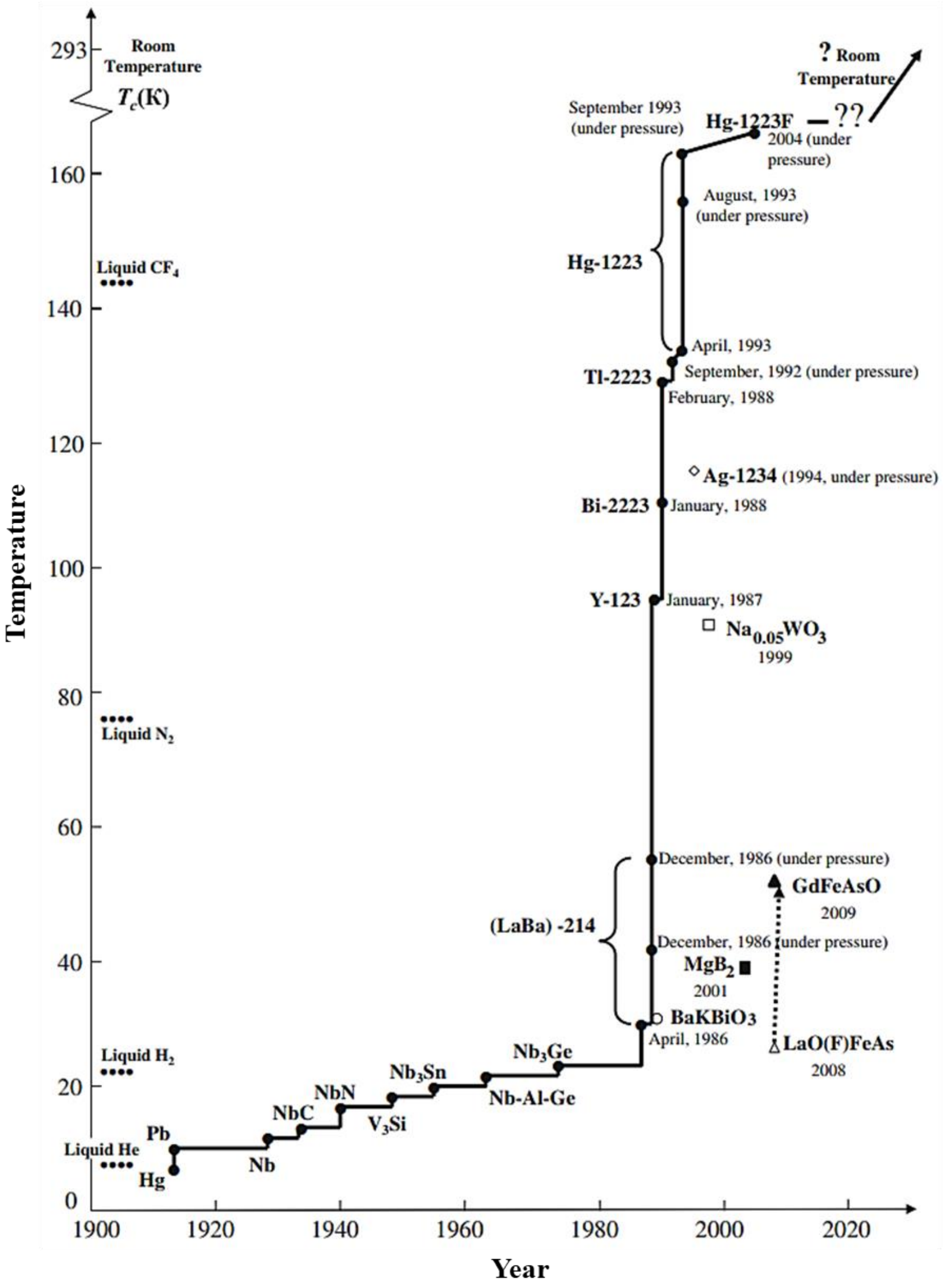

Fig. 1.3. The chronological discovery of superconductors and their critical temperature.

candidate because they have an improvement in the overall reliability, efficiency, and better scalability by removing the gearbox and replacing it with a simple mechanical system that is not sensitive to the fluctuation of the shaft torque. The Direct–drive generator concepts are operated at the very low speed of the turbine rotor; thus high torque is demanded. However, the size and mass of a permanent direct–drive wind generator increases with an increase of power capacity which are difficult to install and replace in practical applications, especially for multi–MW wind turbines. The weight of 10 MW direct–drive permanent magnet generators have been estimated above 300 ton and their diameters are larger than 10 m [6], [7]. The huge size and heavy weight of the wind turbine generator always accompany with high cost of the foundation, transportation, installation, operation, and maintenance. Therefore, many research institutes and companies have recently been studied to develop a wind power generator with high capacity, light weight, and small size with reasonable cost.

Recently, the 2G HTS coated conductor tape is considered as the promising prospect to develop high magnetic field, i.e., 2G HTS field coils, for power electrical applications due to the development technology of 2G HTS tape in terms of long length and high critical current. The HTS synchronous direct–drive generators using 2G HTS excitation field winding are considered as a new solution for a 10 MW class and beyond wind turbine. The HTS generators are expected to achieve compact design, small volume, low mass, and high power generation efficiency because the 2G HTS field coils provide higher current density, higher air gap magnetic field, and higher induced voltage in the armature windings compared with the conventional copper and permanent magnet based generators. For these reasons, the HTS generators can remove a part of the iron core and copper armature windings, consequently reducing the cost in terms of the construction, transportation, and installation of wind turbines. Thus, several works have been studied on the design for the 10 MW class HTS generator and beyond by using the 2G HTS racetrack coils for the excitation field winding [8]–[17]. In general, the stability of HTS generator systems using the conventional insulation winding technique (INS), which is wound with the organic material insulation (i.e., Kapton and Nomex between turn–to–turn layers), for the excitation field winding are degraded in the transient state, due to low normal zone propagation velocity (NZPV) in the 2G HTS wires that is incurred by the low index numbers and large specific heat [18]–[21]. For that reason, expecting a self–protection performance of LTS coils becomes more difficult to achieve than in case of 2G HTS coils. Therefore, an additional protection should be utilized to ensure a reliable operation of 2G HTS field coils for the 10 MW class HTS generator in the event of quench, leading to the complex systems in the wind turbine power. Many researchers have presented and studied no–insulation (NI) winding technique by eliminating the insulation between turn–to–turn layers in the 2G HTS coils to develop compact and mechanically robust 2G HTS magnets with significantly enhanced stability due to its self–protection characteristic [22]–[37]. During quench, the excessive heat and current could be automatically diverted through the neighboring turns from its original spiral direction, and thus the 2G HTS magnets can stay stably at higher current density. Although the results showed that the NI winding method has a higher potential for the improvement of electrical and thermal stabilities compared to its insulated counterpart, it suffers from the disadvantage of a delayed response time, i.e., a charging/discharging delay of the target magnetic field under time–varying condition, due to the absence of insulation resistance [38]–[42]. This problem becomes a serious issue in terms of large–scale 2G HTS magnets. Thus, both INS and NI coils are difficult to use in electrical devices that require fast controllability and high thermal stability, especially in 2G HTS field coils of the 10 MW class HTS generator. Several methods have been proposed to overcome the disadvantages of INS and NI coils in electrical characteristics, i.e., partial insulation (PI), metal cladding (MC), and metal insulation (MI). However, the MI winding technique exhibited a good trade–off among the charging delay time (τ_d), thermal stability, and the ease of winding process compared with PI and MC winding techniques. Therefore, this dissertation proposes the MI winding technique for fabrication 2G HTS field coils of the 10 MW class HTS generator. The proposed method applies stainless steel (SS) material insulation between turn–to–turn layers to achieve not only the fast electromagnetic response of INS winding technique but also high thermal stability of NI winding technique.

1.2. Objectives of the study

The main objective of this dissertation is to study a suitable winding technique to enhance the performance of the magnetic field response as well as the thermal stability of 2G HTS field coils for the 10 MW class HTS generator used in offshore wind power environment. The MI winding technique has been suggested as a promising solution to overcome the aforementioned problems of NI and conventional INS winding methods due to increasing the characteristic resistance by increasing the contact surface resistance between turn–to–turn layers. To date, the benefits of MI winding technique in terms of the electromagnetic response and thermal stability have been reported mostly in pancake type coils by several research groups. There is insufficiently study to analyze the electrical characteristics for 2G HTS racetrack type coils in the steady and transient states. Therefore, this dissertation investigates the electrical features of MI–SS racetrack coils and other factors which can effect to the performance of the τ_d and thermal stability, such as current ramp rate, current amplitude, winding tensions, SS thicknesses, cooling approach, and rotating magnetic field. First of all, the simulation approach of both analytical and numerical methods were developed, which were based on the proposed equivalent circuit mode, to evaluate the τ_d and the joule heat generation inside the 2G HTS coils. In addition, the NI pancake type coil was manufactured to investigate the magnetic field response performance under a steady state operation with rated current charging as well as the thermal stability under a transient state operation with overcurrent charging. In order to validate the simulation approach, the simulation results of the NI pancake coil were compared and discussed with the experiment ones. Then, small–scale MI–SS and NI racetrack type coils were fabricated to investigate the τ_d and thermal stability under the steady and transient states, respectively. The experiment and simulation results showed that the MI–SS racetrack coil possesses a good balance between the τ_d and thermal stability compared to the NI racetrack coil. In addition, the effects of winding tensions and SS thicknesses between turn–to–turn layers on the electrical characteristics of the MI–SS racetrack coils were also analyzed and discussed in detail. Furthermore, the MI–SS racetrack coil was tested under various rotating magnetic fields and cryogenic cooling conditions to estimate the electrical and thermal characteristics. From the experimental results of three small–scale MI–SS racetrack coils, the contact surface resistances were calculated and employed into 2G HTS field coils of the 10 MW class HTS generator. Subsequently, τ_d and thermal stability of MI–SS 2G HTS field coils were investigated by using the proposed equivalent circuit model and the key parameters of the 10 MW class HTS generator.

1.3. Outline of the study

The organization of this study consists of the following contents:

Chapter 1 gives the background of the dissertation such as the basic theory of superconductivity phenomenon, superconductor classification, and the discovery of superconductor according to T_c. Furthermore, the development trend of large–scale generators for offshore wind power and motivation of the dissertation are demonstrated.

Chapter 2 introduces the fundamental principle of the winding techniques for 2G HTS magnets. The pros and cons of the existence winding techniques, i.e., Kapton insulated, non–insulated, partial insulated, metal cladding, and metal insulated methods, for 2G HTS magnets in terms of fast magnetic field response and thermal stability are analyzed and discussed. Moreover, the equivalent circuit model, which is utilized to develop the analytical and numerical approaches, is also expressed to investigate the performance of the electromagnetic response and the thermal stability with considering joule heat generation inside the 2G HTS coil. The processing of formulated governing equations for both analytical and numerical methods in the steady and transient states are expressed based on the proposed equivalent circuit model.

Chapter 3 deals with the fabrications and experiments of the 2G HTS model coils. A small–scale NI pancake coil is fabricated and tested in the steady and transient states to estimate the magnetic field response and thermal stability, respectively. The simulation results of the NI

HTS coil are compared and discussed with the experiment ones to validate the simulation method based on the proposed equivalent circuit model. Then, two small–scale NI and MI–SS racetrack type coils are reported to compare the electrical characteristics of these test coils because the racetrack type coils are widely used to make the superconducting excitation field windings for wind turbine generators. In addition, to select the promising MI–SS winding technique for 2G HTS field coils of the 10 MW class HTS generator in terms of τ_d and thermal stability, three small–scale MI–SS racetrack coils, which are fabricated with various SS insulation thicknesses and winding tensions, are examined in the steady and transient states. In addition, the effects of the current ramp rate and current amplitude to the electrical behavior during the charging are performed to provide the useful references for estimating the electrical characteristics of 2G HTS field coils for the 10 MW class HTS generator. Furthermore, to investigate the effects of external magnetic field and cryogenic cooling conditions on the electrical and thermal characteristics, the MI-SS racetrack coil was tested under rotating magnetic field, which was generated by armature windings of 75 kW class induction motor, and conduction cooling system.

Chapter 4 presents the simulation results on the electrical and thermal characteristics for MI–SS 2G HTS field coils of the 10 MW class HTS generator used in offshore wind power. Based on the experimental results of three small–scale MI–SS racetrack coils, the contact surface resistance values are calculated and employed in the field winding to predict τ_d and thermal stability of the MI–SS 2G HTS field coils by using the proposed equivalent circuit model and the key parameters of 2G HTS field coils of the 10 MW class HTS generator.

Chapter 5 gives the conclusion of this dissertation.

Chapter 2. Winding Technology and Equivalent Circuit Model for 2G HTS Magnet

2.1. Winding technology for 2G HTS magnet

Second generation high temperature superconductors, i.e., $\mathrm{REBa_2Cu_3O_7}$–x (REBCO) coated conductors, have been considered as the most prospective candidate to develop high performance superconducting applications because they possess high current density, high stability margin, and low dependence of critical current (I_c) on an external magnetic field compared to their low temperature counterparts [1]–[5]. However, the 2G HTS has very slow NZPV because of the large specific heat capacity and multi–layer structures of its conductors as shown in the Fig. 2.1 [43]. For that reason, the self–protection characteristic inherent in LTS magnets becomes more difficult to achieve than in case of HTS magnets. Therefore, developing an additional quench protection scheme is essential to ensure the reliable operation for HTS magnet applications if any problems occur in the system [2].

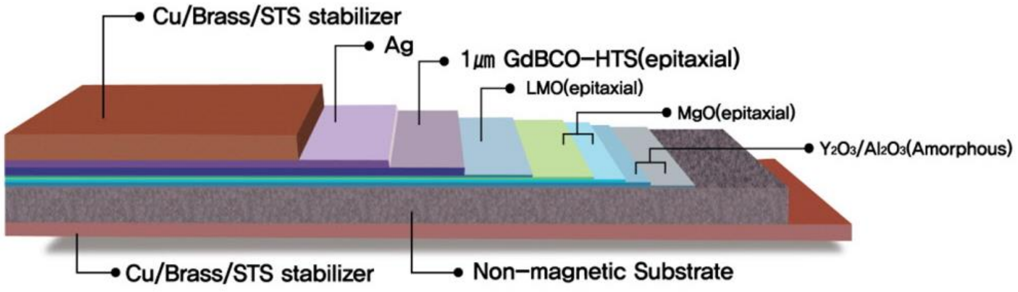

Fig. 2.1. Structure of 2G HTS coated conductor.

Recently, many research groups have been presented and studied the winding techniques for the development of compact 2G HTS magnets with improving the thermal stability characteristic due to their auto–protective feature of diverting excessive operating current into the transverse direction in the event of quench, such as no–insulation (NI), partial insulation (PI), metal cladding insulation (MC), and metal insulation (MI). The fundamental concept, operating mechanism, advantages and disadvantages of these winding technologies will be describe and discuss in this chapter.

2.1.1. No–insulation winding technique

The NI winding technique has been introduced to develop compact, mechanically robust, and self–protection HTS magnets for practical applications, such as NMR, MRI, and accelerators. The concept of this method has been reported, for the first time, on the experiment results of 2G HTS pancake coils by Hahn *et al* in 2010 [22]. The main idea behind this technique is complete elimination insulation between turn–to–turn layers in the 2G HTS coil to enhance the performance of the thermal stability in the transient state compared to its conventional INS winding technique. Fig. 2.2 shows the current flowing characteristic for INS and NI HTS coils in the event of quench. In general, when a local normal–state transition occurs in the INS HTS coil, the organic materials isolate every turns in the coil which causes high concentration current and overheating at the local hot spot, resulting in low thermal stability of the magnet as shown in Fig. 2.2(a). Whereas, in the NI HTS coil, the excessive current can be automatically diverted through the neighboring turns and thus the NI HTS coil can remain stable at a high overall current density as shown in Fig. 2.2(b). Therefore, the INS winding technique requires thick stabilizer to protect HTS magnets from permanent damage that make the HTS magnets becoming larger. Overall, the NI winding technique can provide a new and effective way to protect HTS coils without any external protection. However, the major drawback of NI winding technique is a delayed response time, i.e., a charging/discharging delay time of the target magnetic field under time–varying condition due to the absence of the insulation between turn–to–turn layers. For conventional INS HTS coil, the I_t flows only in the spiral direction to generate the expected design magnetic field. On the other hand, the bypass current flows through turn–to–turn contact path from its original spiral

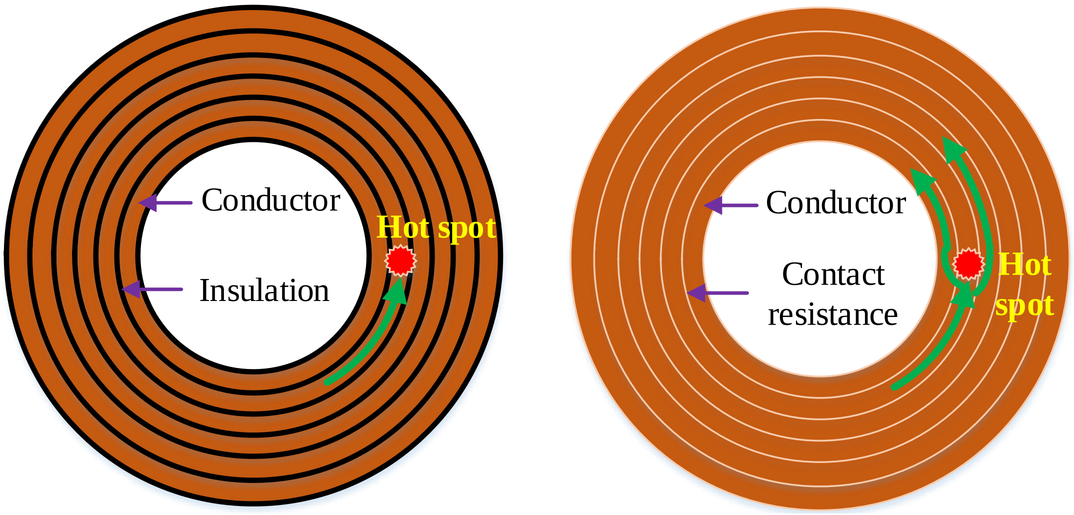

(a) INS coil

(b) NI Coil

Fig. 2.2. Current flowing characteristic during quench.

direction during the charging/discharging process, resulting in the slow charging/discharging delay time of the NI HTS coil.

The advantage and disadvantage of NI HTS coil have been reported in the experiment results from the previous published paper by Y. G. Kim *et al* [44]. As a results, the NI HTS coil showed longer discharging delay time than the INS HTS coil during the discharging test. However, in the over current tests, the NI HTS coil exhibited superior thermal stability compared to the INS HTS coil because the operating current can automatically diverted to the radial direction through turn–to–turn characteristic resistance to reduce heat generation when a local hot spot is generated in the HTS coil, as shown in Fig. 2.3. The NI winding technique shows the compact and high thermal stability during the overcurrent test. This technique is suitable for ultra–high–field, such as MRI and NMR. However, the weakness of NI winding technique is poor magnetic response time because of the delay issue during the charging/discharging process. Thus, the application of the NI winding technique is limited to the electrical devices which require fast controllability, such as superconducting rotating machines and SMES systems.

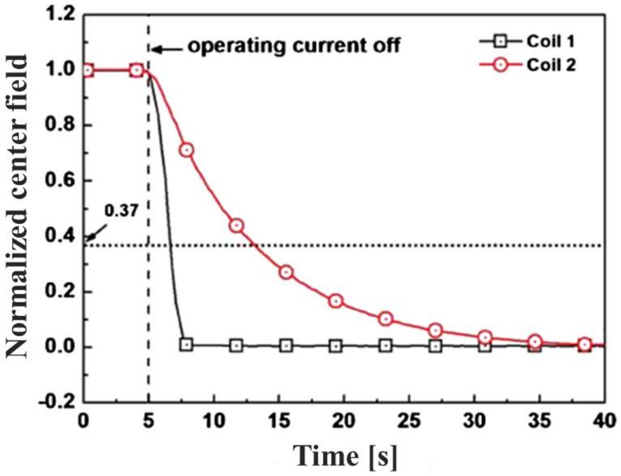

(a) Sudden discharging test

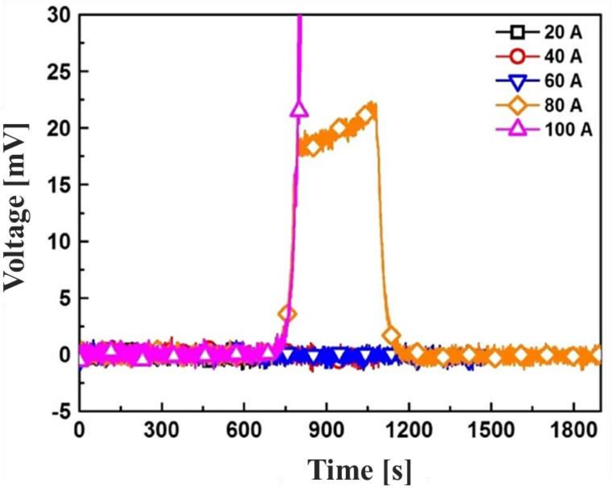

(b) Overcurrent test for INS coil

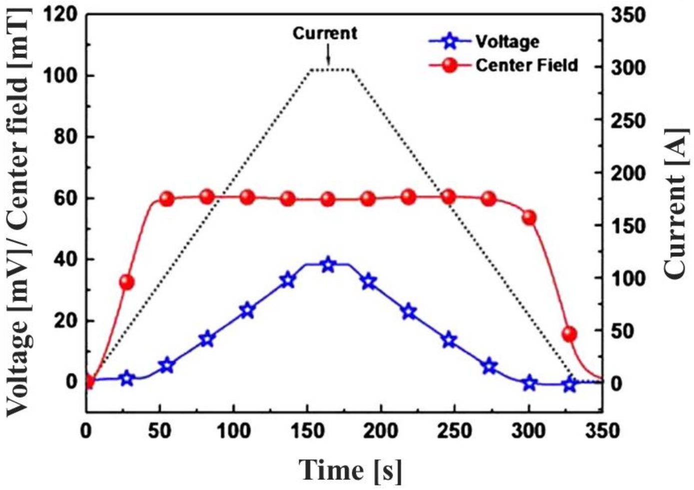

(c) Overcurrent test for NI coil

Fig. 2.3. Experiment results for INS (coil 1) and NI (coil 2).

2.1.2. Partial insulation winding technique

In order to overcome the drawback of NI coil in the slow charging/discharging delay time, the partial insulation (PI) winding technique has been proposed by several research groups [38], [39], [45], [46]. The basic concept of this method involved increasing the characteristic resistance by increasing the contact surface resistance due to the existence of turn–to–turn insulation materials at specific turns as shown in Fig. 2.4. As a result, the PI HTS coil can ameliorate the slow charging/discharging characteristic in the NI coil because the insulation materials are used in few selected turns of the HTS coil which can reduce a portion of bypass current to the adjacent turns. In addition, in the quench event, the excessive current can automatically bypass to radial direction through the turn–to–turn contacts within the non–insulated turns to protect the HTS coil from permanent damage.

Y. H. Choi *et al* experimentally conducted the charge and overcurrent tests for HTS coils with winding techniques of NI, INS, PI to compare the τ_d and thermal stability of these test coils. The results confirmed that the PI HTS coil can reduce the τ_d of NI HTS coil without sacrificing the self–protection characteristic, as shown in the Fig. 2.5 [38]. In the charge test, the PI HTS coils exhibited faster τ_d than the NI HTS coil due to the increase characteristic resistance between turn–to–turn layers. The overcurrent tests demonstrated that the PI HTS coil enhanced the thermal stability compared to the INS HTS coil.

The PI winding technique has been suggested to improve the slow charge/discharge rate in the NI winding technique. However, the mechanical strength of PI HTS coil is lower than that of the NI HTS counterpart due to the use of soft insulation material between specific turns. Based on the experiment results, the PI magnets may be the promising candidate for the self–protection HTS power applications that require both fast τ_d and high thermal stability.

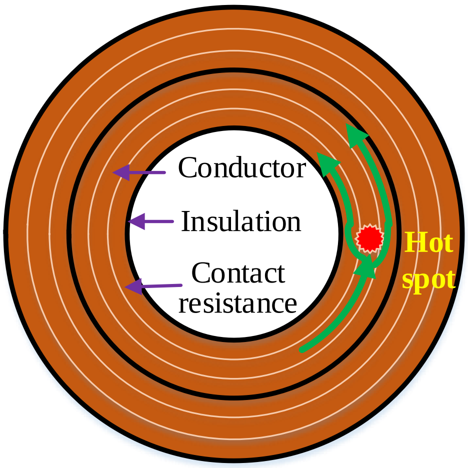

Fig. 2.4. Current flowing characteristic of PI HTS coil during quench.

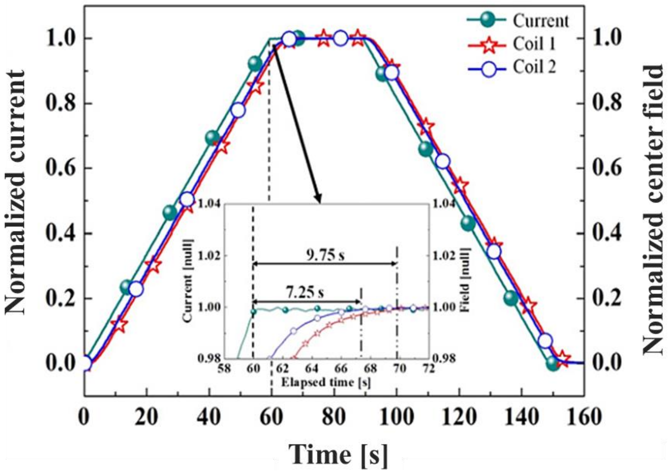

(a) Charging test

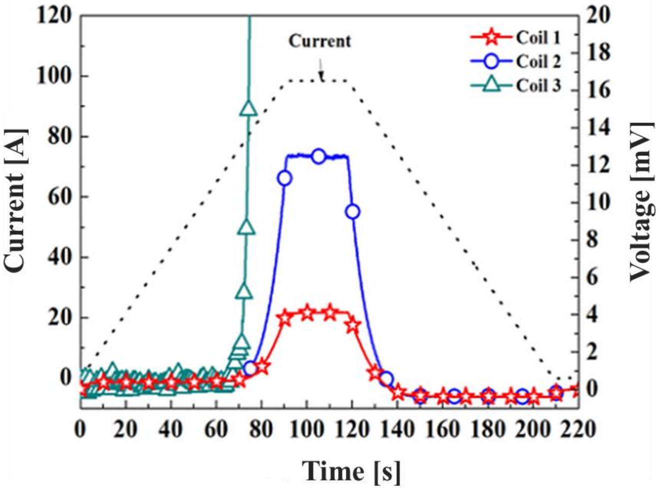

(b) Overcurrent test

Fig. 2.5. Experiment results of NI (coil 1), PI every five turns (coil 2), and INS (coil 3).

2.1.3. Metal cladding winding technique

Metal–cladding winding (MC) technique, which was suggested by the SuNAM Co., Ltd in 2016 [47], is also one of the potential solution to overcome the slow charge/discharge rate weakness of the NI coil. The MC HTS coil is fabricated by applying a micrometer thick metal cladding layer on the HTS tape to improve the turn–to–turn contact surface resistance, leading to the increase τ_d in the NI HTS coil. Fig. 2.6 shows the schematic drawing of the 2G HTS and MC 2G HTS tapes [48].

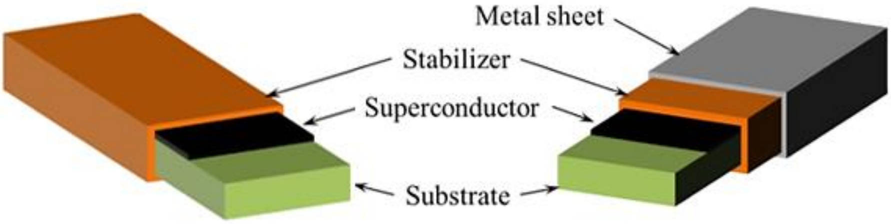

(a) **(b)**

Fig. 2.6. Schematic drawings of (a) 2G HTS and (b) MC 2G HTS tapes.

J. Kim *et al* performed the experiment tests on the MC and PI HTS coils to compare the effectiveness of these winding technique in terms of the τ_d and thermal stability. Fig. 2.7 shows the charge and overcurrent test results of MC, PI 3, PI 6, and PI 9 HTS coils [49]. The results showed that the MC HTS coil has magnetic field response faster than that of PI coils because of higher contact surface resistance between turns in MC HTS coil which can prevent a large portion of bypass current through the radial direction during the charge test. In the overcurrent test, the thermal stability of MC HTS coil was lower than those of PI HTS coils. However, the MC HTS coil was completely more stable than INS HTS coil. From these results, the MC winding technique is promising candidate for improving the slow charge/discharge rate behavior of NI HTS coil and may be suitable for the development self–protection of power applications which require fast charge/discharge rate.

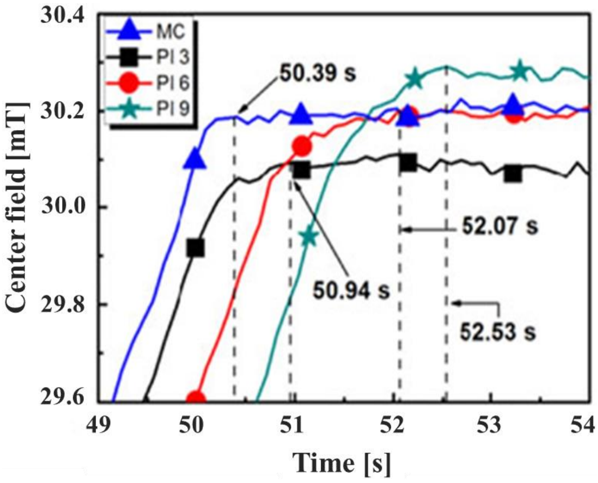

(a) Charging test

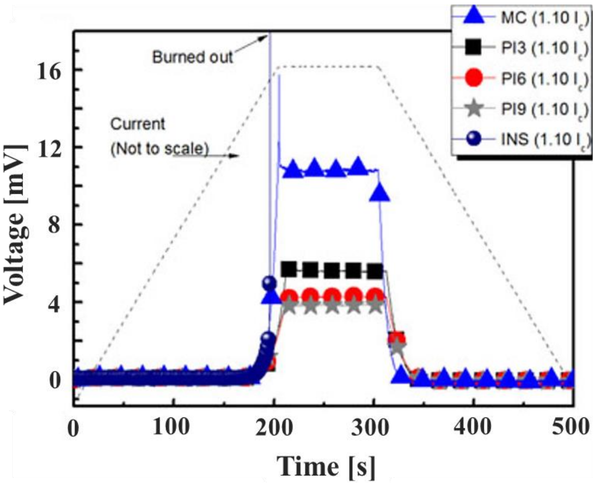

(b) Overcurrent test

Fig. 2.7. Experimental results of MC, PI 3, PI 6, and PI 9 HTS coils.

2.2. Metal insulation winding technique

The MI winding technique, which employs metal insulation material between the turn–to–turn layers, has been proposed as one of the potential solution to solve the slow charge/discharge rate weakness in the NI winding technique [50]–[52]. The main concept of this method is based on the increasing characteristic resistance by increasing the contact surface resistance owing to the presence of metal insulation between turn–to–turn layers. By increasing the characteristic resistance, the MI HTS coil can effectively enhance the τ_d in the NI HTS coil under time–varying condition. Fig. 2.8 shows the schematic drawing of the typical

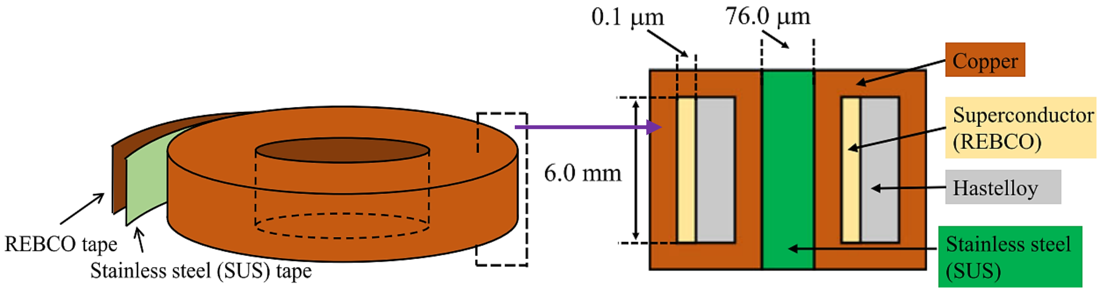

Fig. 2.8. Schematic drawings of the MI HTS pancake coil.

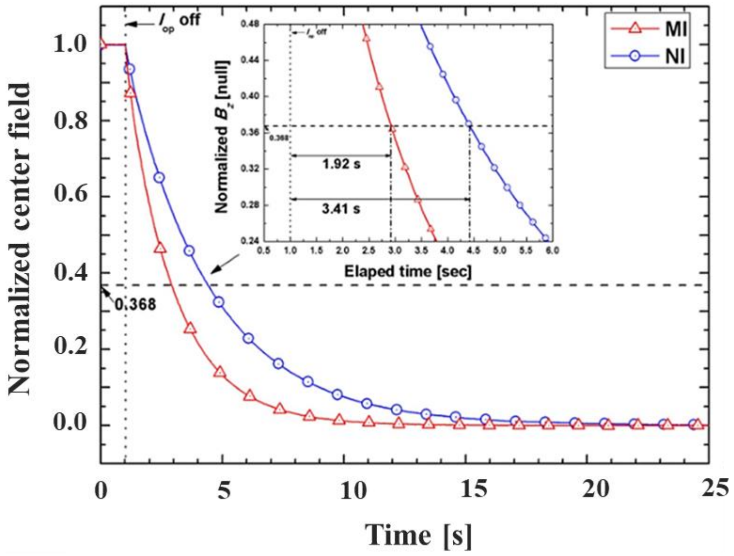

(a) Sudden discharge test

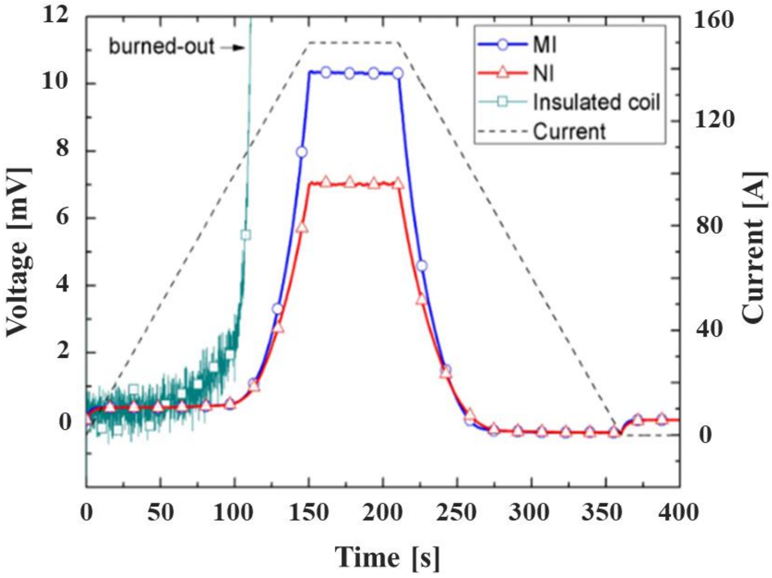

(b) Overcurrent test

Fig. 2.9. Experiment results of INS, MI, and NI HTS coils.

MI HTS pancake coil [53]. Although, the thermal stability of MI HTS coil was lower than those of NI, PI, and MC HTS coil, the MI winding technique showed good balance in terms of τ_d, thermal stability, and the ease of winding process, especially in large–scale HTS magnets. Thus, the MI winding technique is considered the best suitable for the large–scale HTS power applications which require both fast magnetic field response and high thermal stability.

D. G. Yang *et al* confirmed the benefits of MI HTS pancake coil in terms of the τ_d and the thermal stability compared with the NI, and INS HTS pancake coil [40]. Fig. 2.9 shows the sudden discharge and overcurrent test results of INS, MI, and NI HTS pancake coil. These results showed that the MI HTS coil can ameliorate the slow τ_d feature of NI HTS coil due to the increasing characteristic resistance between turn–to–turn layers. In addition, the MI HTS pancake coil demonstrated better thermal stability during the overcurrent test compared to the INS HTS pancake coil.

2.3. Equivalent circuit model for 2G HTS magnet

Fig. 2.10(a) shows an original equivalent circuit model for the HTS coils, in which each branch represents for the corresponding numbered turns in the HTS coils. If quench unexpectedly occurs in a weak layers of the HTS coils, the excessive current can easily bypass to the neighboring turns in the radial direction. However, in order to facilitate the calculation, the concise equivalent circuit model is utilized to analyze the magnetic field response and thermal stability for the HTS coils in the steady and transient states, respectively. The concise equivalent circuit model comprises a DC power supply, a switch, a shunt resistor, and a HTS coil in the cryogenic cooling environment, as shown in Fig. 2.10(b). Based on the Kirchhoff voltage and current laws, the governing equations of the model can be expressed as follows [24], [27], [28], [41], [42]:

$$L_c \frac{dI_\theta}{dt} + I_{st} R_{st} = I_r R_c \tag{1}$$

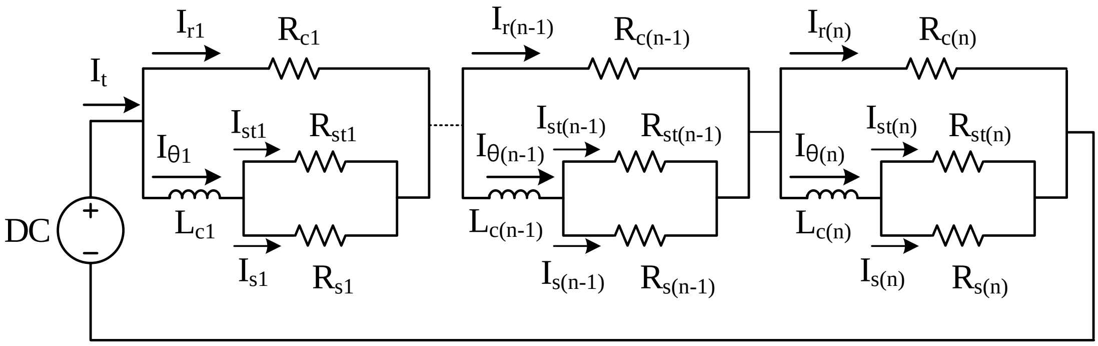

(a) Original model

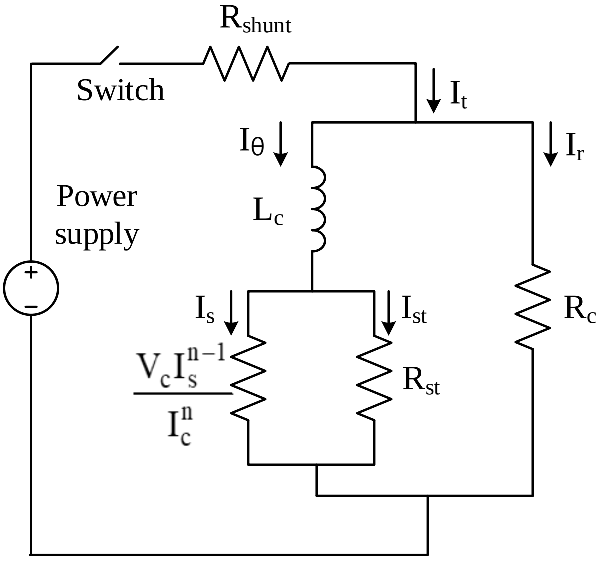

(b) Concise model

Fig. 2.10. Equivalent circuit model for HTS coils.

$$V_c\left(\frac{I_{sc}}{I_c}\right)^n = I_{st}R_{st} \tag{2}$$

$$I_\theta + I_r = I_t \tag{3}$$

$$I_s + I_{st} = I_\theta \tag{4}$$

where L_c, R_{st}, n, I_t, I_c and V_c are coil inductance, stabilizer resistance, n–value, current input, critical current, and critical voltage, respectively. I_θ and I_r represent the current flowing through the spiral and radial directions, respectively. I_s is the current flowing along the superconducting layer while I_{st} is the current flowing along the stabilizer layer. R_c is the characteristic resistance which includes the total sum of contact surface resistance (R_{cs}) and insulation resistances (R_{metal}) between turn–to–turn of the HTS coil, as shown in equation (5). However, the R_c is calculated mainly based on R_{cs}, which is mostly dependent on the surface roughness condition and the contact pressure, due to the small value of the resistivity of insulation material at 77 K, i.e., stainless steel (~5.3×10^{-7} Ωm) and copper (~2×10^{-9} Ωm). The R_c of the HTS coils can be estimated from the following equation [54], [55]:

$$\begin{aligned} R_c &= \sum_{i=1}^{Nt} R_i \\ &= \sum_{i=1}^{Nt} \frac{R_{ct}}{C_i \times \omega_d} + \rho \frac{t}{\omega_d \times l} \\ &= R_{cs} + R_{metal} \end{aligned} \tag{5}$$

where ρ, t, and l are the resistivity, thickness, and length of the insulation material, respectively. R_{ct} is the contact surface resistance and ω_d is width of the HTS tape. Furthermore, C_i is the circumference of the i–th turn of the HTS coils.

2.3.1. Steady state characteristic analysis

In the charging test, the equation of the equivalent circuit model can be formulated as follows:

$$L_c \frac{dI_s}{dt} = \left(I_t - I_s\right) R_c \tag{6}$$

The equation (6) can be solved by the both analytical and numerical methods. By using the analytical method, the precise solution is obtained in a closed form mathematical equations. However, the numerical method, which gives approximate solution, is utilized for the complicated problems that cannot solved by the analytical method. The numerical method is common in the practical problems because it can solve large systems or non–linear equations.

The governing equation (6) can be rearranged to the following form and solved by analytical approach:

$$\frac{dI_s}{dt} + \frac{I_s R_c}{L_c} = \frac{I_t R_c}{L_c} \tag{7}$$

The equation (7) is the first order linear differential equation. The analytical solution of the equation (7) can be obtained as follows [56], [57]:

$$I_s(t) = e^{-\int \frac{R_c}{L_c} dt} \left[\int \frac{I_t(t) R_c}{L_c} e^{\int \frac{R_c}{L_c} dt} dt + C \right] \tag{8}$$

Let $\tau = \frac{L_c}{R_c}$, we have

$$I_s(t) = e^{-t/\tau} \left[\int \frac{I_t(t)}{\tau} e^{t/\tau} dt + C \right] \tag{9}$$

where τ is time constant of the center magnetic field (B_z) which is the main factor for evaluating the discharging time of the HTS coils during the sudden discharging test with the normalized B_z. C is a constant which can be determined by an initial condition. The charging test process of the HTS coils can be classified into two sections, as shown in the Fig. 2.11.

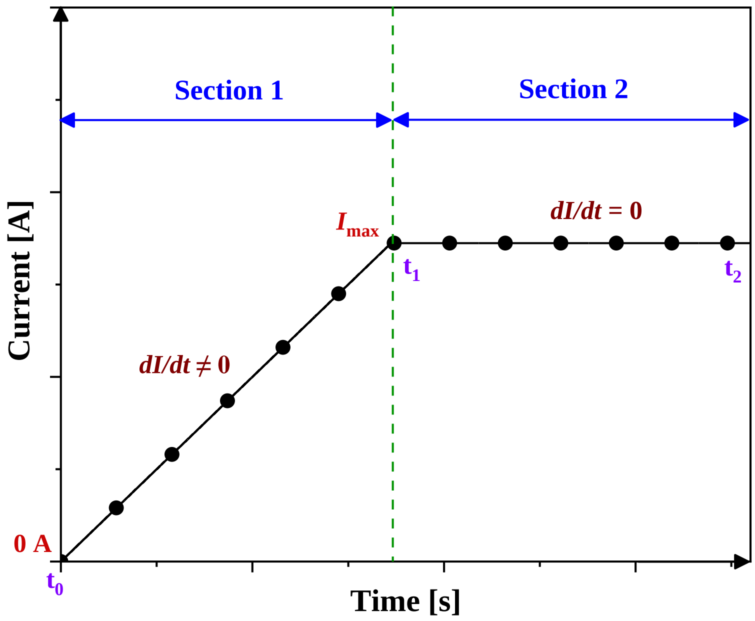

Fig. 2.11. Two sections of input current during the charging test process.

Section 1: I_t increases linearly (i.e., $dI_t(t)/dt \neq 0$) from the initial value ($I_i(t) = 0$) to the target value (I_{max}). To find the constant C, the equation (9) will be solved at the initial value.

Let $I_t(t) = ht; \quad \frac{dI(t)}{dt} = h$

where h, t, and $I_t(t)$ are the current ramping up rate, time period with respect to $I_t(t)$, and input current.

$$I_s(t) = e^{-t/\tau}\left[\frac{h}{\tau}\int te^{t/\tau}dt + C\right] \tag{10}$$

According to the integration by parts formula, we have

$$I_s(t) = h(t-\tau) + Ce^{-t/\tau} \tag{11}$$

At the initial value, we have

$t = 0; I_t(t) = 0; I_s(t) = 0; C = h\tau$

Substituting $C = h\tau$ into the equation (11), we have the analytical solution for the HTS coil at the section 1 during the charging test as follows:

$$I_s(t) = h\left[t - \tau\left(1 - e^{-t/\tau}\right)\right] \tag{12}$$

Section 2: I_t remains constant (i.e., $dI_t(t)/dt = 0$) at the target value (I_{max}) during the time period of t ($t_1 \rightarrow t_2$). Therefore, the equation (9) can be denoted as follows:

$$\begin{aligned} I_s(t) &= e^{-t/\tau}\left[\int \frac{I_t(t)}{\tau} e^{t/\tau} dt + C\right] \\ &= I_{\max} + e^{-t/\tau} C \end{aligned} \tag{13}$$

Similarly, we will solve the constant C at the initial value. The initial value of the section 2 is corresponding to the end value of the section 1 (i.e., $t_1 = I_{max}/h$). Therefore, we can substitute the solution of $I_s(t)$ in the equation (12) to the equation (13) and determine the constant C as follows:

$$C = h\tau\left(1 - e^{t_1/\tau}\right) \tag{14}$$

Substituting C into the equation (13), we have

$$I_s(t) = t_1 h + \left[\tau h\left(1 - e^{t_1/\tau}\right)e^{-t/\tau}\right] \tag{15}$$

As a result, the analytical solution of the equation (6) during the charging test can be expressed as follows [27], [28]:

$$I_{sc}(t) = \begin{cases} h\left[t - \tau\left(1 - e^{-t/\tau}\right)\right], & 0 \le t < t_1 \\ t_1 h + \left[\tau h\left(1 - e^{t_1/\tau}\right)e^{-t/\tau}\right], & t_1 \le t \le t_2 \end{cases} \tag{16}$$

where t, t_1, and t_2 are time period with respect to I_t, time location when the current ramping up becomes maximum (I_{max}/h), and remaining time of maximum I_t, respectively.

As mention above, the equation (6) can be solved by the numerical method. There are many numerical methods (i.e., Euler's method, Midpoint method, Taylor's method, Trapezoidal method, Runge–Kutta method, etc.) that can be used to solve the equation (6). In this study, we developed a simulation code using the fourth order Runge–Kutta method [58], [59] to solve the equation (6). The Runge–Kutta method is one of the commonly used method for solving differential equations. The higher order Runge–Kutta method can obtained higher accuracy but they suffer from the computation time. The fourth order Runge–Kutta method offers a good balance between the accuracy and cost of computation time compared to other numerical methods. With better precision, the fourth order Runge–Kutta method is expected to obtain the τ_d with the small error which is very important in high power application to predict τ_d of large–scale HTS coil. The formula of the fourth order Runge–Kutta method can be expressed as follow:

$$y(x+h) = y(x) + \frac{1}{6}\left(k_1 + 2k_2 + 2k_3 + k_4\right) \tag{17}$$

where

$$k_1 = hf\left(x, y\right)$$

$$k_2 = hf\left(x + \frac{1}{2}h, y + \frac{1}{2}k_1\right)$$

$$k_3 = hf\left(x + \frac{1}{2}h, y + \frac{1}{2}k_2\right)$$

$$k_4 = hf\left(x + h, y + k_3\right)$$

2.3.2. Transient state characteristic analysis

In the transient state, when a hotspot occurs in the HTS coils, one part of I_t is automatically bypassed to the adjacent turns. I_{sc} of the HTS coil can be estimated using the following equation, which is developed based on the equations (1)−(4) [27], [42], [55]:

$$L_c \frac{d\left(I_{sc} + I_{st}\right)}{dt} + V_c\left(\frac{I_{sc}}{I_c}\right)^n = R_c\left(I_t - I_{sc} - I_{st}\right) \tag{18}$$

To facilitate this calculation, we assumed that the current flowing through the stabilizer (I_{st}) was approximately zero, meaning that the excess quench current (I_q) mostly flowed in the radial direction through the turn–to–turn contact because R_c was approximately three orders of magnitude smaller than that of the stabilizer layer. Therefore, the following equation can represent the equation (18) to simplify the calculations:

$$L_c \frac{d\left(I_{sc}\right)}{dt} + V_c\left(\frac{I_{sc}}{I_c}\right)^n = R_c\left(I_t - I_{sc}\right) \tag{19}$$

Equation (19) can be solved using the numerical method. In this study, we developed a simulation approach based on the RK4 method to solve the equation (19). We considered the heat generation inside the HTS coil to estimate the electrical and thermal stabilities of the test coil. I_c decreased with the increase of heat generation in the HTS coils. The processing design of the simulation approach is demonstrated by the following steps:

Step 1: The material properties were declared which included the resistivity and specific heat of stabilizer and 2G HTS layers.

Step 2: The operating current is applied to the HTS coils until it reaches the target value.

Step 3: The material properties and critical current are determined.

Step 4: The current flowing in the spiral and radial directions can be calculated by using the following equations:

$$I_{st} = I_t \frac{R_c}{\left(R_{st} + R_c\right)} \tag{20}$$

$$I_r = I_t \frac{R_{st}}{\left(R_{st} + R_c\right)} \tag{21}$$

Step 5: The heat generation in the HTS coils can be estimated as follows:

$$Q_T = R_{st} I_{st}^2 + R_c I_r^2 \tag{22}$$

Step 6: Considering the criteria for ending the processing simulation. If the operation time reaches the end time, which was set up in the initial step, then the processing simulation will be end. Otherwise, the processing simulation will return to the step 3.

Chapter 3. Fabrication and Experiment of 2G HTS Magnet

3.1. Fabrication and experiment of NI pancake coil

As mention in Chapter 2, although the NI winding technique suffers from electromagnetic drawback in the steady state because of the response time delay of the center magnetic field which caused by the bypass current phenomenon under time–varying condition, it has thermally advantageous in the transient state owning to the self–protection characteristic. Therefore, the NI winding technique could be considered as an effective solution for improving the electrical and thermal stabilities of commercialization of 2G HTS coils in industrial applications such as NMR and MRI. To date, the benefits of the NI HTS magnets in the transient state have been mostly reported in the experimental conditions. There are just a few simulation studies which used partial element equivalent circuit model for numerical thermal stability behavior analysis [60]–[62] or used a lumped circuit model which consisted of the L_c and the parallel R_c [24], [47]. However, the characteristic of heat generation in the HTS coils by superconducting and stabilizer layers did not consider in these studies. Actually, the superconducting layer exhibited resistance when the operating current increased toward the I_c and rose rapidly at the value which was higher than I_c. Total heat in NI HTS coil included generated heat by characteristic resistance and superconducting layers. Therefore, more numerical simulation methods are needed to estimate the electrical characteristics of NI HTS coil under steady and transient states. In this section, we developed an advanced simulation code in MATLAB environment based on the proposed concise equivalent circuit model to evaluate electrical characteristics that considered the joule heat generation inside the HTS coil. Firstly, the current–voltage (I–V) and sudden discharging tests were conducted to measure the I_c and τ of the center magnetic field, respectively. Then, we performed a charging test to investigate the magnetic field response performance under a steady state operation with rated current charging as well as the thermal stability under a transient state operation with overcurrent charging. Finally, the simulation results of the NI HTS coil in both steady and transient states were compared and discussed with the experimental results to validate our simulation approach.

3.1.1. Experiment setup

Fig. 3.1 shows a picture of the winding machine for manufacturing various HTS coils in this dissertation which includes the control panel, HTS tape source, insulation source, and bobbin. The winding processing is controlled by control panel 1. However, the winding tension of insulation tape is adjusted separately by control panel 2 which is used for fabrication the MI coils.

Table 3.1 summarizes the specifications of the 2G HTS coated conductor tape, which was manufactured by SuNAM Co., Ltd with the model of SCN04200, and the parameters of the NI single pancake coil (SPC). The width and thickness of the 2G HTS wire were 4.1 and 0.15 mm, respectively. The minimum and maximum I_c values of the 2G HTS wire were 245 and 268 A, respectively, under LN2 bath of 77 K and self–field conditions.

Fig. 3.2 shows a photograph of the NI SPC. The 2G HTS tape was wound directly onto a fiber reinforced bakelite pancake bobbin with the number of winding turns of 30 and wire length of 7.96 m. The inner and outer diameters of the NI SPC were 80 and 89 mm, respectively. A transverse–type Hall sensor (HGCT–3020 from Lake Shore Cryotronics, Inc.) was installed at the center of a bakelite bobbin to measure the center magnetic field (B_z). In addition, two voltage taps using a thin copper paper were embedded at both ends of the SPC near the current leads to measure the terminal voltage (V_t) under steady and transient conditions. All signals of I_t, B_z and V_t were measured and recorded using the data acquisition (DAQ) system of the LabVIEW software.

Table 3.1. Parameters of 2G HTS tape and NI HTS coil.

Items	**Unit**	**Values**
2G HTS Coated Conductor Tape		
Manufacturer	–	SuNAM Co. Ltd
Conductor model	–	SCN04200
Conductor Width	[mm]	4.1
Conductor thickness	[mm]	0.15
Max I_c at 77 K, self–field	[A]	268
Min I_c at 77 K, self–field	[A]	245
Critical temperature	[K]	91
NI Single Pancake Coil		
Number of turns	–	30
Inner diameter	[mm]	80
Outer diameter	[mm]	89
HTS wire length	[cm]	796
Critical voltage	[μV]	796
I_c at 77 K, self–field *	[A]	125
Coil constant	[mT/A]	0.448
Characteristic resistance	[μΩ]	60
Contact resistance	[μΩ.cm^2]	21.8
Coil inductance	[μH]	150
Decay time constant	[s]	2.5

* Measured using 1μV/cm criterion

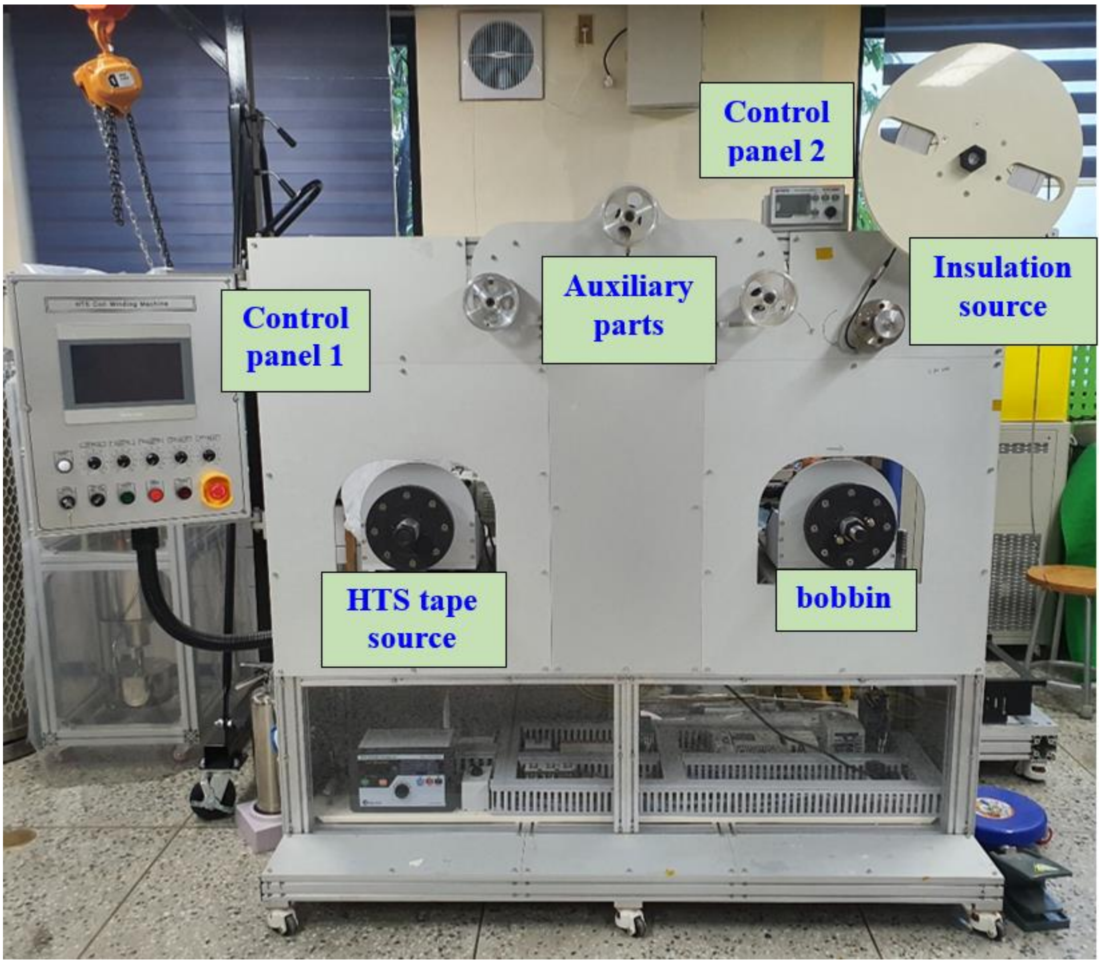

Fig. 3.1. HTS winding machine.

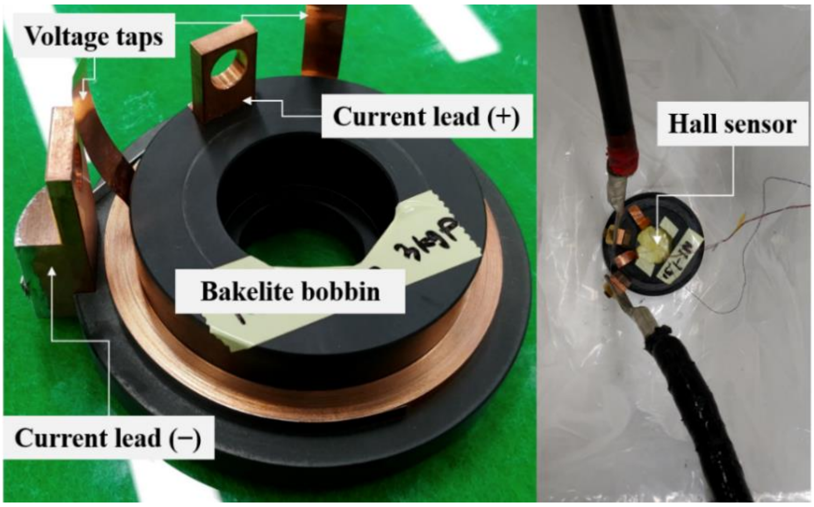

Fig. 3.2. Photographs of the NI SPC.

3.1.2. Results and discussion

A. Current–voltage test

The critical current of the NI SPC can be obtained by the *I–V* test with current ramp rate of 0.5 A/s in LN2 bath of 77 K, as shown in the Fig. 3.3. The input current applied to the test coil until the terminal voltage increased over the critical voltage of 0.796 mV which was calculated by multiplying the length of HTS wire and the criterion of 1 μV/cm (horizontal dashed line in Fig. 3.3). Then, the power supply was cut off to protect the test coil from permanent damage. The I_c value of NI SPC was measured as 125 A with respect to the critical voltage.

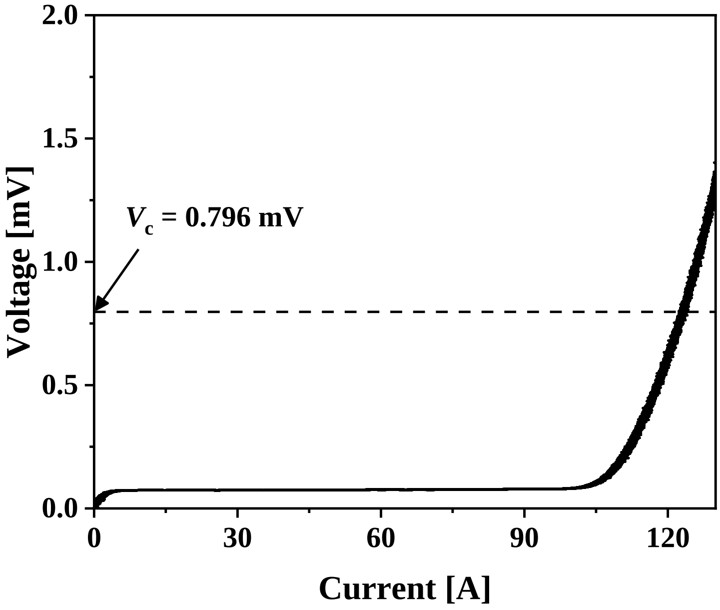

Fig. 3.3. Critical current test of NI HTS coil.

B. Sudden discharging test

In order to characterize the R_c of the NI SPC, the sudden discharging test was performed under steady state operation in a bath of LN2 environment. The R_c value can be simply estimated with respect to τ (i.e., $\tau = L_c/R_c$). L_c of the NI SPC was estimated to be 150 μH using the relationship between the inductor voltage (V_L) and current ramp rate (i.e., $V_L = L_c \times di/dt$).

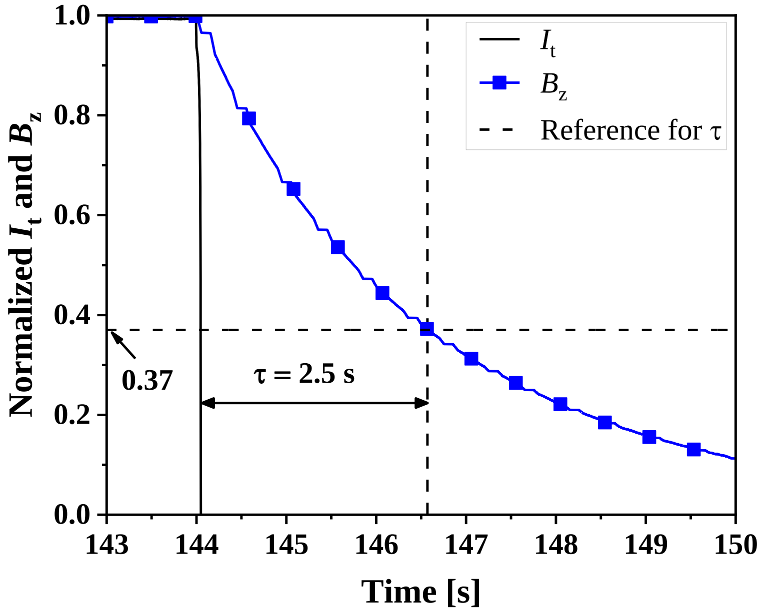

(a) Experiment

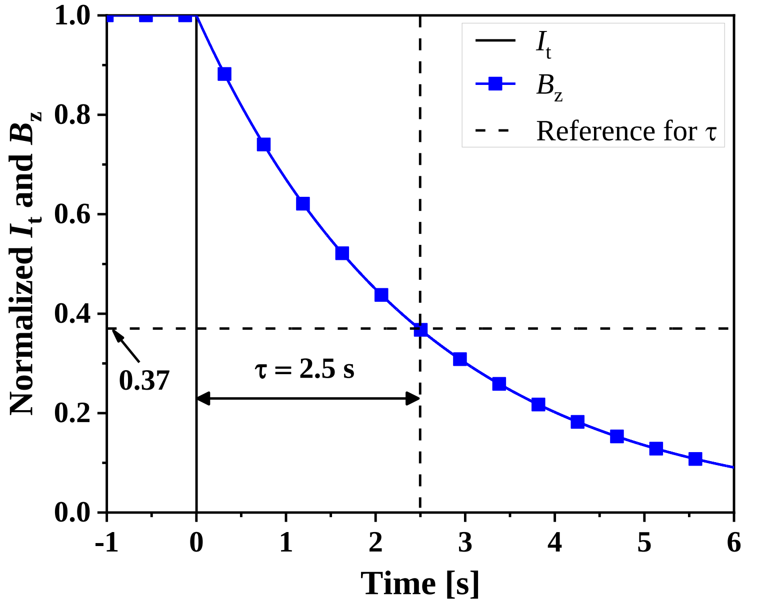

(b) Simulation

Fig. 3.4. Results of normalized B_z and I_t during sudden discharging test.

During the test, I_t gradually increased up to 100 A at a ramping rate of 1 A/s and remained at that for 60 s. Then, I_t was suddenly discharged to 0 A. The B_z of NI SPC according to time can be expressed as follows:

$$B_z(t) = B_{z0}e^{-t/\tau} \tag{23}$$

where $B_{z,0}$ is the initial value of B_z.

Fig. 3.4 shows the profiles of normalized I_t and B_z for NI SPC during the sudden discharging test. To facilitate the calculation of R_c, the magnetic field was normalized to its initial value. τ of the field decay was determined at the normalized value of 0.37 (i.e., $B_z/B_{z,0} = 1/e$ when $t = \tau$), as shown by the horizontal dashed line in Fig. 3.4, and was measured as 2.5 s. Based on the τ and L_c values, the calculated R_c was 60 μΩ. The simulation result was in good agreement with the experimental result, which proved that the validity of the analysis approached that of the proposed concise equivalent circuit model.

C. Charging test

The charging test was carried out under steady state condition to investigate the performance magnetic field response of the NI SPC. I_t of the tested SPC was charged up to 74 A (~ 0.6 I_c) with increment rate of 1 A/s. Thereafter, the applied current was maintained at that level for 60 s to implement the steady state operation. Subsequently, the power supply was decreased to 0 A with decrement rate of 1 A/s. Fig. 3.5 shows the experiment and simulation results of B_z and V_t for the NI SPC during the charging test. V_t of the NI SPC increased and finally reached 0.15 mV. The B_z increased linearly to 33.4 mT which agreed well with the coil constant. As expected, the τ_d of center magnetic field occurred due to the bypass current phenomenon. The τ_d for NI SPC were found to be 5.752 and 5.132 s in the experiment and simulation, respectively. The simulation result was 89.2 % slower than that of the experiment result. Overall, these results demonstrated that the simulation approach using the proposed equivalent circuit model is valid to characterize the τ_d of B_z in the NI SPC.

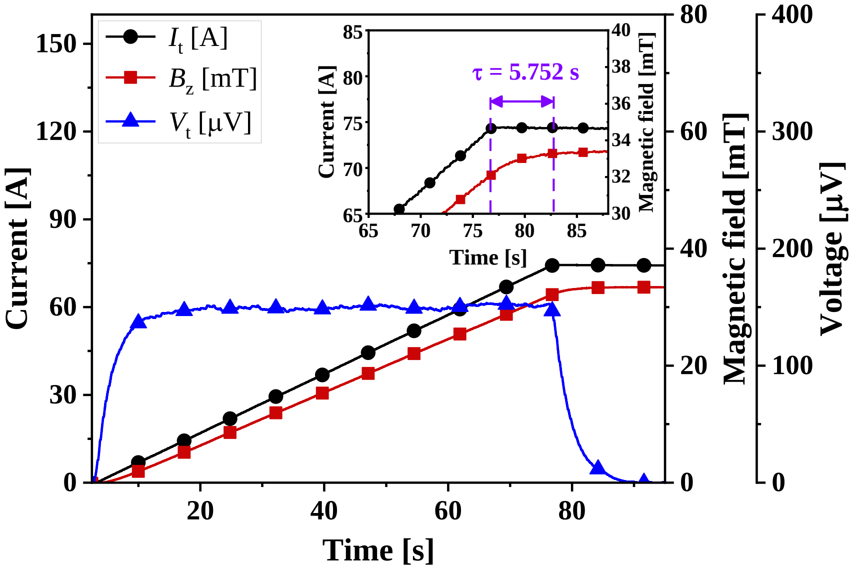

(a) Experiment

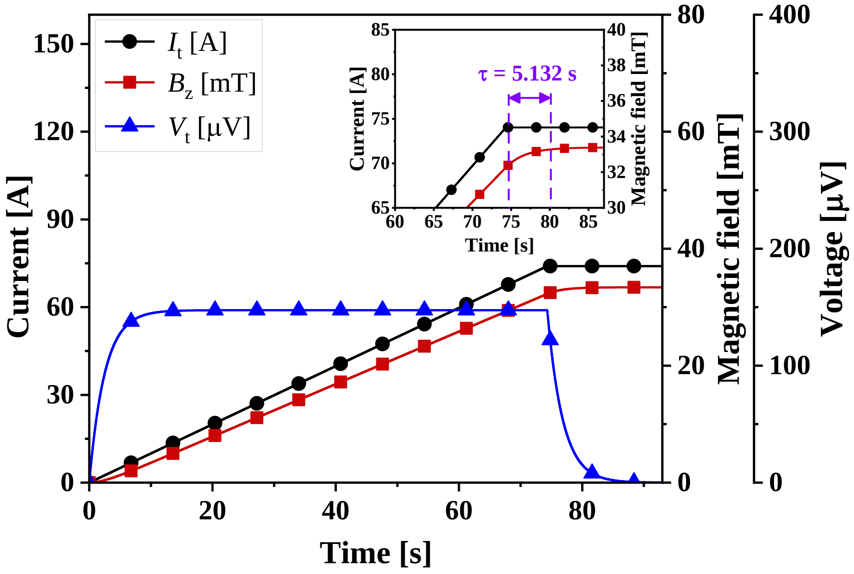

(b) Simulation

Fig. 3.5. Results of V_t and B_z behaviors in the steady state.

D. Overcurrent test

The overcurrent test was conducted in a LN2 bath at 77 K to investigate the thermal stability of the NI SPC in both actual experiment and numerical analysis. I_t increased to 137 A (1.1 I_c) at a charging rate of 1 A/s and remained at that level for 60 s. Then, I_t decreased to 0 A at a discharging rate of 1 A/s. Fig. 3.6 shows the experimental and simulation results of the V_t, B_z,

I_θ, I_r, and I_t profiles during overcurrent charging. V_t slowly started to increase below the I_c value, and it quickly reached the peak voltage of 2 mV. The values of V_t stably remained when I_t was maintained at 137 A, implying thermal balance between the LN2 cooling and joule heating caused by the overcurrent. During the test, the NI SPC exhibited self–protection feature against overcurrent to protect the NI SPC from permanent damage. The bypass current, i.e., I_r, was automatically generated due to a small value of R_c between turn–to–turn, as shown in Fig. 3.6(b). As a result, B_z lagged behind the target magnetic field value. As the I_t maintained at 137 A, the I_r value was estimated to be approximately 29.6 A. The overcurrent test result demonstrated that the thermal and electrical stabilities of the NI coil was higher than that of its conventional INS counterpart, which burned out at ~1.1 I_c [49], [63]. A small difference in V_t existed between the simulation (~1.8 mV) and experimental (~2 mV) results. This may be because the joule heat generation at both ends of current leads was not considered in the simulation analysis.

Fig. 3.7(a) shows the result of heat generation during the charging test for NI SPC. The total heat generation in the test coil (i.e., $Q_T = R_{sc}I_{sc}^2 + R_cI_r^2$) mostly came from the characteristic resistance because the resistance of 2G HTS tape exhibited a very small value under steady state condition. As a result, generated heat by 2G HTS tape (i.e., $Q_T = R_{sc}I_{sc}^2$) was equal to zero. The experiment heat generation by R_c (i.e., $Q_T = R_cI_r^2$) of NI SPC was around 0.38 mW which was almost identical to the simulation result. However, the resistance value of 2G HTS tape in the overcurrent test was considerably higher than that of the value in the charging test when the applied current increased toward to I_c, as shown in Fig. 3.7(b). Consequently, the total heat generation of NI SPC was calculated to be 0.24 W at the operating current of 137 A. The calculated heat generation in 2G HTS tape by simulation method was around 0.19 W at 137A which could not estimate by the experiment method due to the unknown value of resistance of 2G HTS tape. As the operating current maintained at 137 A, heat generation by R_c in experiment and simulation were approximate 0.071 W and 0.053 W,

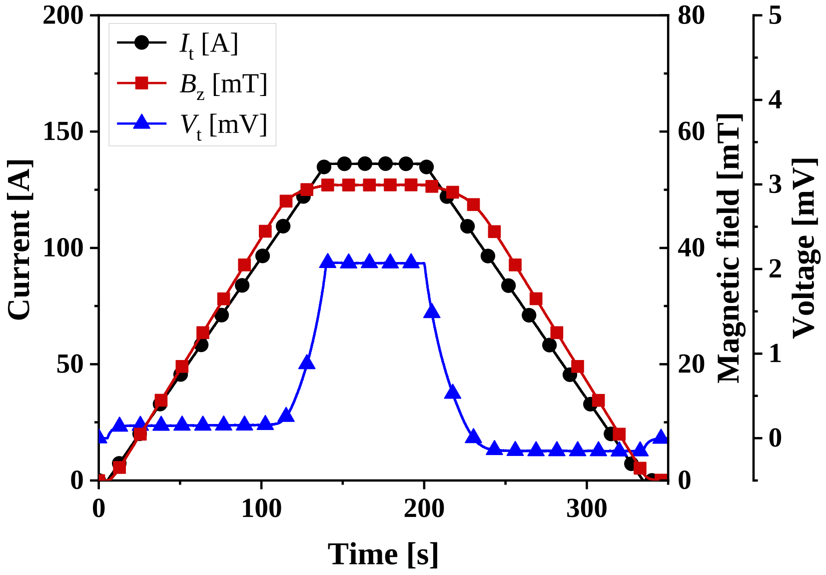

(a) Experiment

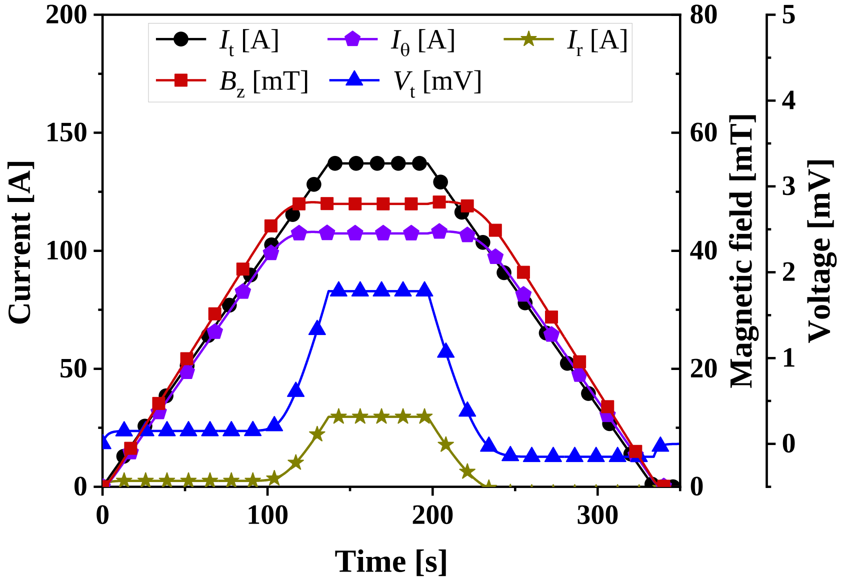

(b) Simulation

Fig. 3.6. Results of V_t, B_z, and current in the transient state.

respectively. The experiment result exhibited a higher value than that of the simulation result, which can be caused by heat generation of current leads during the experiment test.

In this section, we have developed an advanced simulation approach using the proposed concise equivalent circuit model to investigate the NI HTS coil under the steady and transient states. Both experiment and simulation approaches were successful to investigate the response

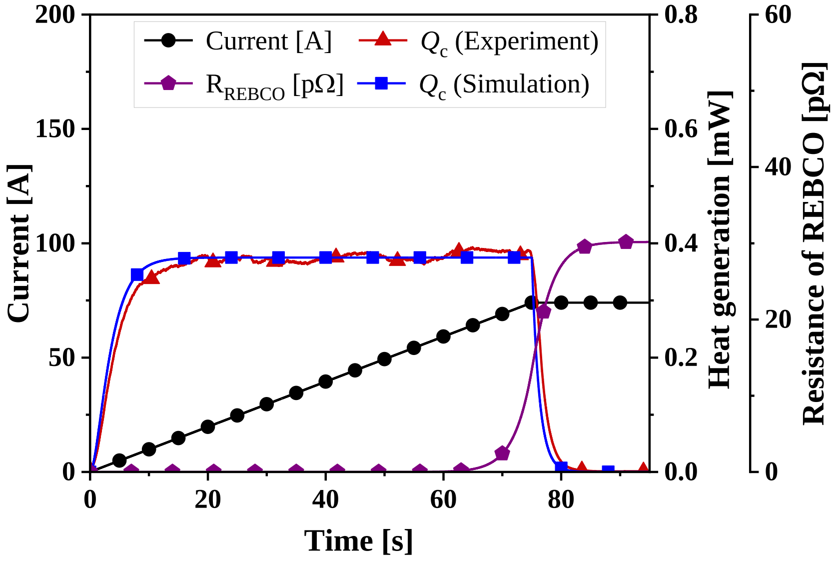

(a) Charging test

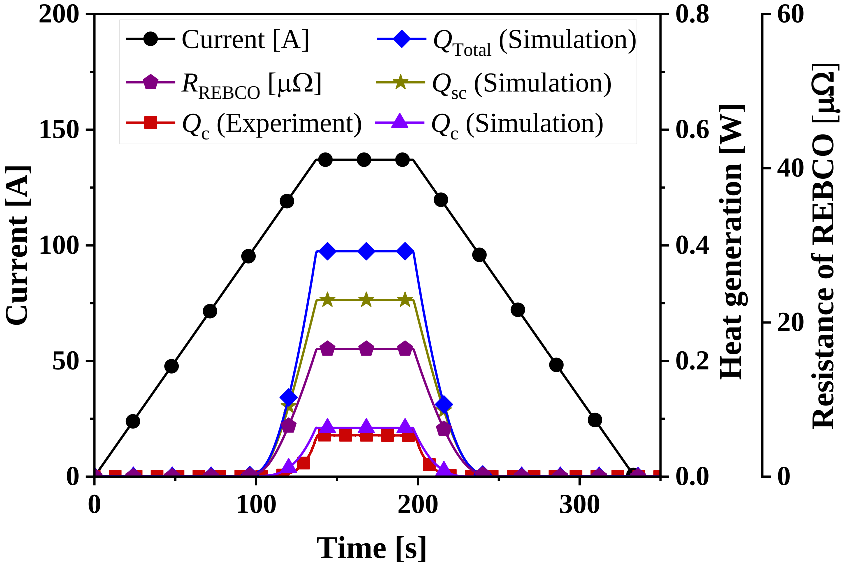

(b) Overcurrent test

Fig. 3.7. Experimental and simulation results of heat generation.

time delay of the magnetic field and thermal stability for the NI HTS in steady and transient states, respectively. We found that R_c of the NI HTS coil strongly influenced to the bypass current phenomenon in both the above mentioned characteristics. The charging test results of the NI HTS coil exhibited that the delay time in the simulation (5.132 s) was shorter than that of the experiment (5.752 s). On the other hand, the simulation approach demonstrated smaller heat generation than that of the experiment during the overcurrent test in the transient state. This may be because generated heat by current leads in the experiment test did not consider in the simulation. Furthermore, resistance of 2G HTS tape showed very small value in the charging test that did not affect heat generation in NI HTS coil. However, it exhibited high value in the overcurrent test which caused the increase of heat generation in NI HTS coil. During the overcurrent test, current was bypassed into the radial direction through turn–to–turn characteristic resistance to reduce heat generation. Overall, the simulation results were in good agreement with the experimental ones under all test conditions, which demonstrated that the simulation approach based on the proposed equivalent circuit model is valid.

3.2. Fabrication and experiment of NI and MI–SS racetrack coil

The NI winding technique has been suggested to develop 2G HTS coils due to its major benefits in terms of self–protection, mechanical robust, and compactness compared with the conventional insulated winding technique. If a quench occurs in the HTS coil, the applied current can be automatically diverted through neighboring turns to protect the magnet from permanent burn–out. However, the τ_d of magnetic field under time–varying condition can be a major challenge for the NI HTS coil because the leakage current can flow through the turn–to–turn contact layers. Therefore, the NI winding technique is difficult in applying to the application devices that require fast magnetic field response, such as superconducting rotating machine and SMES systems.

The MI winding technique has been introduced as a potential candidate to ameliorate τ_d in the NI winding technique owning to the increase in characteristic resistance. Several research groups have investigated the impact on τ_d and thermal stability characteristics of the MI coils. Studies have been conducted on the use of various material metal insulations [40], [50], [52], numerous silicon greases as insulation [41], [64], [65], and several metal insulation layers [66]. However, these studies mostly used pancake type coils. Therefore, it is necessary to investigate the τ_d and thermal stability characteristics of the MI winding technique which is wound in form

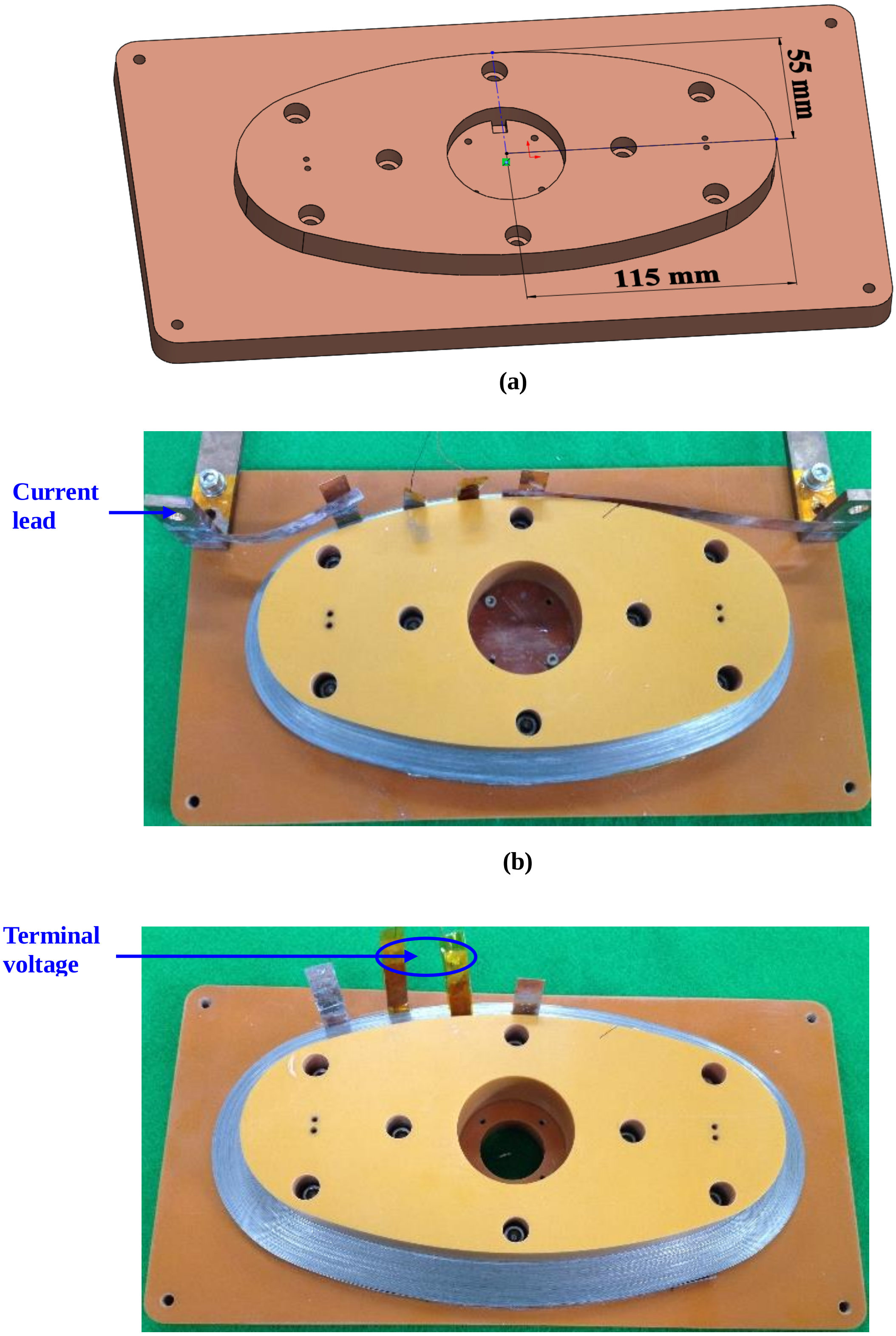

(a)

(b)

(c)

Fig. 3.8. (a) Design model of racetrack bobbin; photograph of (b) NI and (c) MI–SS coils.

Table 3.2. Parameters of 2G HTS tape and two racetrack coils.

Items	**Unit**	**Values**	
2G HTS Coated Conductor Tape			
Manufacturer	–	SuNAM Co. Ltd	
Conductor model	–	SLB04120	
Conductor Width	[mm]	4.1 ± 0.1	
Conductor thickness	[mm]	0.25	
Cu stabilizer thickness	[mm]	0.02	
Brass lamination thickness	[mm]	0.04	
Critical temperature	[K]	91	
NI and MI–SS Racetrack Coils			
Test coils	–	NI	MI–SS
Number of turns	–	50	50
Insulation thickness	[μm]	–	100
HTS wire length	[m]	30.18	30.92
Inner radius along x–axis	[mm]	115	115
Outer radius along x–axis	[mm]	127.5	132.5
Inner radius along y–axis	[mm]	55	55
Outer radius along y–axis	[mm]	67.5	72.5
Ic at 77 K, self–field*	[A]	144	104
Critical voltage	[mV]	3.02	3.09
Characteristic resistance	[mΩ]	0.027	3.19
Contact surface resistance	[$\mu\Omega.cm^2$]	13.4	1617.8
Coil inductance	[mH]	0.9	1.02
Winding tension	[kgf]	10	10

* Measured using 1 μV/cm criterion

of racetrack type coils.

This section presents the experiment and simulation results on the τ_d in the steady state and thermal stability in the transient state of both NI and MI–SS which were fabricated in form of racetrack type coils. First of all, the structural design of the racetrack type bobbin was shown along with its parameters. Then, the I–V tests were carried out to measure I_c values for both test coils. Also, the sudden discharging and charging tests were performed in the steady state to estimate the decay field time and magnetic field response, respectively. Finally, the overcurrent tests were conducted in the transient state to investigate the thermal stability of these test coils.

3.2.1. Experiment setup

Table 3.2 presents the specifications of the 2G HTS coated conductor tape, which was manufactured by SuNAM Co., Ltd., and two racetrack type coils, i.e., NI and MI co–wound with stainless steel tape. The width and thickness of 2G HTS wire were 4.1 mm and 0.25 mm, respectively. The maximum and minimum I_c values were respectively equal to 261 and 243 A under 77 K and self–field conditions. Fig. 3.8(a) shows the schematic drawing of the bobbin, which has a radius along the x–axis of 115 mm and y–axis of 55 mm, for fabrication the NI and MI–SS racetrack coils. Both coils had similar configuration in terms of number of turns, inner radius along x–axis, and inner radius along y–axis. The NI and MI–SS coils were wound at 10–kgf winding tension and directly onto the racetrack type bobbin, as shown in Fig. 3.8. The outer radius of MI–SS coil was larger than that of NI coil due to the thickness of stainless steel tape of 100 μm using between turn–to–turn layers. In addition, the total conductor length used in MI–SS coil (30.92 m) was longer than that of NI coil (30.18 m). The test results of operating current, V_t, and B_z were measured using DAQ system.

3.2.2. Results and discussion

A. Current–voltage test

Fig. 3.9 shows the I–V characteristic curves of two test coils which were conducted under a LN2 bath of 77 K to investigate the I_c values. Both test coils were charged at the current ramp rate of 0.5 A/s. The V_c values were calculated using 1 μV/cm criterion and the total length

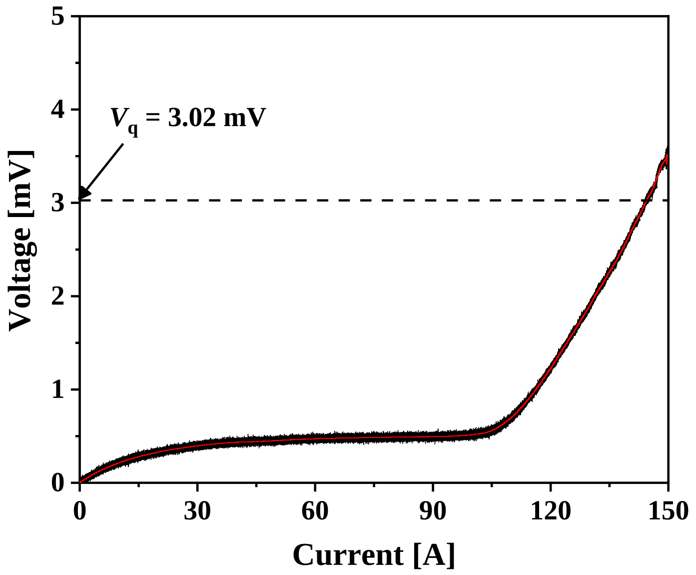

(a) NI coil

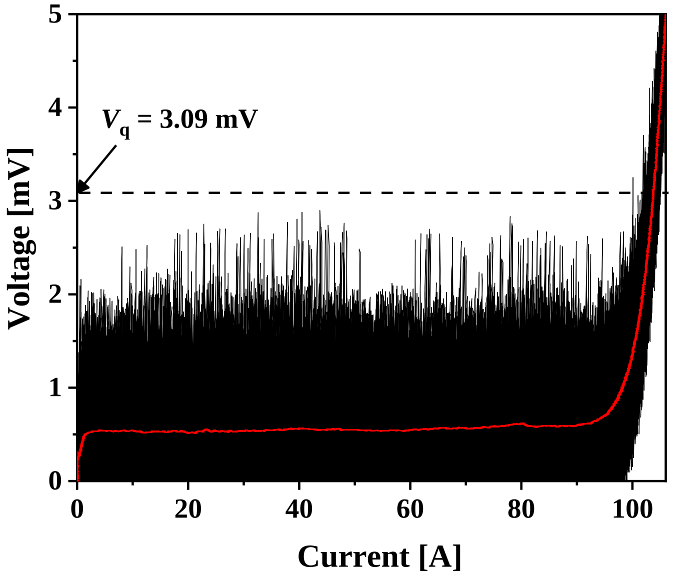

(b) MI–SS coil

Fig. 3.9. *I–V* characteristics at 77 K with current ramp rate of 0.5 A/s.

of HTS tape used for both test coils (blue dashed line in Fig. 3.9). Based on the V_c, the I_c values of NI and MI–SS coils were measured as 144 and 104 A, respectively. In order to obtain high accuracy the I_c value, the *I–V* curves were smoothed using the adjacent–averaging method. As shown in Fig. 3.9, the voltage curve of NI coil is more stable than that of the MI–SS coil. This may be because the MI–SS coil was influenced by the thermal disturbance.

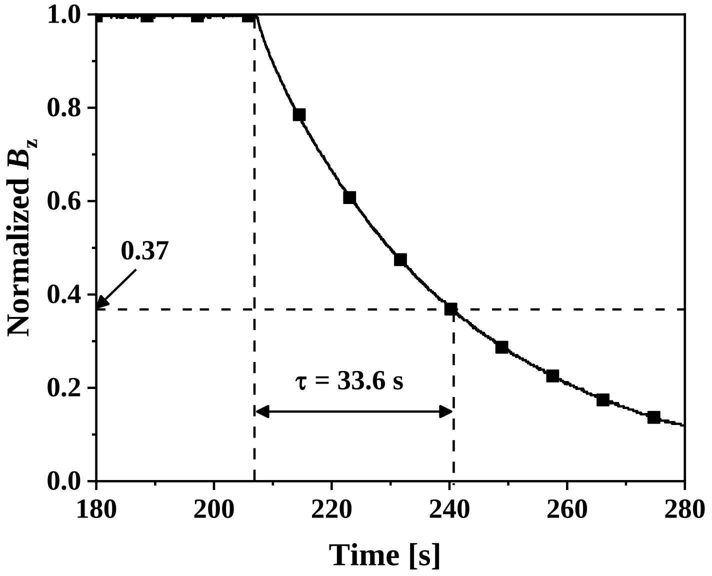

(a) NI coil

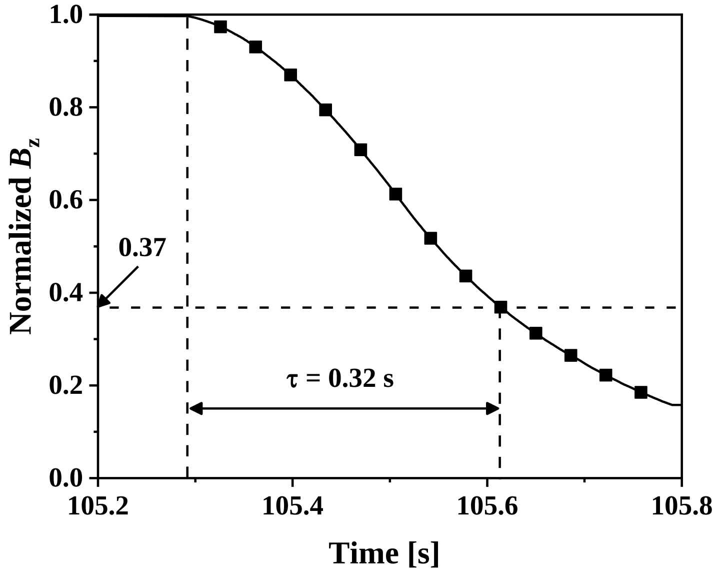

(b) MI–SS coil

Fig. 3.10. Sudden discharging test results at 0.7 I_c with charging rate of 1 A/s.

B. Sudden discharging test

The sudden discharging tests were conducted in LN2 bath of 77 K to estimate the τ and R_c values for NI and MI–SS coils. I_t was increased to 0.7 I_c (101 A for NI coil and 73 A for MI–SS coil) with current ramp rate of 1 A/s. Then, I_t was maintained at that level under steady state operation before the power supply current was turned off. Fig. 3.10 shows the experimental results during the sudden discharging test for NI and MI–SS coils. The τ of both test coils were measured at the normalized B_z value of 0.37 (i.e., $B_z/B_{z,0} = 1/e$ when $t = \tau$), as shown by the horizontal dashed line in Fig. 3.10. The τ values of the NI and MI–SS coils were 33.6 and 0.32 s, respectively. From the results of the τ values, the R_c values of NI and MI–SS coils (i.e., $R_c = L_c/\tau$) were 0.027 and 3.19 mΩ, respectively. The R_c of MI–SS coil was significantly higher than that of the NI coil. This is because the existence of the stainless steel tape between turn–to–turn layers increased the contact surface area in the MI–SS coil. These results exhibited that the MI–SS coil considerably improve slow τ_d characteristic of the NI coil.

C. Charging test

The charging tests were performed in LN2 bath of 77 K to estimate the τ_d for both NI and MI–SS coils. I_t was increased to 0.6 I_c (86 A for NI coil and 62 A for MI–SS coil) with the charging rate of 1 A/s. Figs. 3.11(a) and 3.12(a) show the experimental results versus time curves during the charging test for NI and MI–SS coils, respectively. As the I_t maintained at 0.6 I_c, the B_z values for NI and MI–SS coils increased linearly then reached 27 and 21 mT, respectively. The τ_d for NI and MI–SS coils were 117.04 and 0.975 s, respectively. As expected, the MI–SS coil showed faster τ_d than the NI coil due to increasing the R_c caused by the presence of stainless steel tape between turn–to–turn layers. The τ_d of the MI–SS coil was 99.17 % shorter than that of the NI coil. These results demonstrated that the MI–SS winding technique could significantly enhance the slow τ_d observed in the NI winding technique due to the increase of R_c by the existence of SS tape between turn–to–turn layers, resulting in a decrease leakage current. The “charging delay time” phenomenon could be explained by the proposed equivalent circuit model. During the ramping time (i.e., $dI/dt \neq 0$), I_t could be bifurcated in the spiral and radial directions, as shown in Fig. 2.10. As a results, the existence of I_r caused I_s lag behind I_t, resulting in the magnetic field loss in the test coils. Figs. 3.11(b) and 3.12(b) show the simulated results during the charging tests at 0.6 I_c for NI and MI–SS coils, respectively. The τ_d values for NI and MI–SS coils were 106.11 and 0.78 s, respectively, which were 9.3%

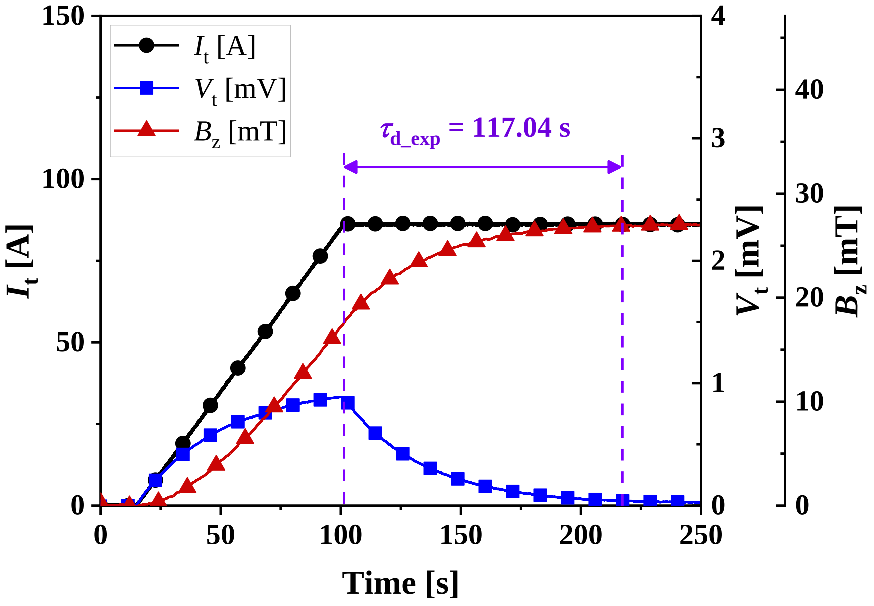

(a) Experiment

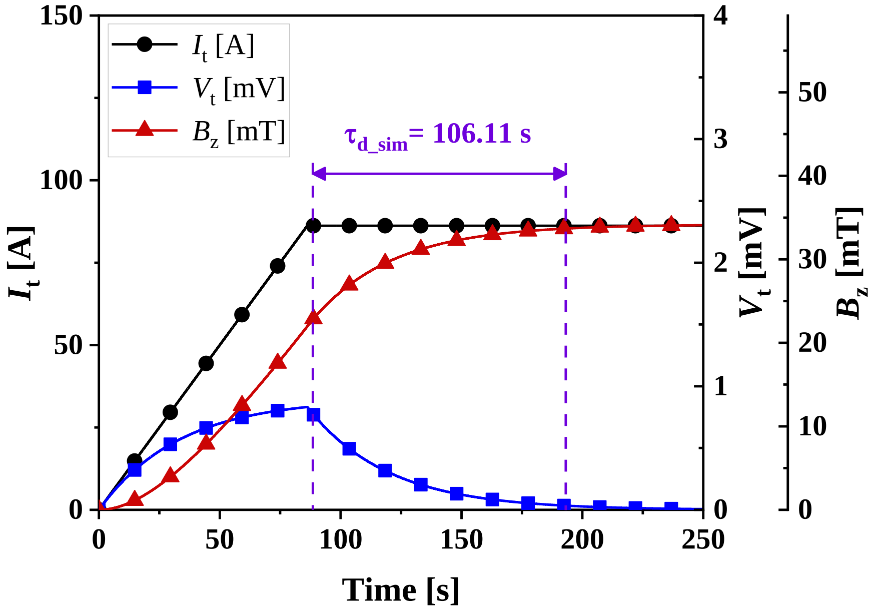

(b) Simulation

Fig. 3.11. Charging test results of NI coil at 0.6 I_c with charging rate of 1 A/s.

(NI coil) and 20% (MI–SS coil) smaller than the experimental results. This may be because heavy noises, which caused by thermal disturbance, occurred during the experiment tests. However, the maximum experimental results of V_t (~ 1 mV) for both test coils agreed well with the simulated results, which proved that the validity of the proposed equivalent circuit model.

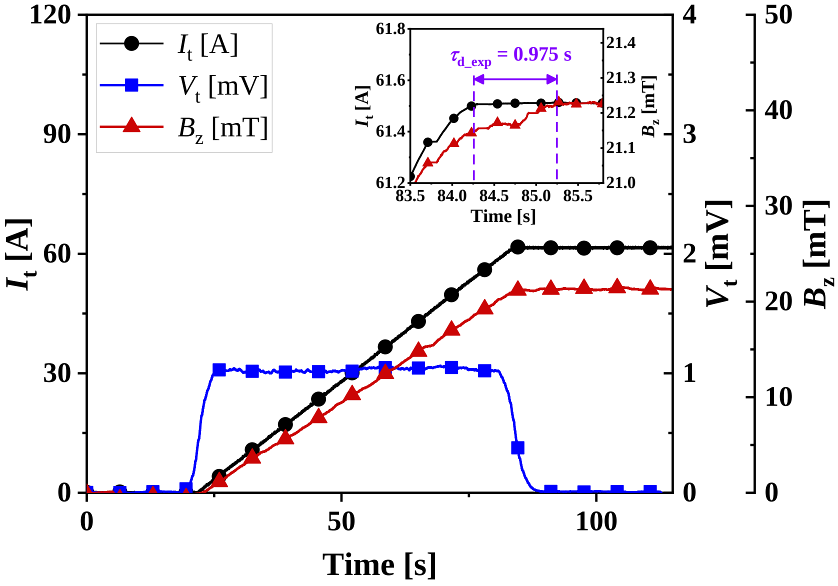

(a) Experiment

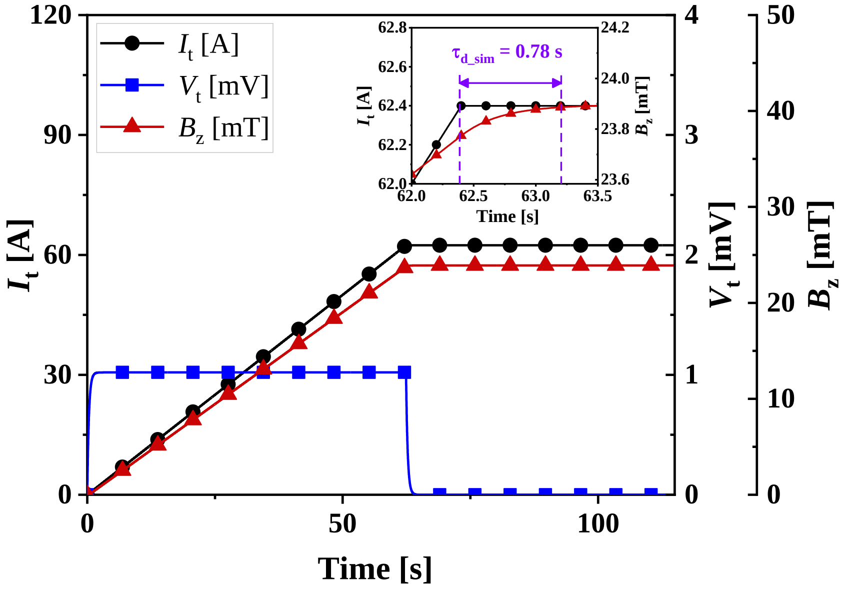

(b) Simulation

Fig. 3.12. Charging test results of MI–SS coil at 0.6 I_c with charging rate of 1 A/s.

D. Overcurrent test

The overcurrent tests were conducted in LN2 bath of 77 K to estimate the electrical and thermal stabilities of NI and MI–SS coils. I_t was increased to 1.1 I_c (158A for NI coil and 114 A for MI–SS coil) at the current ramp rate of 0.5 A/s. Figs. 3.13(a) and 3.14(a) show the experimental results for NI and MI–SS coils, respectively. Both test coils showed self–

protection feature during the overcurrent test operation. When I_t maintained at 1.1 I_c, the V_t of NI and MI–SS coils remained at steady state values of 3.6 and 21 mV, respectively, implying that the thermal was equilibrated between LN2 cooling and joule heating caused by the overcurrent. As the I_t decreased, the V_t started to decrease linearly and finally reaching zero, indicating that both test coils were fully recovered. The V_t value of MI–SS coil was 5.8 times higher than that of NI coil due to the existence of stainless steel tape between turn–to–turn layers, which reduced bypass current through the adjacent turns during the overcurrent tests. The results obviously showed that the NI coil had superior electrical and thermal stabilities compared with the MI–SS coil. However, the MI–SS coil exhibited stable operation to prevent the magnet from permanent damage under the overcurrent test at 1.1 I_c. These results verified that the MI–SS racetrack type coil could be a potential solution for the development 2G HTS field coils used in large–scale offshore wind turbine generators. Figs. 3.13(b) and 3.14(b) show the simulated results during the overcurrent tests for NI and MI–SS coils, respectively. The simulated V_t of NI and MI–SS coils were 2.2 mV and 18.5 mV, respectively, which were in good agreement with the experimental results. These results demonstrated that the proposed concise equivalent circuit model was validated for the NI and MI–SS racetrack type coils.

In section 3.2, the electrical characteristics of NI and MI–SS racetrack type coils have been investigated through the experiment and simulation to determine the preferable winding technique for the development 2G HTS field coils of the 10 MW class HTS generator used in offshore wind turbine environment. The simulation results were agreed well with the experimental results, which validated the proposed equivalent circuit model. The MI–SS racetrack coil showed a good balance between the τ_d and thermal stability compared with NI racetrack coil. The τ_d for MI–SS racetrack coil is approximately 99 % faster than that of NI racetrack coil. During the overcurrent test at 1.1 I_c, although the MI–SS racetrack coil showed higher V_t and Q_T values than that of the NI racetrack coil, the MI–SS racetrack coil operated successfully during the transient state against excessive current to protect the test coil from permanent burn–out.

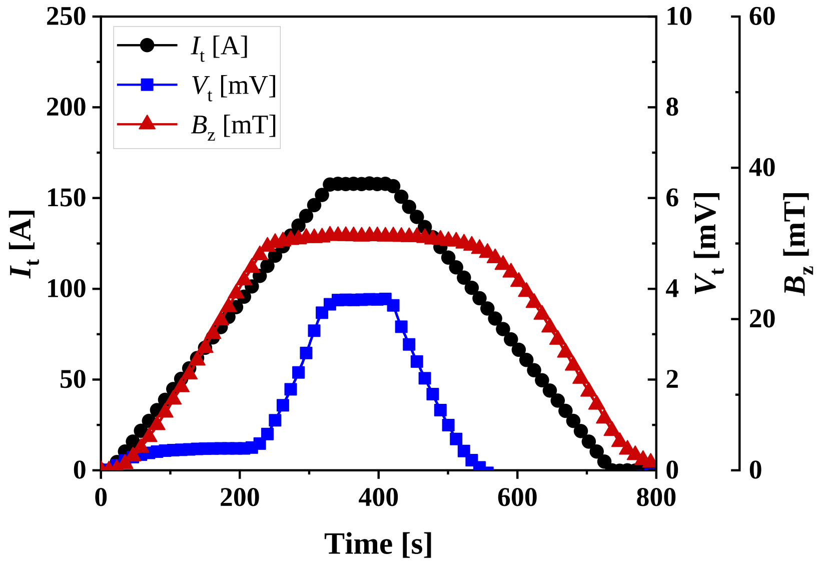

(a) Experiment

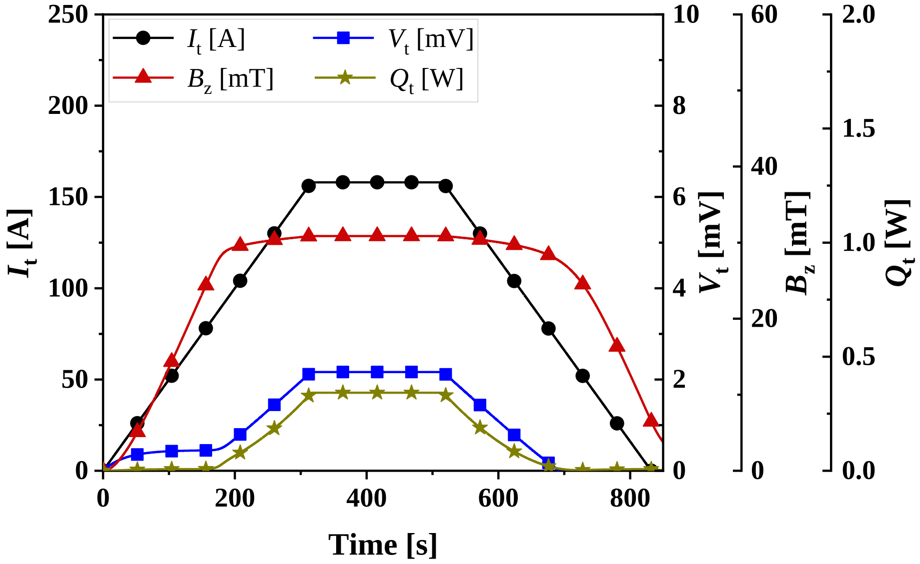

(b) Simulation

Fig. 3.13. Overcurrent test results of NI coil at 1.1 I_c with charging rate of 0.5 A/s.

Overall, the MI–SS winding technique, which possesses both fast τ_d and high thermal stability, proposes as the effective candidate to develop 2G HTS field coils of the 10 MW class HTS generator. These results would be useful references for the design of future 2G HTS field coils used in offshore wind turbine. For more details of investigating on the τ_d and thermal stability behaviors of the MI–SS racetrack type coil, it is necessary to estimate the effects of stainless

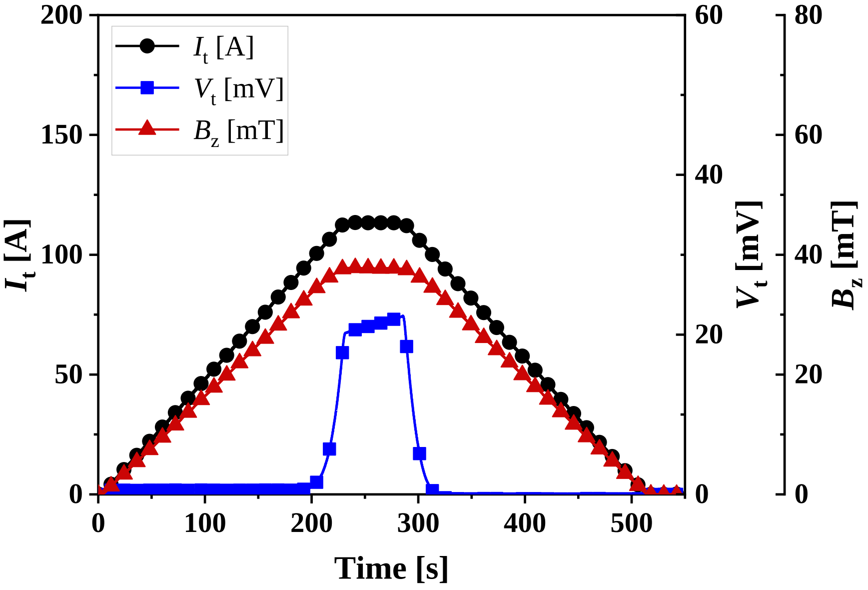

(a) Experiment

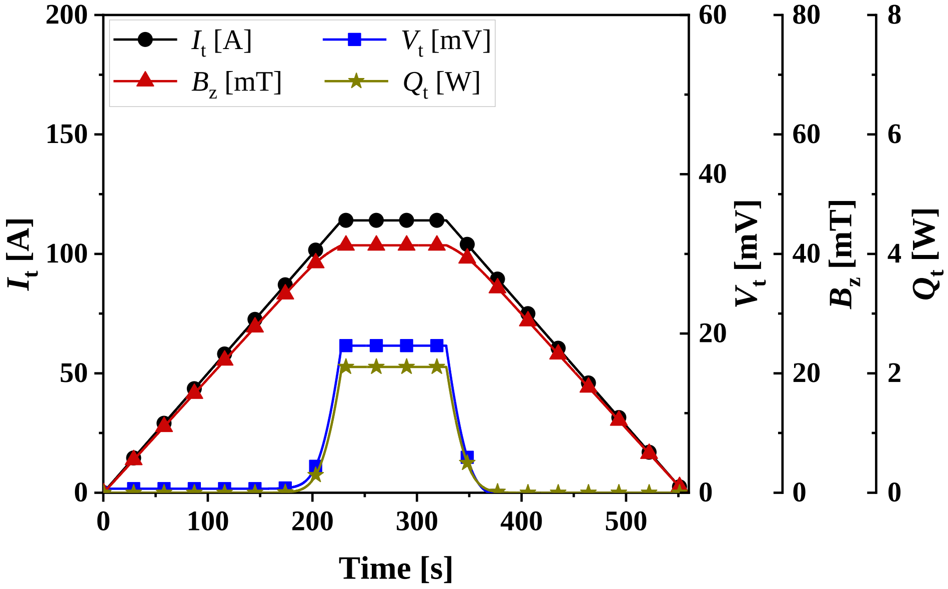

(b) Simulation

Fig. 3.14. Overcurrent test results of MI–SS coil at 1.1 I_c with charging rate of 0.5 A/s.

steel thickness and winding tension on the electrical characteristics to optimize the economic efficiency as well as the operation reliability of the MI–SS winding technique for 2G HTS field coils.

3.3. Fabrication and experiment of MI–SS racetrack coils according to various winding tension and stainless steel insulation thickness

The MI winding technique has been suggested as the effective approach to overcome the slow charge–discharge rate of NI winding technique, as shown in section 3.2. However, to utilize the MI winding technique for the development 2G HTS field coils of the 10 MW class HTS generator, it is essential to investigate the factors that affect to the τ_d and thermal stability of MI coils. This section estimates the electrical characteristics of 2G HTS racetrack coils co–wound with stainless steel tapes of various thicknesses and winding tensions. The SS thickness and winding tension are identified as the factors affecting the τ_d and thermal stability of MI coils. To verify these characteristics, three types of MI–SS racetrack coils were fabricated with various SS thicknesses and winding tensions: 100–μm SS thickness and 10–kgf winding tension (coil 1); 100–μm SS thickness and 5–kgf winding tension (coil 2); and 50–μm SS thickness and 10–kgf winding tension (coil 3). Three MI–SS racetrack coils were characterized in the LN2 bath of 77 K through the *I*–*V* test, sudden discharging, charging, and overcurrent tests. The *I*–*V* test was conducted in the steady state to evaluate the I_c values for the test coils. The sudden discharging and charging tests were performed in a steady state to investigate the time constant and τ_d of the center magnetic field, respectively. To investigate the thermal stability of three MI–SS racetrack coils, the overcurrent tests were conducted in a transient state at 1.1 and 1.05 I_c. Based on these results, the τ_d and thermal stability of three MI–SS racetrack coils were compared and analyzed in detail to determine a preferable winding approach for improving τ_d as well as the thermal stability of 2G HTS field coils for the 10 MW class HTS generator used in offshore wind power environment.

3.3.1. Experiment setup

Table 3.3 summarizes the parameters of the 2G HTS coated conductor, which was manufactured by SuNAM Co., Ltd., and three types of MI–SS racetrack coils. The width and

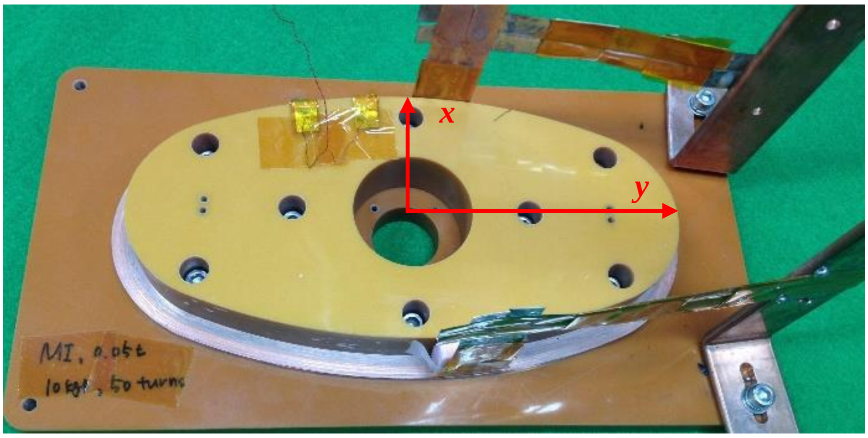

(a) Coil 1

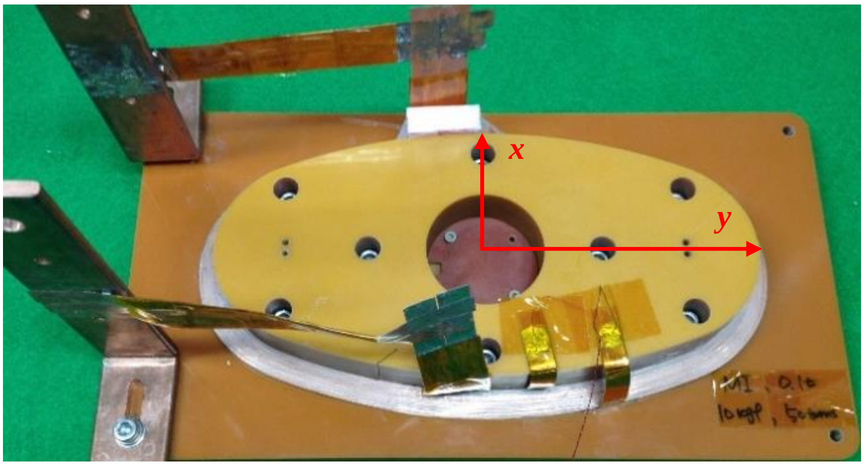

(b) Coil 2

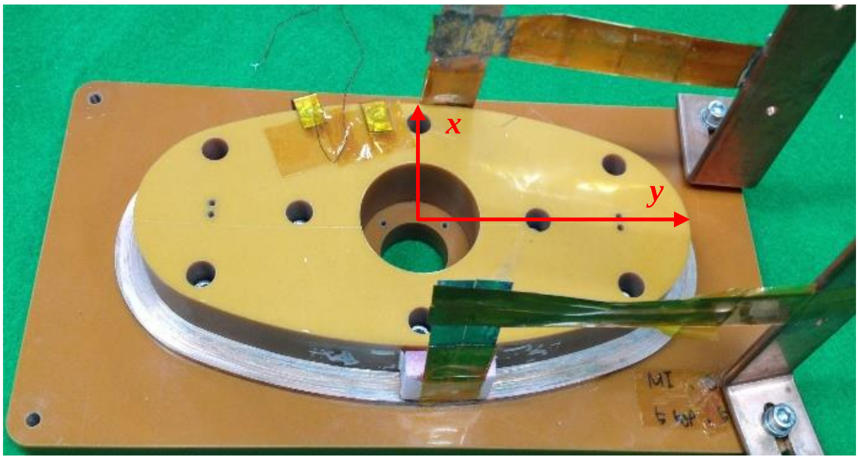

(c) Coil 3

Fig. 3.15. Photograph of MI–SS racetrack coils.

Table 3.3. Parameters of 2G HTS tape and three racetrack type coils.

Items	**Unit**	**Values**		
2G HTS Coated Conductor Tape				
Manufacturer	–	SuNAM Co. Ltd		
Conductor model	–	SCN04150		
Conductor Width	[mm]	4.1 ± 0.1		
Conductor thickness	[mm]	0.15		
Min I_c at 77 K, self–field*	[A]	236		
Max I_c at 77 K, self–field*	[A]	248		
Critical temperature	[K]	91		
Three Racetrack Coils				
Test coils	–	Coil 1	Coil 2	Coil 3
Number of turns	–	50	50	50
Material insulation	–	SS	SS	SS
Insulation thickness	[μm]	100	100	50
Winding tension	[kgf]	10	5	10
HTS wire length	[m]	30.1	30.1	29.73
Inner radius along x–axis	[mm]	115	115	115
Outer radius along x–axis	[mm]	127	127	124.5
Inner radius along y–axis	[mm]	55	55	55
Outer radius along y–axis	[mm]	67	67	64.5
I_c at 77 K, self–field*	[A]	100	104	100
Critical voltage	[mV]	3.01	3.01	2.97
Characteristic resistance	[mΩ]	3.195	8.621	7.813
Contact surface resistance	[μΩ.cm^2]	1577	4256	3809
Coil inductance	[mH]	1	1	1

* Measured using 1–μV/cm criterion

thickness of the 2G HTS coated conductor tape were 4.1 and 0.14 mm, respectively. Fig. 3.15 shows the structural dimensions of the fiber reinforced bakelite racetrack type bobbin with a radius along the *x*–axis of 115 mm and *y*–axis of 55 mm. Three coils were wound directly onto the bobbin with various SS thicknesses and winding tensions. Coils 1, 2, and 3 were wound with the winding tension maintained at 10, 5, and 10 kgf, respectively. The three coils exhibited identical configurations and number of turns, indicating similar coil inductance of 1 mH. However, the thicknesses of the SS tape (100 μm) used in coils 1 and 2 were larger than that of coil 3 (50 μm), which made the outer radius of coils 1 and 2 larger than that of coil 3. Thus, the total conductor length used in coils 1 and 2 (30.1 m) was longer than that used in coil 3 (29.73 m). During the tests, the current, voltage, and magnetic field were measured and recorded using the DAQ system of LabVIEW software.

3.3.2. Results and discussion

A. Current–voltage test

Fig. 3.16 shows the I_c curves with respect to V_c of three MI–SS racetrack type coils, which were performed in a bath of LN2 at 77 K. The current ramp rate of I_t was set to 1 A/s and applied to three test coils until the V_t increased over the V_c. Then, I_t was turned off to prevent three test coils from permanent damage. The V_c values of coil 1 (3.01 mV), coil 2 (3.01 mV), and coil 3 (2.97 mV) were calculated using the electric field criterion (E_c) of 1–μV/cm and the total length of the 2G HTS conductor tape used for manufacturing the test coils (horizontal dashed line in Fig. 3.16). According to V_c, the I_c values of coils 1, 2, and 3 were measured as 100, 104, and 100 A, respectively, as shown in Fig. 3.16.

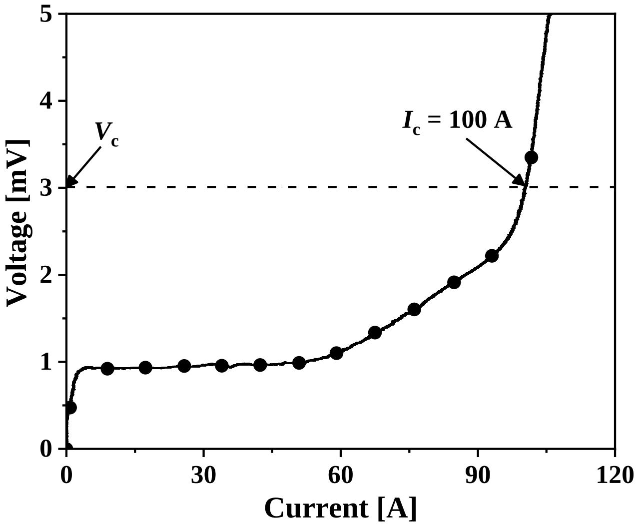

(a) Coil 1

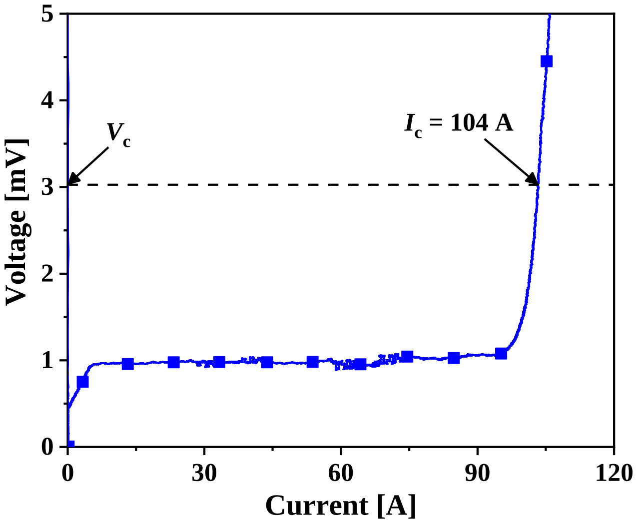

(b) Coil 2

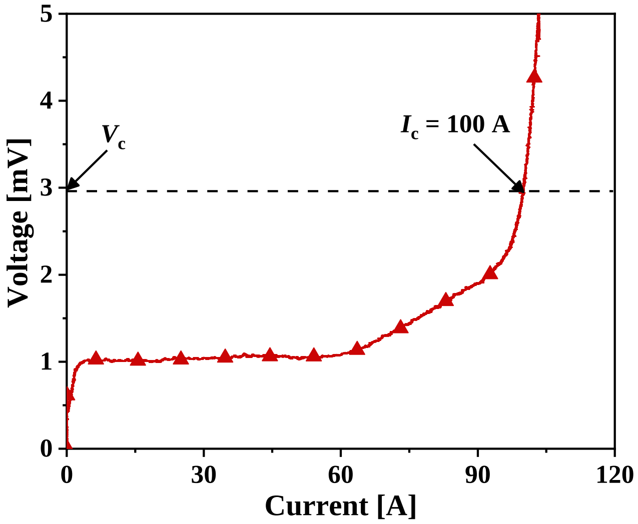

(c) Coil 3

Fig. 3.16. Critical current values at 77 K with current ramp rate of 1 A/s.

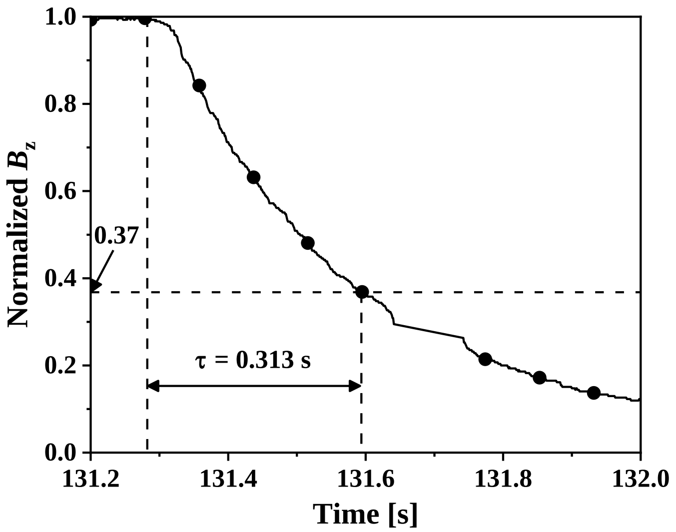

(a) Coil 1

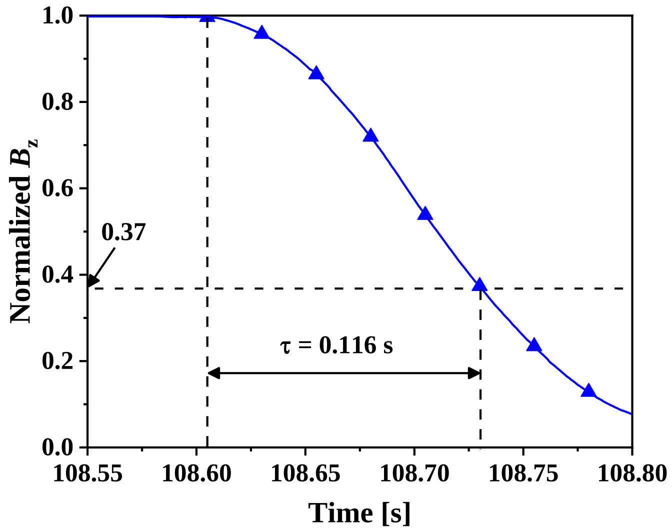

(b) Coil 2

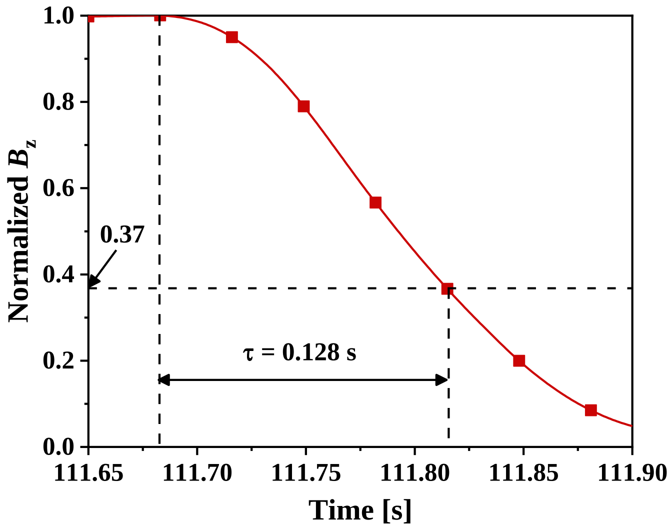

(c) Coil 3

Fig. 3.17. Sudden discharging tests at 0.7 I_c with current ramp rate of 1 A/s.

B. Sudden discharging test

To investigate τ and R_c of the three MI–SS racetrack coils, the sudden discharging tests were conducted under steady state operation in a bath of LN2 at 77 K. I_t was increased to 0.7 I_c (70 A for coils 1 and 3 and 73 A for coil 2) with a charging rate of 1 A/s. Then, I_t was maintained at that level so that all the test coils were in a steady state condition before the power supply was cut off abruptly. The center magnetic field of each coil under the sudden discharging tests can be expressed by the equation (23). Fig. 3.17 shows the results of the normalized B_z with respect to time curves for all the test coils: (a) coil 1, (b) coil 2, and (c) coil 3. The τ values of coils 1, 2, and 3, which were measured at a normalized B_z of 0.37 (i.e., $B_z/B_{z,0} = 1/e$ when $t = \tau$, as shown by the horizontal dashed line in Fig. 3.17), were 0.313, 0.116, and 0.128 s, respectively. From the results of τ, the R_c values of coils 1, 2, and 3, calculated by the ratio between L_c and τ (i.e., $R_c = L_c/\tau$), were 3.195, 8.621, and 7.813 mΩ, respectively. In general, the R_c of coil 1 was smaller than those of the coils 2 and 3. These results demonstrated that the R_c of the MI–SS racetrack coils was influenced by the winding tension and SS thickness between the turn–to–turn layers. Furthermore, R_c increased as the SS insulation thickness and winding tension decreased.

C. Charging test

The charging tests were performed under steady state operation in bath of LN2 at 77 K to investigate τ_d of the three MI–SS racetrack coils. I_t was increased to 0.6 I_c (60 A for coils 1 and 3 and 62 A for coil 2) with a charging rate of 1 A/s. Fig. 3.18 shows B_z, I_t, and V_t versus time curves for all test coils during the charging tests. V_t of the test coils increased rapidly and finally reached ~1 mV. The L_c of the three test coils was calculated to be ~1 mH, which was defined from the relationship between the inductive voltage (V_L) and the current ramping rate of 1 A/s, as shown in Fig. 3.18 ($V_L = L_c \times dI/dt$). When the operating current was maintained at 0.6 I_c, the B_z values of coils 1, 2, and 3 were 24.4, 25.8, and 25.6 mT, respectively. Moreover,

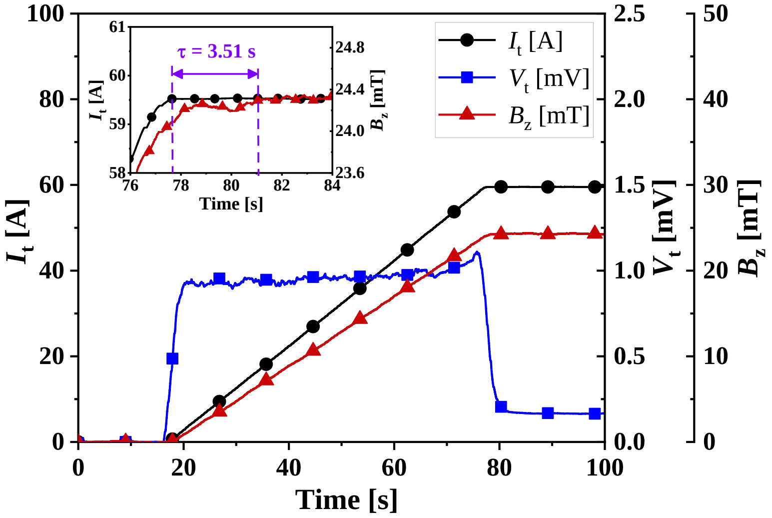

(a) Coil 1

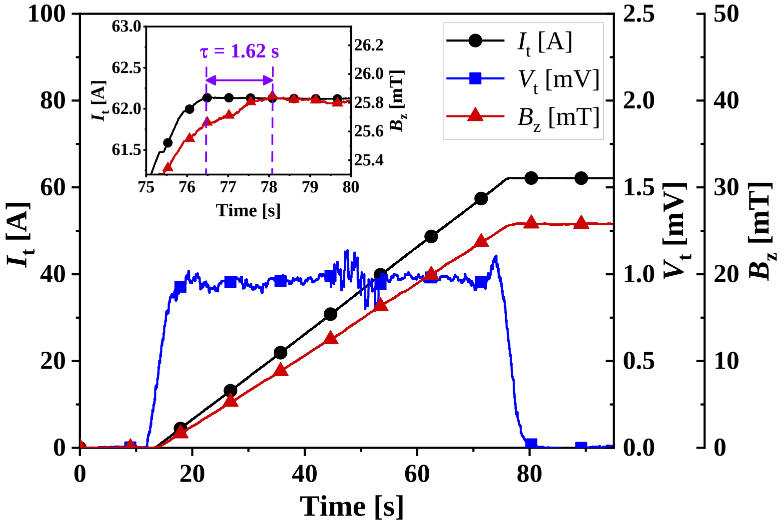

(b) Coil 2

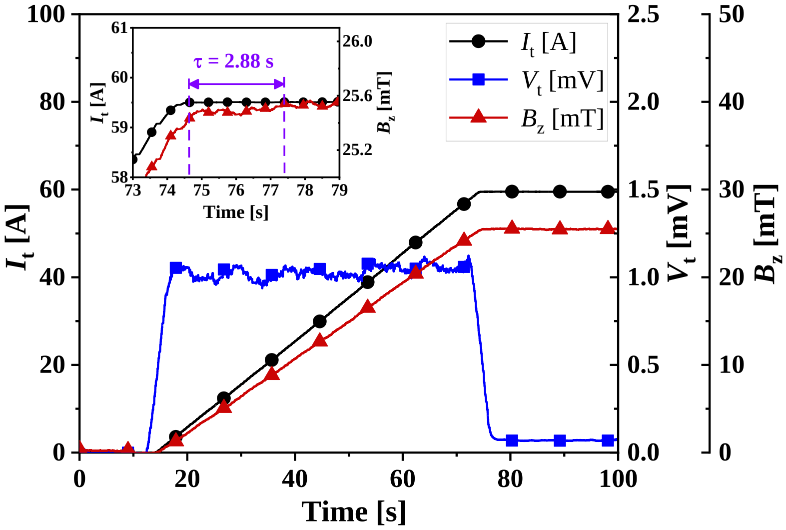

(c) Coil 3

Fig. 3.18. Charging tests at 0.6 I_c with current ramp rate of 1 A/s.

Table 3.4. Effects of winding tension and SS thickness on the charging time of MI–SS racetrack coils.

Impact factors	**Winding tension**	**Stainless steel thickness**	**Charging time**
Case 1	Constant	Increase	Increase
Case 2	Increase	Constant	Increase

the τ_d for coils 1, 2, and 3 reaching the expected magnetic field were 3.51, 1.62, and 2.88 s, respectively. At the same SS thickness of 100 μm, τ_d of coil 2 was 54% faster than that of coil 1, indicating that the decreasing winding tension can ameliorate the charging time behavior. Thus, the R_{ct} increased as the winding tension decreased, leading to an increase in R_c, which resulted in an improvement in τ_d. Similarly, at an identical winding tension of 10–kgf, τ_d of coil 3 was 18% faster than that of coil 1, suggesting that τ_d decreased with a decrease in SS thickness between the turn–to–turn layers. The reason may be that the contact surface of thinner stainless steel in coil 3 is rougher than that of coil 1, leading to an increase in R_c, which results in an improved τ_d. As discussed in chapter 2, R_c comes mostly from the turn–to–turn contact surface, because the R_{metal}, calculated by the equation (5), is very small (~ 0.43 nΩ for coil 1 and 0.22 nΩ for coil 3) compared with the R_{cs} (~ 3.195 mΩ for coil 1 and 7.813 mΩ for coil 3) due to the small value of the resistivity of stainless steel material at 77 K (~ 5.3×10^{-7} Ω.m). Thus, the R_{metal} between the turn–to–turn layers is very small and is considered to have an insignificant effect on R_c. In general, the R_{ct} depends mostly on the winding tension and the surface roughness between HTS and SS tapes [52], [67]. The effects of the SS thickness and winding tension on the τ_d behavior are shown in Table 3.4.

Fig. 3.19 shows the results of the three MI–SS racetrack coils at a current ramp rate of 5 A/s during the charging tests. The I_t, V_t, and B_z curves exhibited similar behaviors to those observed in the charging tests at a current ramp rate of 1 A/s. However, the V_t value of the test coils at a charging rate of 5 A/s was 5 mV, which was five times higher than that in the charging

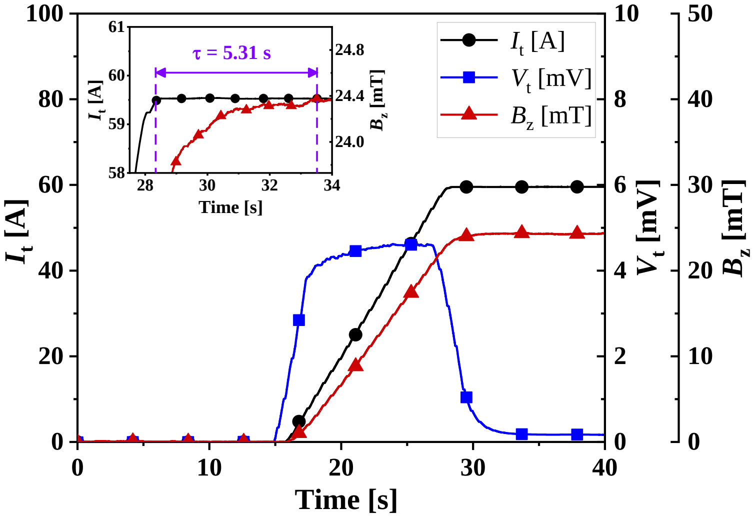

(a) Coil 1

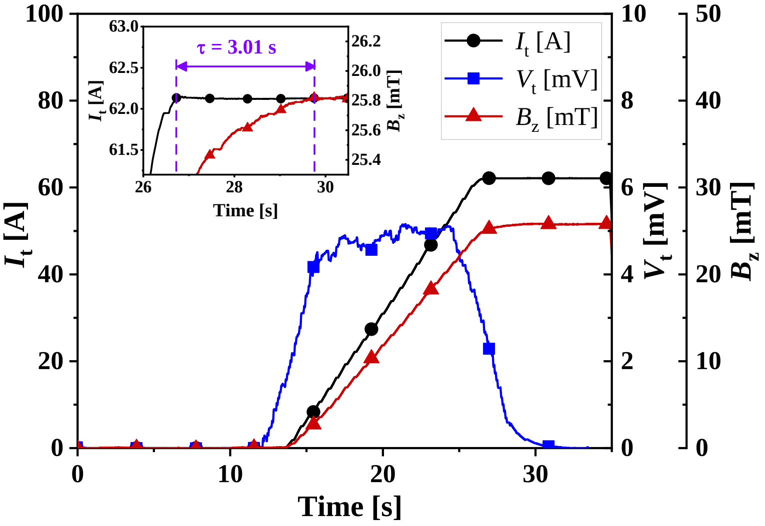

(b) Coil 2

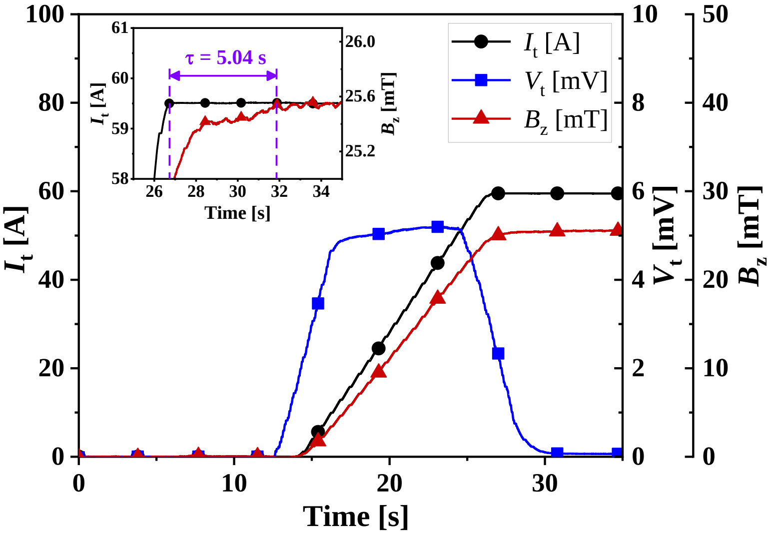

(c) Coil 3

Fig. 3.19. Charging tests at 0.6 I_c with current ramp rate of 5 A/s.

Table 3.5. Effects of current ramp rate on charging time of MI–SS racetrack coils.

Current ramp rate	**0.6 I_c_1 A/s**	**0.6 I_c_5 A/s**
τ_d of Coil 1 [s]	3.51	5.31
τ_d of Coil 2 [s]	1.62	3.01
τ_d of Coil 3 [s]	2.88	5.04

test at 1 A/s. Furthermore, the τ_d of coils 1, 2, and 3 were 5.31, 3.01, and 5.04 s, respectively, as shown in Fig. 3.19. Thus, the τ_d of these test coils also increased with the increase of the current ramp rate due to the bypass current phenomenon through turn–to–turn contact layers, which could be explained by the equation (1). It is assumed that L_c and R_c are constant values, and I_r increases according to the increase of dI/dt, leading to more I_s lag behind I_t, which causes more lagging of the magnetization. Table 3.5 shows a comparison of τ_d between the current ramp rate at 1 and 5 A/s for the three test coils. In addition, during the charging test at 5 A/s, the V_t (~5 mV) of the test coils was higher than V_c (~3 mV), resulting in the greater joule heat energy induced by the quench, which may cause less stable operation compared with the charging test at 1 A/s.

Fig. 3.20 shows I_t, V_t, and B_z versus time curves of the three test coils at 0.8 I_c (80 A for coils 1 and 3 and 83 A for coil 2) with a current ramp rate of 1 A/s during the charging tests. As the charging current increased to 0.8 I_c, the V_t of coil 1 (1.68 mV) and coil 3 (1.52 mV) increased over the inductive voltage of 1 mV, which was obtained from the charging test at 0.6 I_c with a current ramp rate of 1 A/s. This may be because quench unexpectedly occurred in a weak layer of the test coils, which caused more I_r flowing through the turn–to–turn contact layers, leading to an increase in V_t (i.e., $V_t = R_c \times I_r$). The saturated fields for coils 1, 2, and 3 at 0.8 I_c (32.6, 34.6, and 34 mT, respectively) were higher than those at 0.6 I_c (24.4, 25.8, and 25.6 mT, respectively). Additionally, the τ_d values of the test coils at 0.8 I_c exhibited a slight decrease compared with 0.6 I_c, as summarized in Table 3.6. This was because the R_{ct} increased

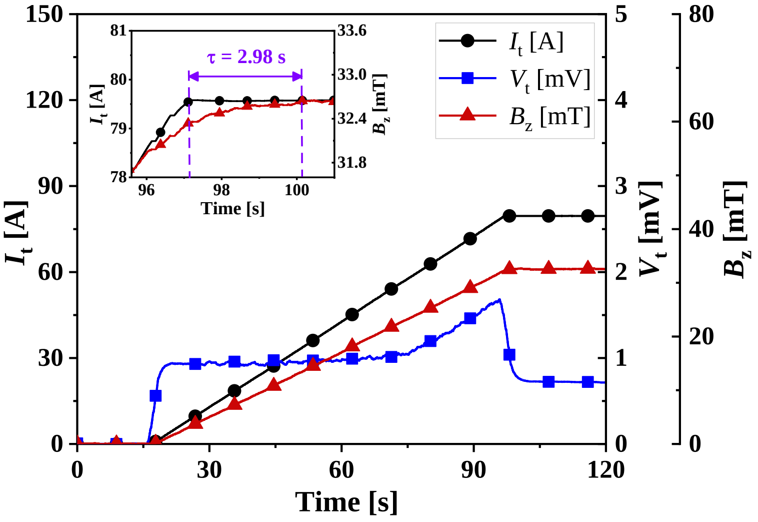

(a) Coil 1

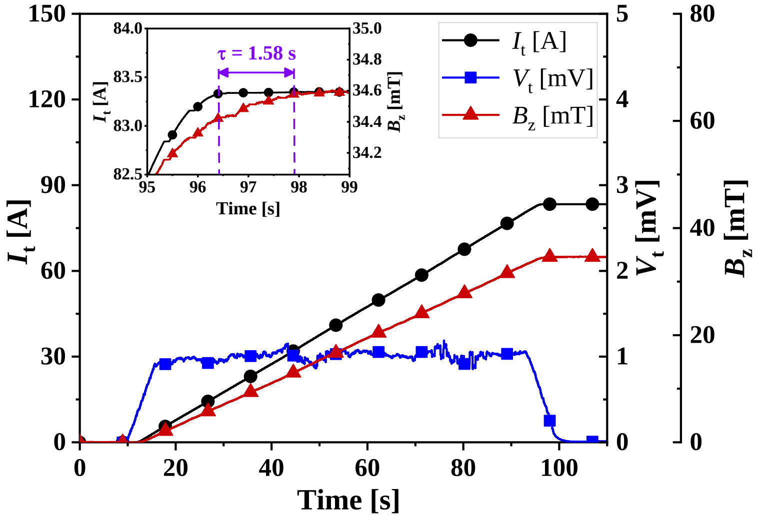

(b) Coil 2

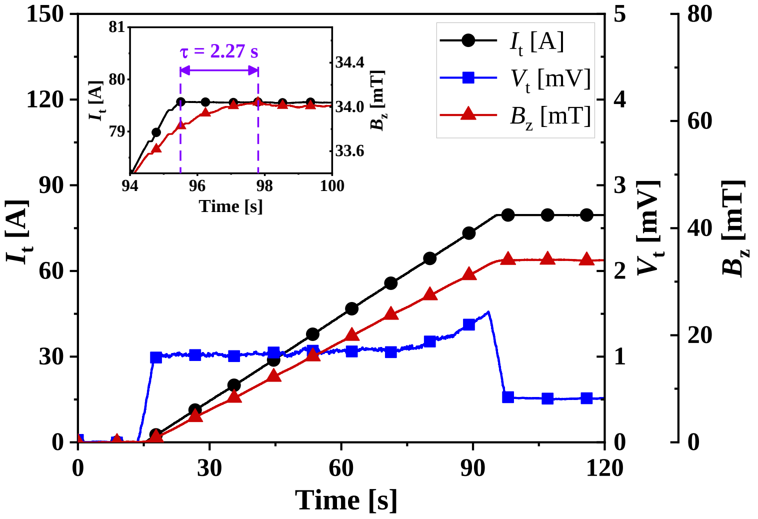

(c) Coil 3

Fig. 3.20. Charging tests at 0.8 I_c with current ramp rate of 1 A/s.

Table 3.6. Effects of current amplitude on charging time of MI–SS racetrack coils.

Current ramp rate	**0.6 I_c_1 A/s**	**0.8 I_c_1 A/s**
τ_d of Coil 1 [s]	3.51	2.98
τ_d of Coil 2 [s]	1.62	1.58
τ_d of Coil 3 [s]	2.88	2.27

with an increase in I_t as more joule heat energy was induced within the test coils [36]. As a results, τ_d of the MI–SS racetrack coils decreased with an increase in I_t. Overall, the charging test results demonstrated that the τ_d phenomenon of the MI–SS racetrack coils could be improved by decreasing the SS thickness and winding tension. Furthermore, the τ_d of the MI–SS racetrack coils were also affected by the current ramp rate and current amplitude. The τ_d of the test coils decreased with decreasing current ramp rate or increasing current amplitude. The operation of the test coils with a high current ramp rate and high current amplitude generated a high V_t during the charging tests because more bypass current flows through the turn–to–turn contact layers, resulting in low stability of the HTS magnets.

D. Overcurrent test

To investigate the thermal stability of three MI–SS racetrack test coils, overcurrent tests were performed in the transient state of 1.1 I_c (110 A for coils 1 and 3 and 114 A for coil 2) and 1.05 I_c (109 A for coil 2 and 105 A for coil 3) with an increment rate of 1 A/s. Fig. 3.21(a) shows the experimental results of V_t, B_z, and I_t versus time curves for coil 1 during the overcurrent test at 110 A. The V_t of coil 1 slowly started to increase below I_c value and rapidly reached the peak voltage ~5 mV. Then, V_t remained stable at maximum value as the operating current maintained at 110 A, implying that the joule heat energy induced by the excessive current was equilibrated by a LN2 cooling bath. When I_t decreased to zero, the V_t of coil 1 also decreased and finally reached zero, indicating that the test coil completely recovered; whereas the V_t of coils 2 and 3 increased over the protective voltage value that was set up to prevent

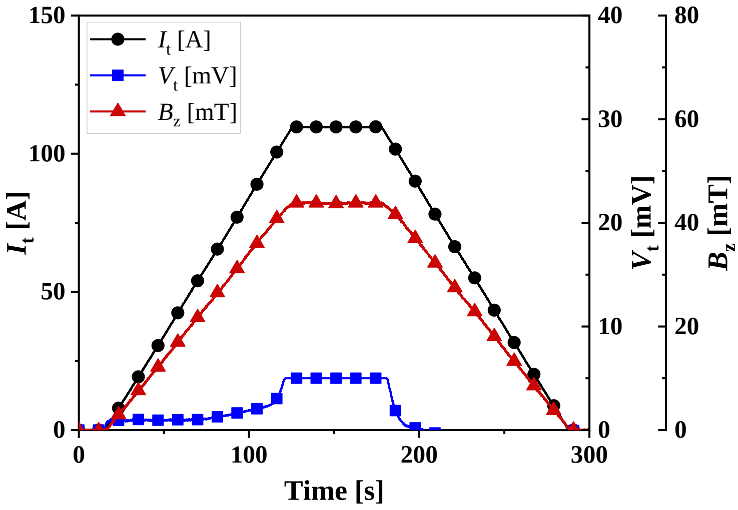

(a) Coil 1 at 1.1 I_c

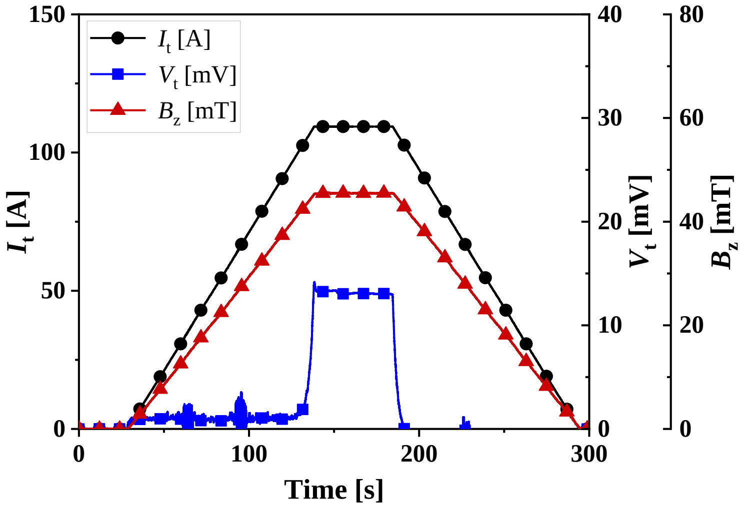

(b) Coil 2 at 1.05 I_c

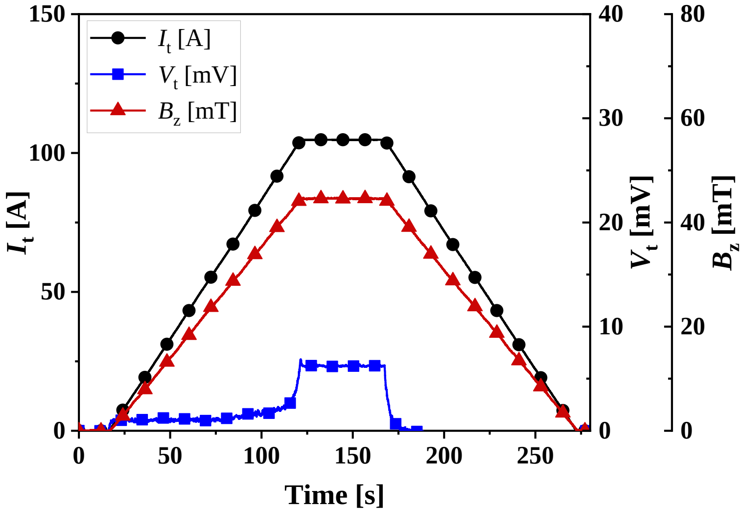

(c) Coil 3 at 1.05 I_c

Fig. 3.21. Overcurrent tests at 1.1 and 1.05 I_c with current ramp rate of 1 A/s.

Table 3.7. Effects of winding tension and SS thickness on the thermal stability of MI–SS racetrack coils.

Impact factors	Winding tension	Stainless steel thickness	Thermal stability
Case 1	Constant	Increase	Increase
Case 2	Increase	Constant	Increase

the test coils from permanent damage. Therefore, overcurrent tests were performed at 1.05 I_c to estimate the thermal stability of coils 2 and 3. Fig. 3.21 shows the experimental results of V_t, B_z, and I_t versus time curves during the overcurrent tests at 1.05 I_c (109 A for coil 2 and 105 A for coil 3). When I_t was maintained at 1.05 I_c, V_t of coils 2 and 3 remained at steady state values of 13.2 and 6.2 mV, respectively, which were higher than that of coil 1 (5 mV) at 1.1 I_c. These results demonstrated that the thermal stability of these test coils was affected by the winding tension and SS thickness between the turn–to–turn layers, as shown in Table 3.7. In general, coil 1 exhibited higher thermal stability than coils 2 and 3 owing to its thicker SS insulation and higher winding tension. This was because the greater winding tension in coil 1 could easily dissipate the joule heat energy induced by hot spots compared with that of coil 2. Similarly, compared with coil 3, the thicker SS insulation in coil 1 could enhance the heat capacity, which absorbed more joule heat energy generated by hot spots. Furthermore, coil 1 could easily divert the larger amount of excessive current through turn–to–turn contact layers because of its higher winding tension and smoother SS insulation compared to coil 2 and coil 3, respectively, resulting in less joule heat energy induced by hot spots. For further study, the effect of external magnetic field on the electrical and thermal characteristics of MI–SS racetrack coil should be investigated to optimize the operational performance because the 2G HTS field coils can be subjected to external magnetic field in practical wind generator application.

3.4. Fabrication and experiment of MI–SS racetrack coil according to various AC rotating magnetic field and cryogenic cooling system

In the practical superconducting rotating machine applications, although the superconducting coils are designed to operate on the direct current, they can be subjected to external magnetic field due to the unsynchronized armature windings during electrical or mechanical load fluctuations. The superconducting coils show the voltage and magnetic field fluctuations and the critical current reduction when they are exposed to the external magnetic field. Moreover, the cryogenic cooling conditions are also identified as the factor that affects to the electrical and thermal characteristics of the HTS coil because the R_c changes according to the cryogenic cooling conditions. Therefore, it is essential to investigate the effect of various external magnetic fields and cryogenic cooling conditions on the electrical and thermal characteristics of MI–SS racetrack coil for further development reliable 2G HTS field coils of the 10 MW class HTS generator.

This section presents the experiment and simulation results on the electrical and thermal behaviors of a MI–SS racetrack coil under rotating magnetic field. There were two main parts in the experiment test, such as cryostat and three phase armature windings. The MI–SS racetrack coil, which was cooled by conduction cooling system, was operated under external magnetic field generated by armature windings of a 75 kW class induction motor. The effects of external magnetic field on the electrical and thermal characteristics of MI–SS racetrack coil were adjusted by current amplitude and frequency. First, the major components of the experiment test, such as MI–SS racetrack coil, armature windings of asynchronous rotating machine, and conduction cooling system, were fabricated and assembled. Then, the *I*–*V* tests for MI–SS racetrack coil were performed in various cryogenic cooling conditions, i.e., LN2 bath and conduction cooling of 35 and 77 K, to estimate the I_c value for the test coil. In addition, to investigate the effect of cryogenic cooling on the R_c and τ_d for MI–SS racetrack coil, the charging and discharging tests were conducted in the LN2 bath and conduction cooling conditions. Furthermore, the test coil was charged to the target value under conduction cooling of 35 K then exposed to the rotating magnetic field to estimate the electrical and thermal characteristics during the transient state. The critical current and magnetic field of the MI–SS racetrack coil were analyzed and discussed according to the variation in external magnetic field.

3.4.1. Experiment setup

A. Construction of MI-SS racetrack coil

The major parameters of the REBCO coated conductor, which was manufactured by SuNAM Co., Ltd., and the MI–SS racetrack coil are listed in Table. 3.8. The width and thickness of the REBCO tape are 12.1 mm and 0.14 mm, respectively. The racetrack bobbin was made of stainless steel with outer diameter at curvature of 40 mm and straight section of 140 mm, as shown in Fig. 3.22. The thickness of stainless steel tape used between turn–to–turn layers was 120 μm. During fabrication the MI–SS racetrack coil, the winding tensions for 2G HTS and SS tapes were maintained at 10 and 5 kgf, respectively. The center bore and shoe cover were made of carbon steel (S45C) to concentrate and increase the magnetic field. The test coil was wound directly onto the center bore of SS racetrack bobbin and covered by conduction guide with oxygen–free high conductive copper (OFHC) to enhance heat transfer characteristic of conduction cooling system. The various signal sensors were utilized to measure the electromagnetic behaviors during coil operation. Three voltage taps (V_1 – V_3) were installed in every ten turns, starting from the innermost turn, and terminal voltage tap (V_T) was inserted between two terminals to measure the voltage signal in the steady and transient states. In addition, a Hall sensor was located at the bobbin center to measure the center magnetic field density of the test coil.

Table 3.8. Parameters of REBCO tape and MI–SS racetrack coil.

Items	Unit	Values
REBCO Coated Conductor Tape		
Manufacturer	–	SuNAM Co. Ltd
Conductor model	–	SCN12500
Conductor width	[mm]	12.1 ± 0.1
Conductor thickness	[µm]	140 ± 15
Min I_c at 77 K, self–field*	[A]	676
Max I_c at 77 K, self–field*	[A]	808
Critical temperature	[K]	91
MI–SS Racetrack Coil		
Number of turns	–	32
Material insulation	–	SS 310S
Material bobbin	-	Copper and S45C
Insulation thickness	[µm]	120
Conductor length	[m]	17.8
Inner radius at curvature	[mm]	40
Outer radius at curvature	[mm]	48.64
Length of straight portion	[mm]	140
I_c at 77 K, self–field *	[A]	239
Critical voltage	[mV]	1.78
Characteristic resistance	[µΩ]	144.3
Contact resistance	[µΩ.cm^2]	304.7
Winding tension of REBCO	[kgf]	10
Winding tension of SS	[kgf]	5
Coil inductance	[µH]	577

* Measured using 1–µV/cm criterion

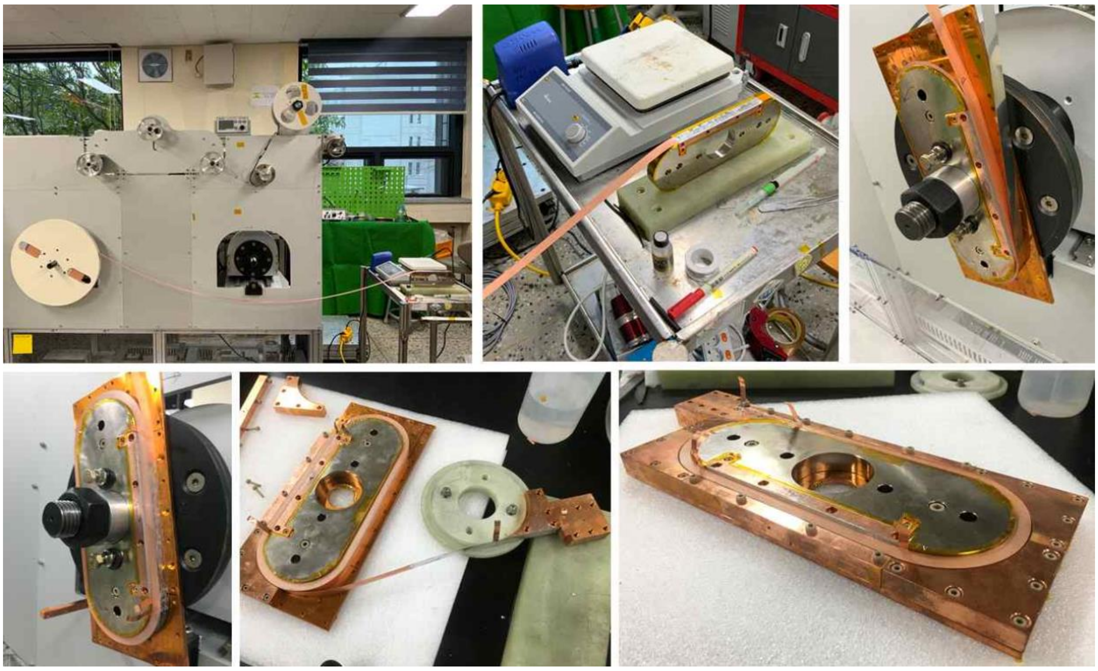

Fig. 3.22. Photographs of MI–SS racetrack coil.

B. Fabrication of conduction cooling system integrated MI-SS racetrack coil

The MI–SS racetrack coil was placed inside the cryostat part in vertical direction as shown in Fig. 3.23. A pair of HTS current leads were utilized to supply the operating current into the test coil with minimizing heat intrusion. Each current lead included two 2G HTS tapes, which are the same properties with 2G HTS tape used to fabricate the test coil, and fiber reinforced plastic sheets to insulate and protect the HTS tapes. The inlet of both HTS current leads were connected to the first–stage of cryocooler. Both HTS current leads were cooled down to approximately 80 K, which can transport I_t of 1352 A (= 2 × 676 A) into the test coil. The test coil was electrically closed with two HTS current leads through OFHC terminal lead blocks. Then, they were thermally connected with the second–stage of cryocooler through conduction structure (i.e., OFHC–bars and –braided wires) to cool down the test coil to 35 K. Cernox® , DT–670 Silicon Diodes, and PT–1000 sensors were attached at various locations inside cryostat to measure the temperature, as shown in Fig. 3.24. In addition, to reduce thermal radiation from room temperature, thermal shield cylinder with multi–layer insulation of aluminum foil was utilized to cover all structures below the first–stage of cryocooler, as shown in Fig 3.23. The configuration of 75 kW class induction motor, which was used to generate AC external magnetic field on the MI–SS racetrack coil, is shown in Fig. 3.25. The length of stator core, inner and outer diameters of induction motor were 214, 281 and 435 mm, respectively. The stator had 72 slots and double layer windings. During the experiment tests,

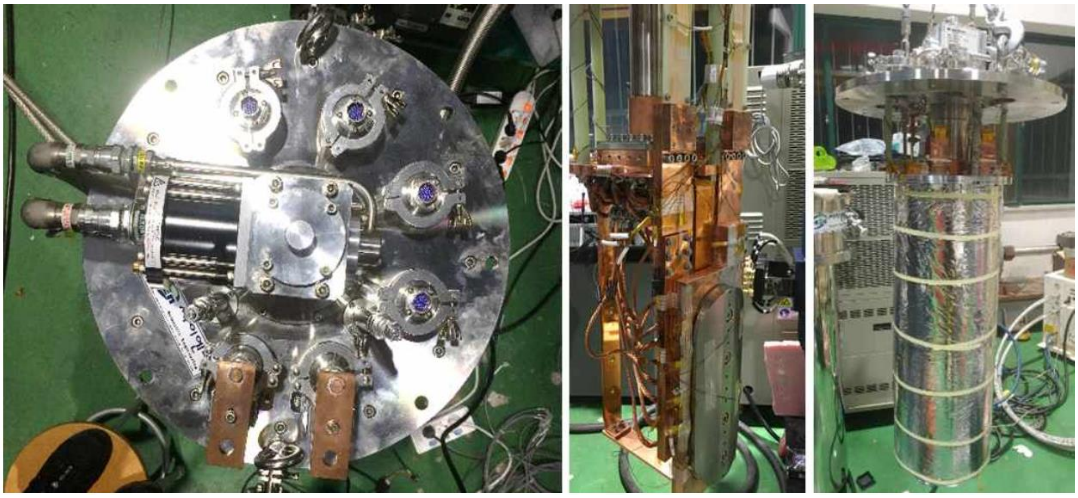

Fig. 3.23. Photographs of assembly MI-SS racetrack coil into conduction cooling system.

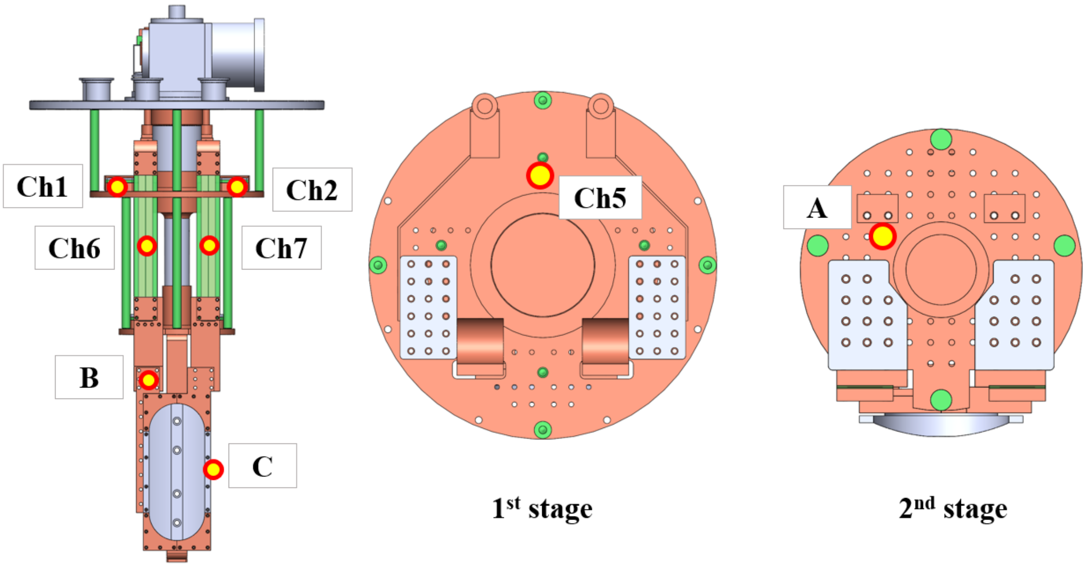

Fig. 3.24. Schematic drawings of cryostat part with position of temperature sensors.

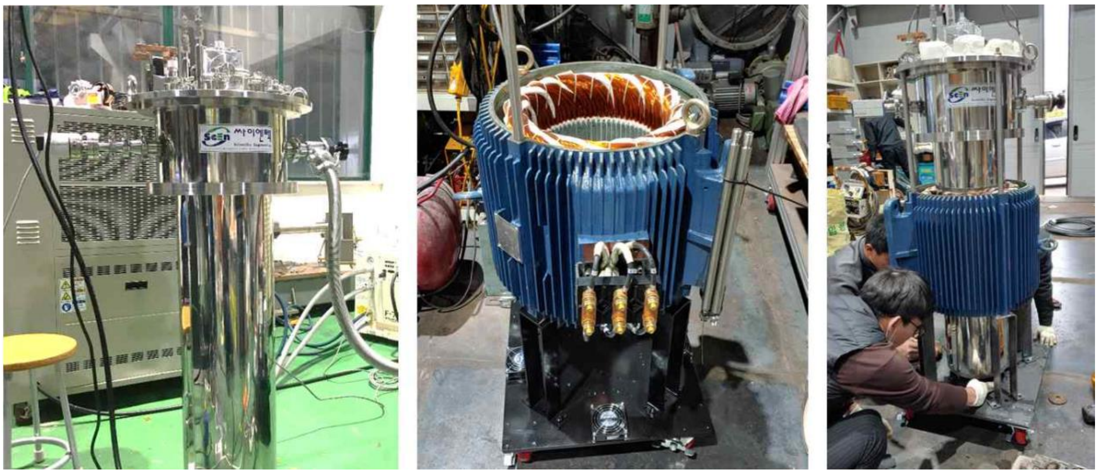

Fig. 3.25. Photographs of assembly cryostat part into induction motor.

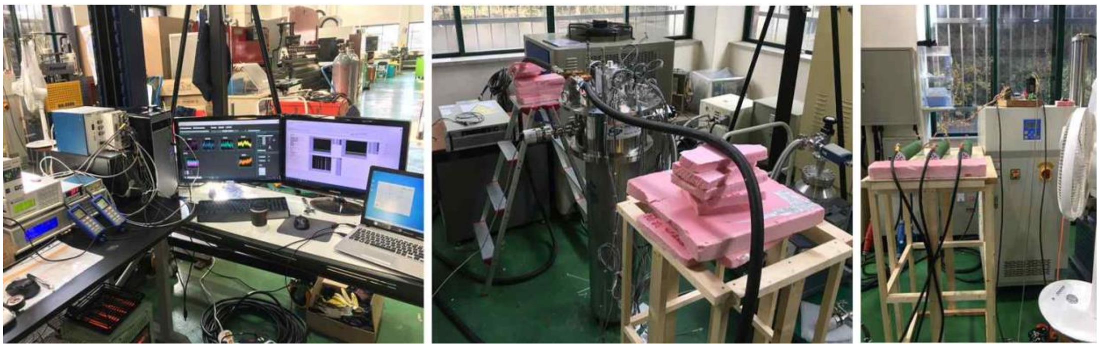

Fig. 3.26. Photographs of experiment setup.

the external magnetic field, which was generated by three phase armature windings, was controlled by the frequency and current amplitude. The MI–SS racetrack coil was placed parallel to the three phase armature windings to investigate the effect of external magnetic field on the I_c and B_z of the test coil, as shown in Fig. 3.25. A data acquisition system was used to measure the B_z, V_t, and temperature fluctuations according to the variation of external magnetic field generated by a 75 kW class three phase armature windings, which was controlled by variable voltage and frequency inverter. The experiment setup for estimating on the electrical and thermal characteristics of MI–SS racetrack coil under rotating magnetic field is shown in Fig. 3.26.

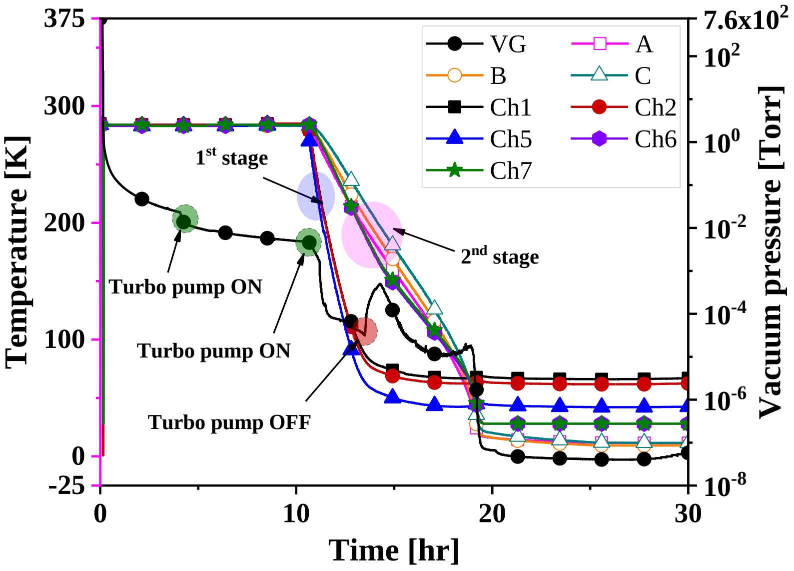

(a) Cool down temperature

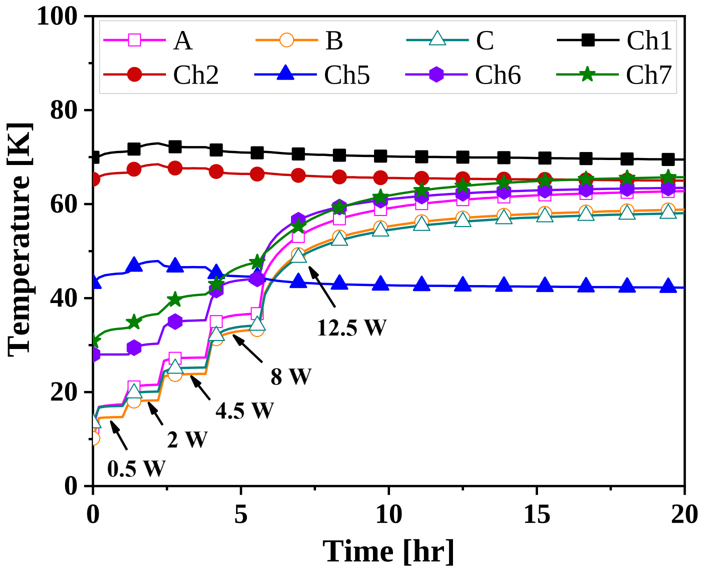

(b) Temperature variation according to heater power

Fig. 3.27. Experiment results under cooling and vacuum tests.

3.4.2. Results and discussion

A. Cooling and vacuum test

Fig. 3.27(a) shows the experiment results of vacuum and cool down temperature during the 1st and 2nd stages of cryocooler. It took around 13 and 19 hours to reach the steady state temperature for the 1st and 2nd stages, respectively. The vacuum pressure was decreased to 4.7

$\times 10^{-3}$ Torr using a turbo molecular pump. Then, the cryocooler started to reduce the vacuum pressure as well as temperature inside the cryostat part. For beginning hours, the temperature inside the cryostat part remained stable at room temperature. Subsequently, the temperature of the test coil was maintained at 10 K under vacuum pressure of 4.06×10^{-8} Torr during around 15 hours after turning on the cryocooler, as shown in Fig. 3.27(a).

Fig. 3.27(b) shows experiment result of temperature variation with respect to joule heat generation by heater power of 50 Ω, which was installed at the 2nd stage of the cryocooler. The temperature of the stages could be controlled by this heater power. However, the electrical and thermal characteristics of the test coil were not affected by the operation of heater power because they had a separate thermal link model and most of heat generation by heater power was absorbed by the cryocooler. When the heater power was zero, the temperature of the 2nd stage remained at 10 K. To maintain the target operating temperature of 35 and 77 K for the MI-SS racetrack coil, the heater power of 9.245 and 15.125 W were respectively supplied to the cryocooler, as shown in Fig. 3.27(b).

B. Current–voltage test

To investigate the I_c value for the MI–SS racetrack coil, the I–V tests were performed in the LN2 bath and conduction cooling conditions. The test coil was charged with the current ramp rate of 1 A/s until the V_t increased over the V_c of 1.78 mV which was calculated by multiplying the total length of HTS tape and the electric field criterion of 1–μV/cm. Then, the power supply current was turned off to prevent the test coil from permanent damage. In the LN2 bath of 77 K, the I_c value of the test coil was measured as 239 A, as shown in Fig. 3.28(a). In addition, the I–V tests were conducted under conduction cooling condition of 77 and 35 K to investigate the I_c value. Fig. 3.28(b) shows the experiment result of I_c value for the MI–SS racetrack coil under conduction cooling of 77 K. The I_c value of the test coil was estimated to be 236 A. However, the I_c value under conduction cooling of 35 K was assumed to be 500 A due to the limitation of power supply current, as shown in Fig. 3.28(c). It should be noted that the I_c value

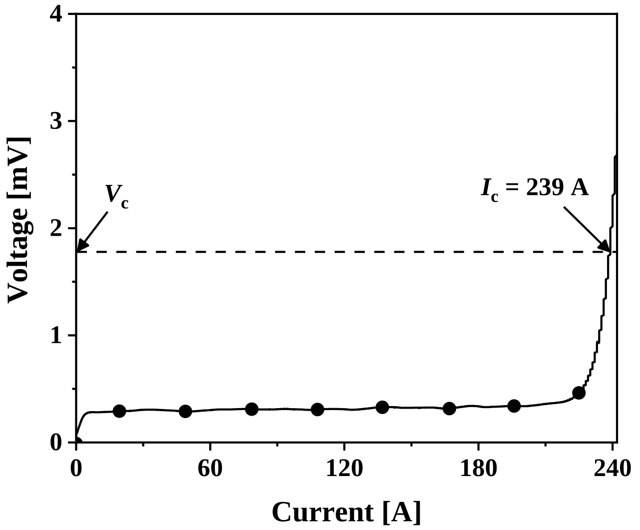

(a) LN2 bath cooling

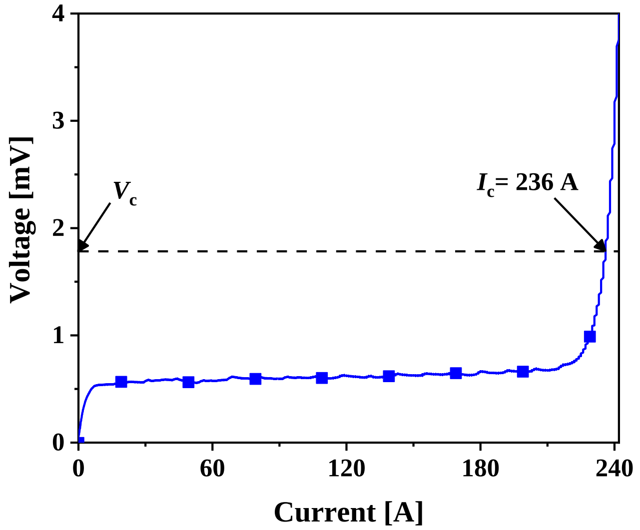

(b) Conduction cooling of 77 K

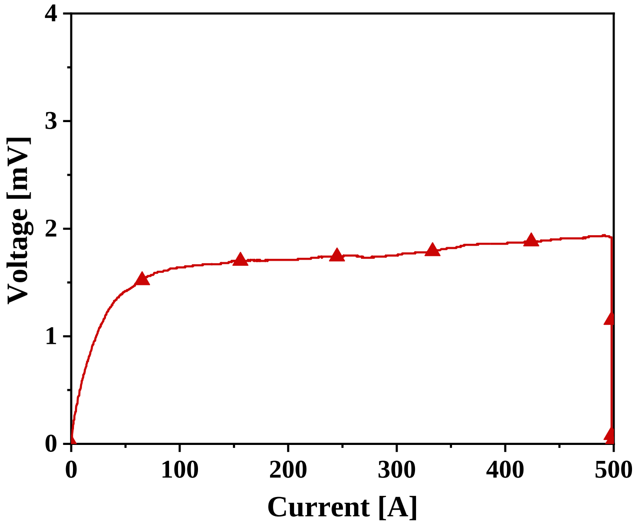

(c) Conduction cooling of 35 K

Fig. 3.28. Critical current results of MI–SS racetrack coil.

under conduction cooling of 35 K may exceed 500 A because the V_t did not increase over the V_c of 1.78 mV.

The numerical analysis was suggested to investigate the I_c value for the MI–SS racetrack coil using electromagnetic finite element analysis (FEA). The I_c value is well known to be decreased when the HTS coated conductor operates under magnetic field. The reduction of I_c value changes according to the incidence angle of magnetic field. In general, the I_c value decreases significantly under the perpendicular magnetic field. Fig. 3.29 shows the I_c value reduction according to perpendicular flux density of 2G HTS tape manufactured by SuNAM Co., Ltd. To analyze the magnetic field distribution in the MI–SS racetrack coil, the 3D FEA model is developed using the Ansys Mawell software. The test coil is charged to 500 A which is equal to the limitation value of the experimental power supply current. Based on the analysis of magnetic field distribution in the test coil, the simulation results of the I_c value according to the perpendicular magnetic field under conduction cooling of 77 and 35 K are estimated, as shown in Fig. 3.30. The I_c value is determined at the intersection point between the transport current and critical current at perpendicular flux density. The I_c value under the conduction cooling of 77 K is estimated as 245 A which is 2.45% and 3.67 % higher than those of experimental results obtained from LN2 bath and conduction cooling conditions of 77 K, respectively. In the case of conduction cooling of 35 K, the I_c value for the test coil is evaluated over 500 A which is similar to the experiment result. Overall, the simulation results were in good agreement with the experimental results, which proved that the validity of the developed 3D FEA model.

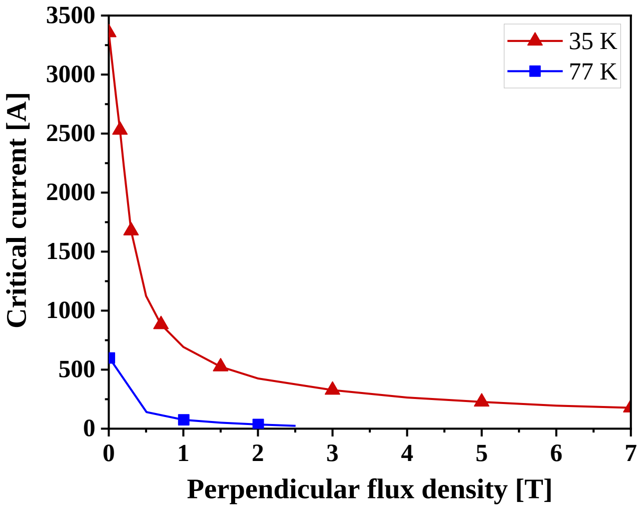

Fig. 3.29. Reduction of I_c value according to perpendicular flux density

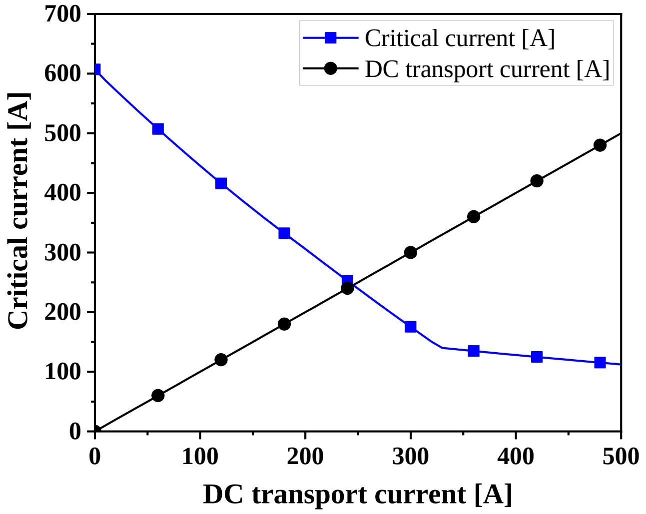

(a) Conduction cooling of 77 K

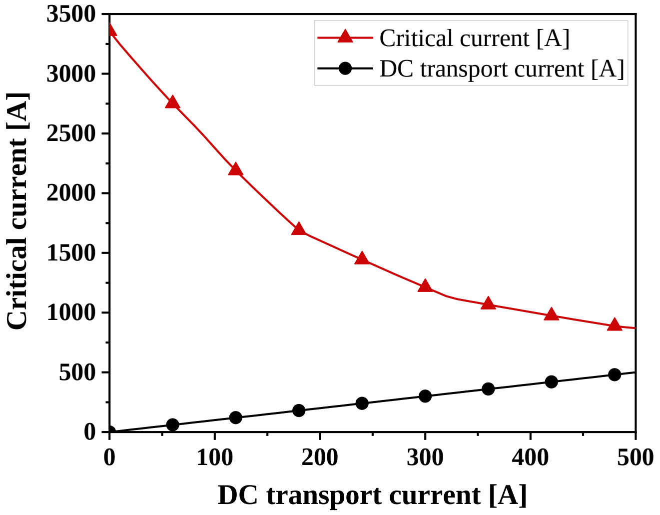

(b) Conduction cooling of 35 K

Fig. 3.30. Simulation critical current results of MI–SS racetrack coil.

C. Charging and discharging test

To characterize τ and R_c for the MI–SS racetrack coil, the charging and discharging tests were performed under the LN2 bath and conduction cooling conditions. I_t increased up to 221 A with charging rate of 0.6 A/s under LN2 bath and 1 A/s under conduction cooling. Then, I_t was maintained at that level so that the test coil was in a steady state condition. Finally, I_t was decreased to zero with discharging rate of 0.6 A/s under LN2 bath and 1 A/s under conduction cooling. Fig. 3.31 shows the experiment results of the I_t and V_t under LN2 bath and conduction cooling of 77 and 35 K. τ of the test coil under LN2 bath and conduction cooling of 77 and 35 K, which was determined at a normalized V_t value of 0.632 (i.e., 0.224 V under LN2 bath, 4.16 V under conduction cooling of 77 K, and 0.369 V under conduction cooling of 35 K), were 4, 4, and 9 s, respectively. Based on the inductive voltage and current ramp rate (i.e., $V_L = L_c \times di/dt$), the L_c of the test coil under LN2 bath and conduction cooling of 77 and 35 K were estimated to be 577, 641, and 580 μH, respectively. Furthermore, the R_c of the test coil under conduction cooling of 35 K (64.4 μΩ), which was calculated using the values of L_c and τ (i.e., $R_c = L_c/\tau$), was smaller than those of LN2 bath of 77 K (144.3 μΩ) and conduction cooling of 77 K (160.3 μΩ). These results demonstrated that the R_c decreased as the temperature cooling decreased because joule heat generation inside the MI–SS racetrack coil was effectively eliminated at low temperature. However, at the same temperature cooling of 77 K, the R_c under LN2 bath was smaller than that of conduction cooling condition. This was because the LN2 bath could effectively cover the contact surface between turn–to–turn layers of the test coil, resulting in the enhancement of cooling performance, which eliminated more joule heat energy generated by bypass current through the neighboring turns. Table 3.9 summarizes the experiment results of τ, L_c, and R_c for MI–SS racetrack coil under the charging and discharging tests with respect to LN2 bath and conduction cooling conditions.

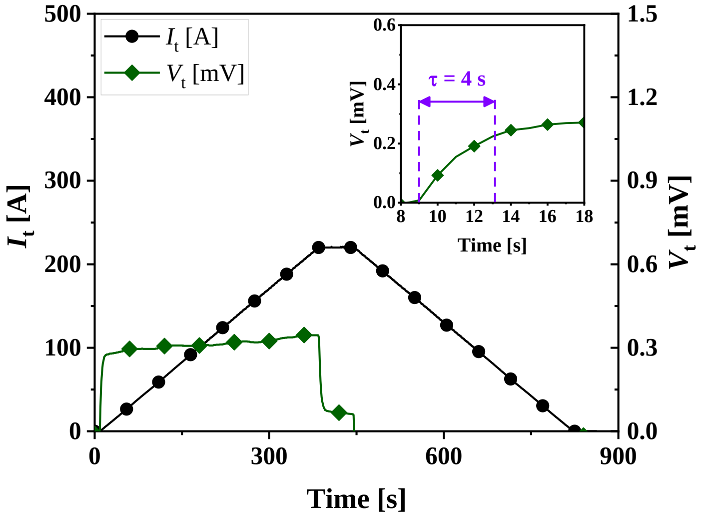

(a) LN2 bath cooling

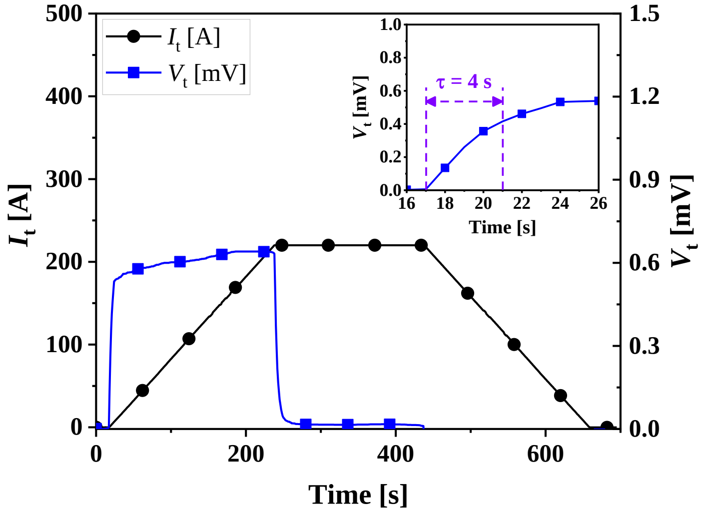

(b) Conduction cooling of 77 K

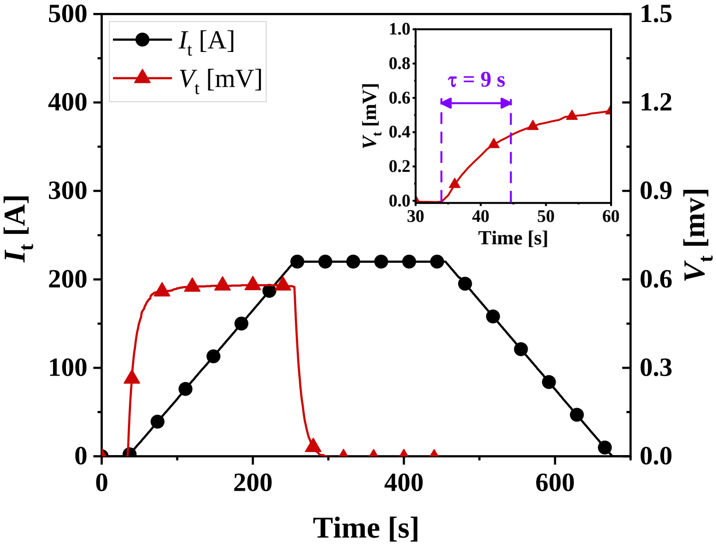

(c) Conduction cooling of 35 K

Fig. 3.31. Time constant results of MI–SS racetrack coil at 221 A.

Table 3.9. Experiment results of the test coil under LN2 and conduction cooling.

Items	**Unit**	**Values**		
Cooling approach	-	LN2	Conduction	Conduction
Temperature (K)	[K]	77	77	35
Inductance (μH)	[μH]	577	641	580
Time constant	[s]	4	4	9
Characteristic resistance	[μΩ]	144.3	160.3	64.4

Fig. 3.32 shows the experiment results of I_t, V_t, and B_z versus time curves under LN2 bath (Case 1) and conduction cooling of 77 K (Case 2) and 35 K (Case 3). The V_t of Cases 1, 2, and 3 increased and finally reached maximum voltages of 0.346, 0.641 and 0.58 mV, respectively. Moreover, when I_t maintained constant at 221 A, the B_z of Cases 1, 2, and 3 were 17.4, 17.5 and 17.44 mT, respectively. The τ_d values for Cases 1, 2, and 3 were 18, 14 and 28 s, respectively. As expected, the τ_d for Case 3 was slower than those of Cases 1 and 2. This was because the test coil under Case 3 could enhance the heat dissipation owing to its high performance cooling, which resulted in a decrease in R_c. Thus, the conduction cooling system of 35 K can be considered as an effective method for improving the electrical and thermal stabilities of the test coil under transient operating conditions.

Fig. 3.33 shows the temperature results inside the cryostat part during the charging and discharging tests under conduction cooling of 77 and 35 K. The positions of temperature sensors were shown in Fig. 3.24. The temperature at the channel C, which measured the temperature signal for the test coil, were maintained around 77 and 35 K, as shown in Fig. 3.33, implying that the joule heat generation during the test was equilibrated with the conduction cooling.

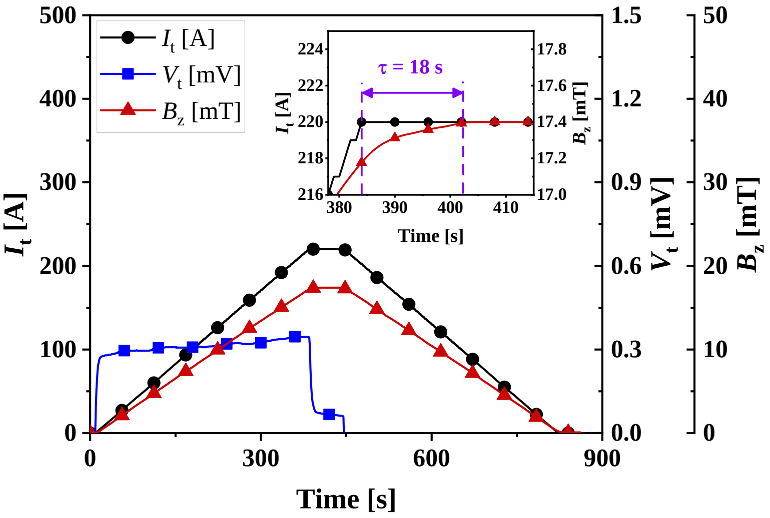

(a) LN2 bath cooling

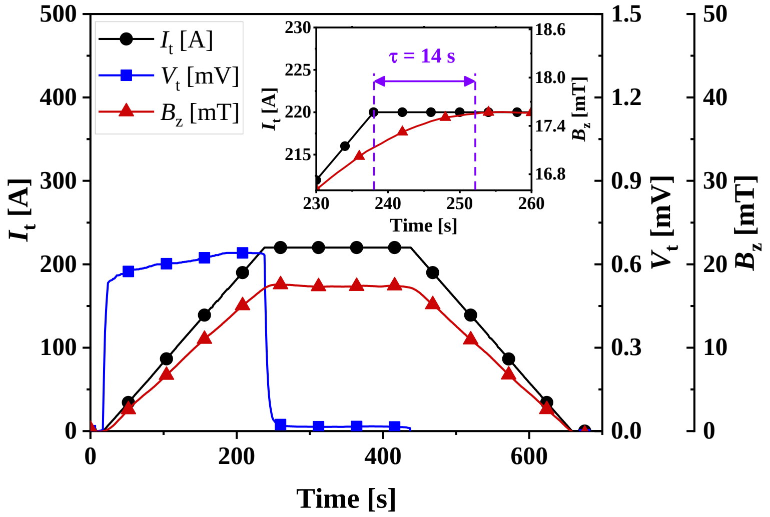

(b) Conduction cooling of 77 K

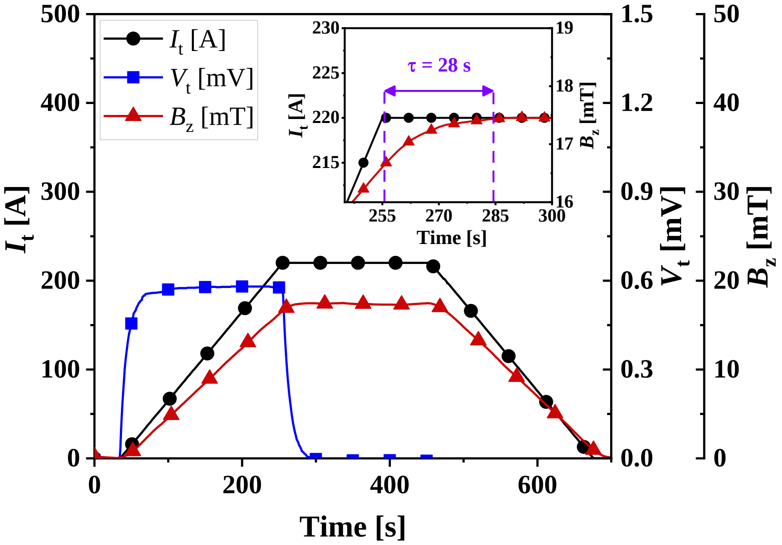

(c) Conduction cooling of 35 K

Fig. 3.32. Charging delay time results of MI–SS racetrack coil at 221 A.

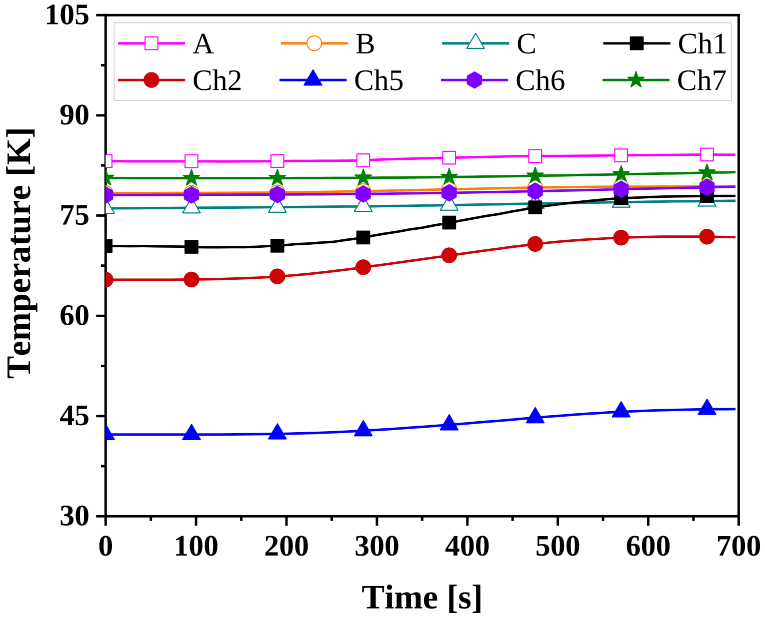

(a) Conduction cooling of 77 K

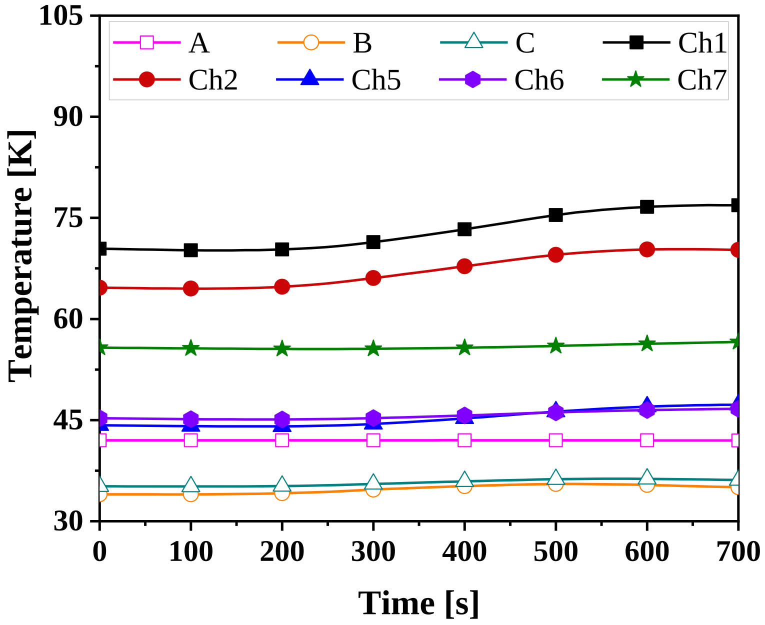

(b) Conduction cooling of 35 K

Fig. 3.33. Temperature results of MI–SS racetrack coil at 221 A.

D. Characteristic test under various AC rotating magnetic field

To investigate the effect of external magnetic field on the I_c characteristic of the test coil cooled by the conduction cooling system of 35 K, the transient tests were performed under various AC rotating magnetic field generated by three phrase armature windings. The armature current (i.e., 28.5, 42.5, and 57.6 A_{rms}) and frequency (i.e., 0.5, 1, and 1.5 Hz) were utilized to generate the rotating magnetic fields. As discussed in the I–V tests, the experimental I_c value under conduction cooling of 35 K was not estimated according to terminal voltage curve due to the limitation of power supply current of 500 A. However, the numerical approach was suggested to evaluate I_c value by using electromagnetic FEA model. The results under conduction cooling of 77 K demonstrated that the numerical approach is valid to estimate the I_c of the MI–SS racetrack coil. Therefore, the numerical approach was utilized to characterize I_c value for the test coil under rotating magnetic field and conduction cooling of 35 K. When the armature current and frequency of 28.5 A_{rms} and 0.5 Hz (Case 1), 42.5 A_{rms} and 1 Hz (Case 2), and 57.6 A_{rms} and 1.5 Hz (Case 3) were applied to the test coil, the I_c values were 421, 416, and 413 A, respectively. Although the accuracy of I_c value under conduction cooling system of 35 K cannot be obtained by the experiment approach due to the limitation of the power supply current, the effect of rotating magnetic field on the I_c characteristic under conduction cooling of 35 K may be investigated by the experiment tests based on the trend curves of I_t and B_z due to current bypass phenomenon. It is assumed that the I_c value of the test coil is 500 A which is the maximum value of power supply current. Fig. 3.34 shows the experiment results of the test coil under AC excitation in armature windings according to Cases 1, 2, and 3. It is noted that the B_z curve shows only the trend of center magnetic field for the test coil due to heavy noise. In Case 1, the magnetic field started to decrease at the I_t value of 497 A which was higher than those of Case 2 (463 A) and Case 3 (433 A). The experimental results demonstrated that the I_c value of the test coil was affected by the rotating magnetic field. The I_c value decreased as the rotating magnetic field increased.

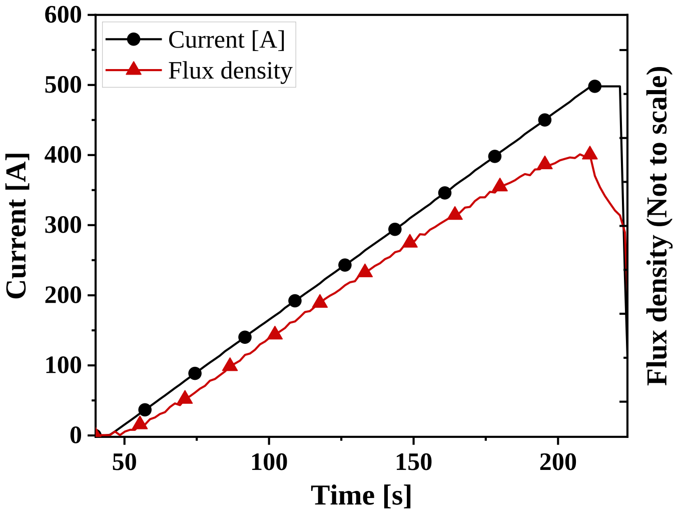

(a) 28.5 Arms and 0.5 Hz

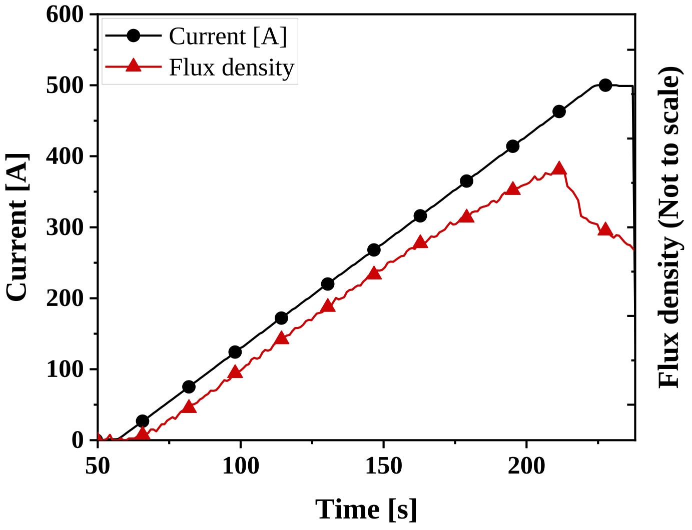

(b) 42.5 Arms and 1 Hz

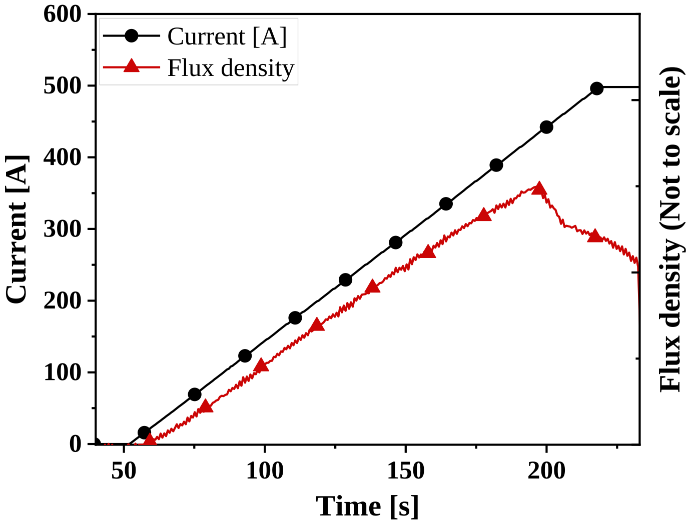

(c) 57.6 Arms and 1.5 Hz

Fig. 3.34. Test results of MI–SS racetrack coil under external magnetic field.

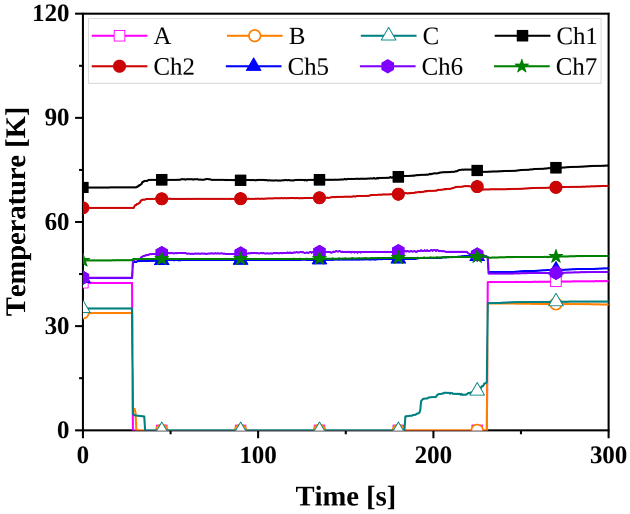

(a) 28.5 Arms and 0.5 Hz

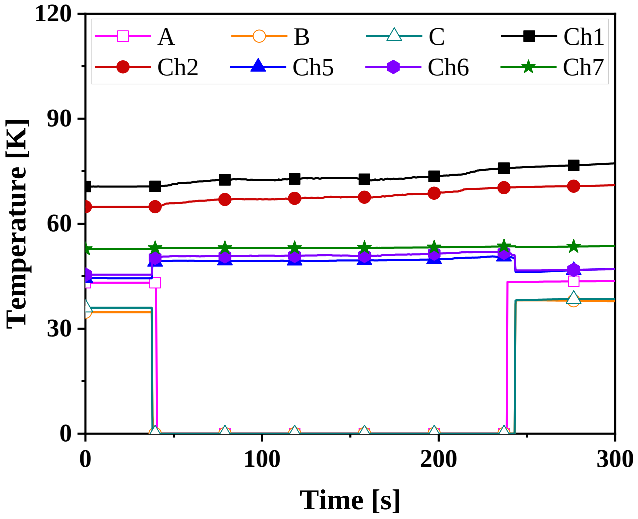

(b) 42.5 Arms and 1 Hz

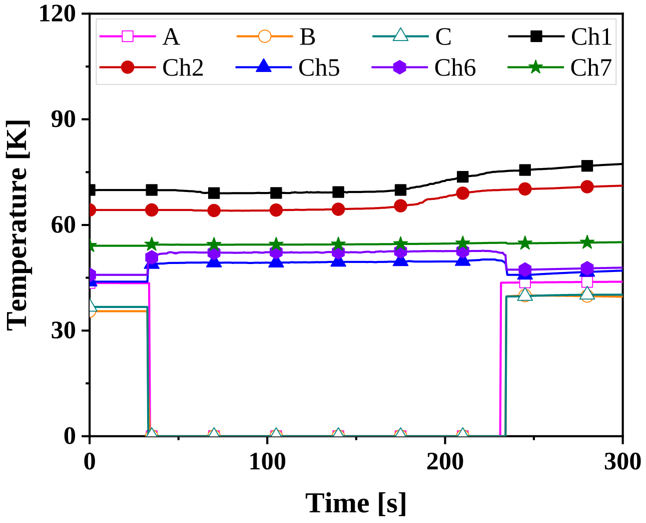

(c) 57.6 Arms and 1.5 Hz

Fig. 3.35. Temperature results of MI–SS racetrack coil under external magnetic field.

The temperature sensors were installed at the positions inside cryostat part as shown in Fig. 3.24. The experiment temperature results for Cases 1, 2, and 3 were shown in Fig. 3.35. When the external magnetic field applied to the test coil, the temperature channels A, B, and C were decreased to zero. However, the temperature channels Ch1, Ch2, and Ch7 operated normally during the experiment test. This is because the temperature sensors are affected by the three phrase armature windings. The magnitude of this effect depends on the distance between the temperature sensors and armature windings. Thus, the temperature channels A, B, and C were installed inside the armature windings of 75 kW class induction motor, resulting in a stronger effect than those of Ch1, Ch2, and Ch7, which were located far enough to avoid signal interference. Therefore, the initial and final temperature values of these channels were utilized to estimate the influence of the external magnetic field on the temperature characteristic for the cryostat part. In general, the average temperature was increased approximately 3 K for all the experiment tests. The temperature at all positions in Case 3 was higher than those of Cases 1 and 2. Overall, the temperature inside cryostat part increased as the current amplitude and frequency of external magnetic field increased, leading to the decrease of stable operation for the test coil. Table 3.10 summarizes the variation of temperature at all positions inside cryostat part during the characteristic test under conduction cooling of 35 K and various AC external magnetic field.

Table 3.10. Temperature results of MI–SS racetrack coil under external magnetic field.

(a) 28.5 Arms and 0.5 Hz			
Channel Name	**Position**	**Temp. (K)**	**Temp. (K)**
A	2nd stage	42.5001	42.9839
B	Coil lead block	33.8396	36.1214
C	Coil lead block	35.1186	37.0762
Ch1	1st stage lead block	69.9530	76.6670
Ch2	1st stage lead block	64.0740	70.6020
Ch5	1st stage	43.8540	46.9370
Ch6	HTS lead	43.9780	45.8000
Ch7	HTS lead	48.9380	50.4240
(b) 42.5 Arms and 1 Hz			
A	2nd stage	43.1494	43.6700
B	Coil lead block	34.6806	37.4293
C	Coil lead block	35.9915	38.4614
Ch1	1st stage lead block	70.6140	78.1870
Ch2	1st stage lead block	64.8360	71.5280
Ch5	1st stage	44.4030	47.7620
Ch6	HTS lead	45.4450	47.3860
Ch7	HTS lead	52.7300	53.8910
(c) 57.6 Arms and 1.5 Hz			
A	2nd stage	43.5001	44.0231
B	Coil lead block	35.4902	39.0516
C	Coil lead block	36.7115	40.0126
Ch1	1st stage lead block	69.9170	78.5560
Ch2	1st stage lead block	64.2500	71.8470
Ch5	1st stage	43.9010	47.9130
Ch6	HTS lead	45.8320	48.4590
Ch7	HTS lead	54.0960	55.5150

Chapter 4. Analysis on Electrical Characteristics of MI–SS 2G HTS Field Coils for 10 MW Class Wind Generator

4.1. Parameters of 2G HTS field coil

This section investigates the electrical and thermal characteristics of MI–SS 2G HTS field coils for the 10 MW class HTS generator used in offshore wind turbine environment. Based on the experimental results of three small–scale MI–SS racetrack coils in section 3.3, the R_{ct} were calculated and applied to the 2G HTS field coils to estimate the R_c. Then, the τ_d and thermal stability of MI–SS 2G HTS field coils were investigated using the proposed equivalent circuit model and the key parameters of 2G HTS field coils of the 10 MW class HTS generator, which was referenced from previous researches [68]–[70]. Finally, the results of three MI–SS 2G HTS field coils were compared and discussed in detail. Table 4.1 shows the design parameters of the three 2G HTS field coils that are used to develop a numerical analysis. The field pole involves eight single racetrack coils with 411, 411, and 419 turns for field coils 1, 2, and 3, respectively. The R_c values of field coils 1, 2, and 3 are 14.06, 37.93, and 35.29 mΩ, respectively, which were calculated using the R_{ct} values from three small–scale MI–SS racetrack coils 1, 2, and 3, respectively, in section 3.3. To compare τ_d and thermal stability, it is assumed that three 2G HTS field coils have the same values of the straight line section and inner radius at the round sections of 1250 and 40 mm, respectively. Field coil 3 is wound with an SS thickness of 0.05 mm, which makes the outer radius and conductor length shorter than those of field coils 1 and 2. The processing design for the simulation approach is illustrated in section 2.3. Here, the center magnetic field in each field coil is determined by 3D FEA based on the I_θ result values from the equivalent circuit model because the equivalent circuit model cannot calculate the magnetic field in iron–core structures, i.e., salient field pole. The I_θ profiles were used in the FEA simulations as field excitations of the 2G HTS field coils.

Table 4.1. Key parameters of three HTS field coils.

Parameters	**Unit**	**Values**		
Field coil types	–	Field coil 1	Field coil 2	Field coil 3
Number of turns*	–	3288	3288	3352
SS thickness	[μm]	100	100	50
Winding tension	[kgf]	10	5	10
Conductor length*	[km]	10.1	10.1	10.1
Conductor width	[mm]	12	12	12
Straight section	[mm]	1250	1250	1250
Inner radius at round section	[mm]	40	40	40
Outer radius at round section	[mm]	142.8	142.8	123.8
Critical current	[A]	305	305	287
Critical voltage	[V]	1.01	1.01	1.01
Temperature operation	[K]	35	35	35
Characteristic resistance	[mΩ]	14.06	37.93	35.29
Contact surface resistance	[μΩ.cm^2]	1577	4256	3809
Coil inductance	[H]	8.71	8.71	8.86

*: for a pole

4.2. Results and discussion

4.2.1. Charging test

In the charging tests for three small–scale MI–SS racetrack coils in section 3.3, a high current ramp rate and current amplitude could generate more joule heat energy in the test coils during the charging tests, leading to a reduction in the thermal stability. Therefore, during the

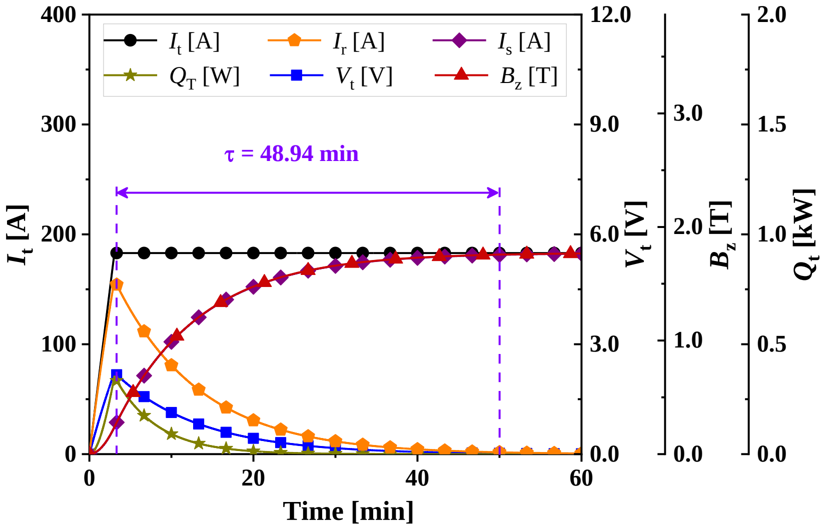

(a) Field coil 1

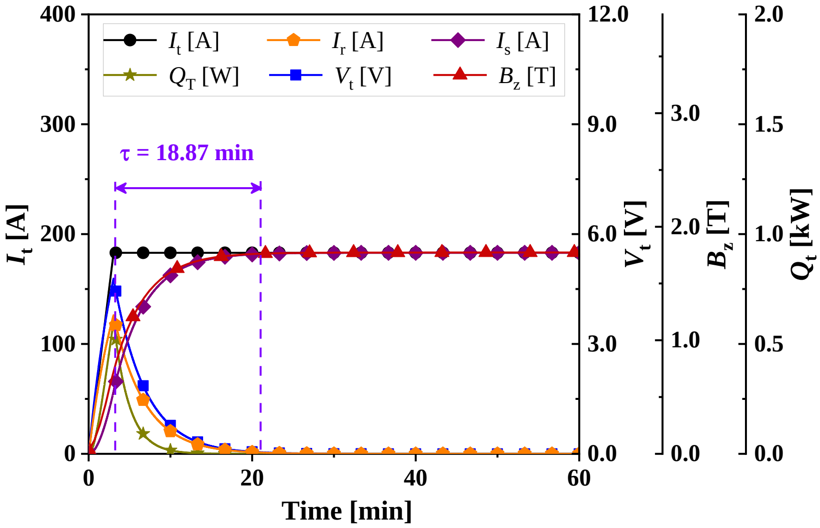

(b) Field coil 2

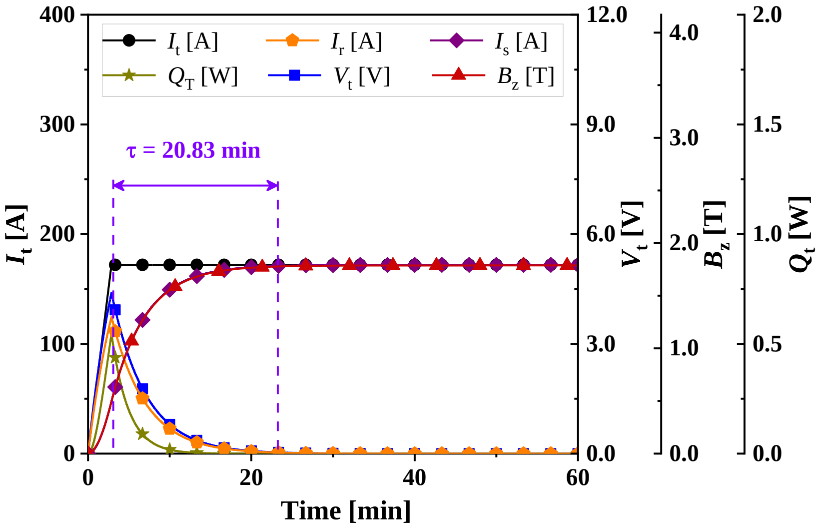

(c) Field coil 3

Fig. 4.1. Charging test at 0.6 I_c with current ramp rate of 1 A/s.

charging tests, I_t is increased to 0.6 I_c (183 A for field coils 1 and 2 and 172 A for field coil 3) with a current ramp rate of 1 A/s and maintained at that level for 1 h; then, I_t is decreased to zero at a current ramp rate of 1 A/s. As shown in Fig. 4.1, B_z of field coils 1, 2, and 3 increases linearly with respect to I_t, finally reaching saturated field values of 1.77, 1.77, and 1.79 T, respectively. Further, B_z of field coil 3 is higher than those of field coils 1 and 2. The τ_d values for field coils 1, 2, and 3 are 48.94, 18.87, and 20.83 min, respectively. As expected, τ_d decreases as the winding tension and SS thickness decreases because of the increased R_{ct} between the turn–to–turn layers. The τ_d values for field coils 2 and 3 are 61.4 % and 57.4% shorter than that of field coil 1, respectively. The results indicate that the decreased winding tension and SS thickness can notably enhance the slow τ_d behavior observed in the MI–SS 2G HTS field coils. Overall, field coil 3 is a promising candidate for 2G HTS field coils of the 10 MW class HTS generator owing to its fast charging time. The fast charging time reduces the setup time and downtime for the rated operation of the wind turbine generator, leading to increased economic efficiency [71], [72]. In addition, the SS tape thickness of 0.05 mm used in field coil 3 can reduce the total HTS conductor length (l_{fc}) compared with the 0.1 mm SS tape thickness used in field coils 1 and 2.

4.2.2. Overcurrent test

In the overcurrent test, I_t increases to 1.2 I_c (366 A for field coils 1 and 2 and 344 A for field coil 3) at a charging rate of 1 A/s and maintained at that level for 1 h; then, I_t decreases to zero at a discharging rate of 1 A/s. Fig. 4.2 shows the overcurrent test results with respect to time for all field coils. The V_t of field coils 1, 2, and 3 initially starts to increase and rapidly reach 3.89, 6.94, and 6.61 V, respectively. When I_t remains at 1.2 I_c, the V_t of field coils 1, 2, and 3 recovered to 0.88, 2.01, and 1.79 V, respectively. The V_t of field coils 2 and 3 are higher than the critical voltage (i.e., $V_c = l_{fc} \times E_c$), implying that quench occurs in these field coils. The recovered voltages of field coils 2 and 3 are 56.2% and 50.8% higher than that of field coil 1. In addition, the maximum heat generations in field coil 2 (2.54 kW) and field coil 3 (2.27 kW)

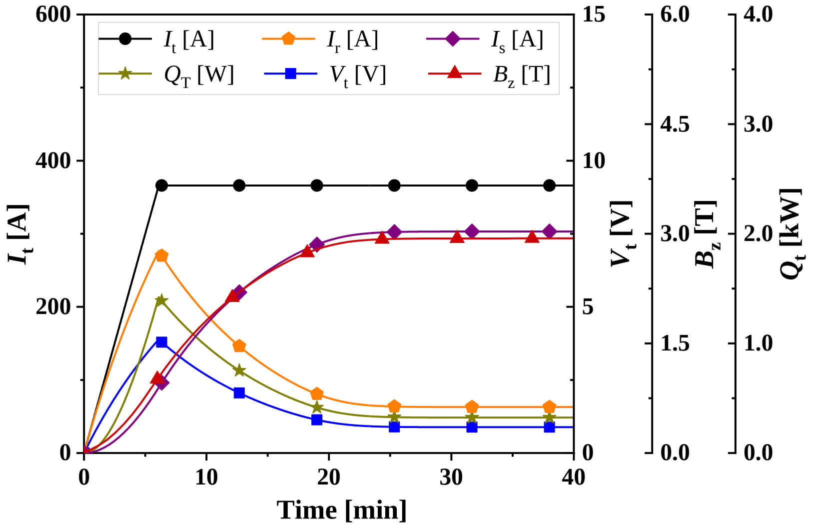

(a) Field coil 1

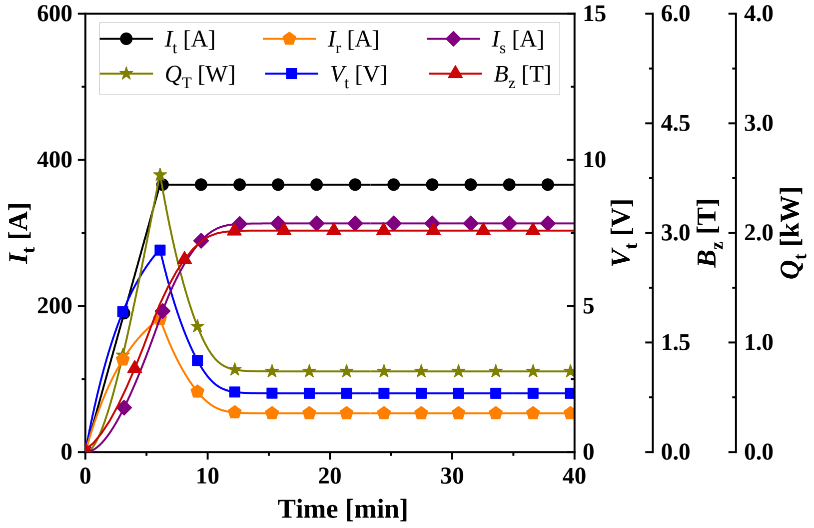

(b) Field coil 2

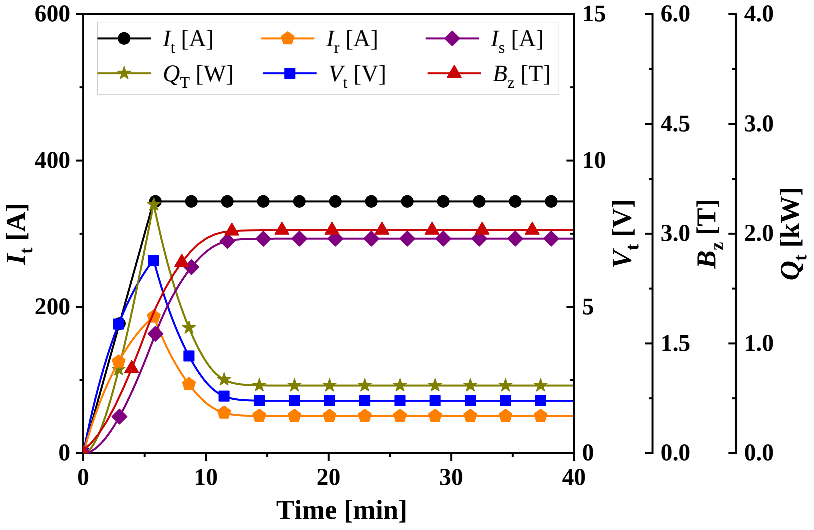

(c) Field coil 3

Fig. 4.2. Overcurrent tests at 1.2 I_c with current ramp rate of 1 A/s.

are higher than that in field coil 1 (1.42 kW). As expected, V_t and Q_T increases with an increase in R_c owing to the limited bypass current through the neighboring turns during the overcurrent test. The results clearly show that field coil 1 exhibits better thermal stability than those of field coils 2 and 3. Although the field coils 2 and 3 showed V_t higher than V_c during the overcurrent test, it is believed that a portion of the excessive current could divert through the SS tape to prevent permanent damage to these field coils.

The effects of winding tension and SS thickness on the electrical characteristics of the MI–SS winding technique employed in 2G HTS field coils of the 10 MW class HTS generator were investigated in this section. The experimental results from three small test coils provided useful references for estimating the electrical characteristics of 2G HTS field coils. Through the experimental analyses, a current ramp rate of 1 A/s and a current amplitude of 0.6 I_c were selected to reduce joule heat generation in 2G HTS field coils of the 10 MW class HTS generator during charging operation. Furthermore, the R_c values of the three field coils were obtained based on the R_{ct} values of the three small test coils. From the equivalent circuit model analyses, the charging test results demonstrated that field coils 2 and 3 can be charged significantly faster than field coil 1. In the transient state at 1.2 I_c, although quench occurred in the HTS field coils 2 and 3, a portion of the bypass current was diverted through adjacent turns to prevent these field coils from being permanently damaged. Overall, the MI–SS winding technique with a 0.05 mm SS tape thickness and 10–kgf winding tension is a highly promising candidate for 2G HTS field coils of the 10 MW class HTS generator owing to its effective economic advantage in terms of the τ_d and HTS conductor required.

Chapter 5. Conclusions

The main objective of this dissertation is to study an effective winding technique according to magnetic field response performance and thermal stability for the development 2G HTS field coils of the 10 MW class HTS generator used in offshore wind power. The advanced simulation approach using the proposed concise equivalent circuit model has been developed to investigate the τ_d and thermal stability for the HTS coils in the steady and transient states, respectively. The simulation results were in good agreement with the experimental ones under all test conditions, indicating that the simulation approach is verified. In addition, the MI–SS winding technique exhibited a good balance in terms of τ_d and thermal stability compared with NI winding technique, especially in large–scale HTS generator. The charging test results demonstrated that the MI–SS coil could considerably improve the slow τ_d characteristic in the NI coil due to increasing the R_c between turn–to–turn layers. Although the NI coil showed higher thermal stability than that of MI–SS coil during the transient state, the MI–SS coil operated successfully in the overcurrent test due to the bypass current phenomenon. The excessive current could be automatically diverted through the stainless steel tape to protect the MI–SS racetrack coil from permanent damage. Further, the effects of current ramp rate, current amplitude, winding tension, and SS thickness between turn-to-turn layers were investigated to select a suitable MI–SS winding technique for 2G HTS field coils of the 10 MW class HTS generator, as shown in section 3.3. Thus, the following factors (1)–(4) should be considered to optimize the performance in steady–state and transient–state operations for the MI–SS 2G HTS field coils. Moreover, the MI–SS racetrack coil was also tested under rotating magnetic field and conduction cooling system to estimate the electrical and thermal characteristics, as shown in section 3.4. Based on the test results, the following considerations (5)–(7) should be given to ensure stable operation for the MI–SS 2G HTS field coils, which can be subjected to external magnetic field in practical wind generator application.

(1) In the charging tests, the winding tension and SS insulation thickness strongly influenced τ_d of the test coils, and τ_d increased with increasing SS insulation thickness and winding tension.

(2) The effects of the SS thickness resistance on the R_{ct} of the MI–SS coil are less critical than those of the contact surface roughness feature between HTS and SS tapes due to the small resistivity of stainless steel material at 77 K.

(3) τ_d was also affected by the current ramp rate and current amplitude during the charging tests. At the same I_t, τ_d of the test coils decreased as the current ramp rate decreased because of the decreased I_r flowing through the turn–to–turn layers. However, at the same current ramp rate, τ_d decreased with increasing I_t because of the increased contact surface resistance, which could be caused by more joule heat energy generated within the test coils at high I_t. The test coil exhibited a high V_t with respect to a high current ramp rate and high current amplitude during the charging test, which could cause less stable operation.

(4) During the overcurrent tests, the test coil with a higher winding tension and thicker SS insulation exhibited greater thermal stability than the other coils. This was because the joule heat energy induced by the overcurrent could be dissipated effectively with increasing winding tension. Similarly, the thicker SS insulation could enhance the heat capacity, which absorbed more joule heat energy generated by hot spots. Overall, increasing the SS insulation thickness and winding tension could be an effective approach for improving the thermal stability of the MI–SS winding technique.

(5) At the same temperature cooling of 77 K, the R_c under LN2 was smaller than that of conduction cooling system, leading to the decreased joule heat generation, which resulted in an improvement thermal stability for the test coil.

(6) The test coil under conduction cooling system of 35 K exhibited superior electrical and thermal stabilities due to its efficiency in eliminating joule heat generation during the tests.

(7) When the test coil was exposed to AC rotating magnetic field, the I_c value decreased with increasing current amplitude and frequency of the three phase armature windings,

resulting in decreased electrical and thermal stabilities of the test coil.

Overall, these results could be effectively utilized as a technical reference for the design of future 2G HTS field coils of the 10 MW class HTS generator used in the offshore wind power environment.

REFERENCES

[1] S. S. Kalsi, *Applications of high temperature superconductors to electric power equipment*, Wiley–IEEE Press, 2011.

[2] Y. Iwasa, *Case studies in superconducting magnets–design and operational issues*, 2nd edition, New York: Springer, 2009.

[3] Z. Melhem, *High temperature superconductors (HTS) for energy applications*, Woodhead Publishing Limited, 2012.

[4] Y. Wang, *Fundamental elements of applied superconductivity in electrical engineering*, Wiley, 2013.

[5] I. A. Parinov, *Microstructure and properties of high–temperature superconductors*, 2nd edition, New York: Springer, 2013.

[6] O. Keysan and M. A. Mueller, "A homopolar HTSG topology for large direct–drive wind turbines," *IEEE Trans. Appl. Supercond.*, vol. 21, no. 5, Oct. 2011.

[7] G. Snitchler, B. Gamble, C. King, and P. Winn, "10 MW class superconductor wind turbine generators," *IEEE Trans. Appl. Supercond.*, vol. 21, no. 3, pp. 1089–1092, Jun. 2011.

[8] R. Shafaie and M. Kalantar, "Design of a 10–MW–class wind turbine HTS synchronous generator with optimized field winding," *IEEE Trans. Appl. Supercond.*, vol. 23, no. 4, Aug. 2013.

[9] J. H. Kim and H. M. Kim, "Electromagnetic design of 10 MW class superconducting wind turbine using 2G HTS wire," *Prog. Supercond. Cryog.*, vol. 15, no. 3, Sep. 2013.

[10] Y. Xu, N. Maki, and M. Izumi, "Electrical design study of 10–MW salient–pole wind turbine HTS synchronous generators," *IEEE Trans. Appl. Supercond.*, vol. 24, no. 6, Dec. 2014.

[11] B. S. Go *et al.*, "Design and comparative analysis of performance evaluation systems for a large–scale HTS generator," *IEEE Trans. Appl. Supercond.*, vol. 29, no. 5, Apr. 2019.

[12] Y. S. Chae *et al.*, “Design and analysis of HTS rotor–field coils of a 10–MW–class HTS generator considering various electric insulation techniques,” *IEEE Trans. Appl. Supercond.*, vol. 30, no. 4, Jun. 2020.

[13] S. Fukui *et al.*, “Study of 10 MW–class wind turbine synchronous generators with HTS field windings,” *IEEE Trans. Appl. Supercond.*, vol. 21, no. 3, Jun. 2011.

[14] Y. Xu, N. Maki, and M. Izumi, “Performance comparison of 10–MW wind turbine generators with HTS, copper, and PM excitation,” *IEEE Trans. Appl. Supercond.*, vol. 25, no. 6, Dec. 2015.

[15] H. J. Sung, B. S. Go, and M. Park, “A performance evaluation system of an HTS pole for large–scale HTS wind power generations,” *IEEE Trans. Appl. Supercond.*, vol. 29, no. 5, Aug. 2019.

[16] H. J. Sung *et al.*, “Design of a 12–MW HTS wind power generator including a flux pump exciter,” *IEEE Trans. Appl. Supercond.*, vol. 26, no. 3, Apr. 2016.

[17] J. Lloberas, “Finite–element analysis of a 15–MW high–temperature superconductor synchronous generator for offshore wind energy application,” *IEEE Trans. Appl. Supercond.*, vol. 25, no. 6, Dec. 2015.

[18] J. Pelegrín, E. Martínez, L. A. Angurel, Y. –Y. Xie, and V. Selvamanickam, “Numerical and experimental analysis of normal zone propagation on 2G HTS wires,” *IEEE Trans. Appl. Supercond.*, vol. 21, no. 3, Jun. 2011.

[19] F. Trillaud *et al.*, “Normal zone propagation experiments on HTS composite conductors,” *Cryogenics*, vol. 43, pp. 271–279, Apr. 2003.

[20] W. S. Kim, F. Trillaud, I. C. Ang, S. Hahn, and Y. Iwasa, “Normal zone propagation in YBCO winding pack models,” *IEEE Trans. Appl. Supercond.*, vol. 17, no. 2, Jun. 2007.

[21] W. S. Kim *et al.*, “Normal zone propagation in 2–dimensional YBCO winding pack models,” *IEEE Trans. Appl. Supercond.*, vol. 18, no. 2, Jun. 2008.

[22] S. Hahn, D. K. Park, J. Bascuñán, and Y. Iwasa, “HTS pancake coils without turn–to–turn insulation,” *IEEE Trans. Appl. Supercond.*, vol. 21, no. 3, pp. 1592–1595, Jun. 2011.

[23] S. Noguchi, K. Monma, H. Igarashi, and A. Ishiyama, “Investigation of current flow between turns of NI REBCO pancake coil by 2–D finite–element method,” *IEEE Trans. Appl. Supercond.*, vol. 26, no. 3, Apr. 2016.

[24] Y. G. Kim *et al.*, “Numerical analysis on bifurcated current flow in no–insulation magnet,” *IEEE Trans. Appl. Supercond.*, vol. 24, no. 3, Jun. 2014.

[25] S. Choi, H. C. Jo, Y. J. Hwang, S. Hahn, and T. K. Ko, “A study on the no insulation winding method of the HTS coil,” *IEEE Trans. Appl. Supercond.*, vol. 22, no. 3, Jun. 2012.

[26] X. Wang *et al.*, “Turn–to–turn contact characteristics for an equivalent circuit model of no–insulation ReBCO pancake coil,” *Supercond. Sci. Technol.*, vol. 26, no. 3, Jan. 2013.

[27] H. L. Quach *et al.*, “Analysis on electrical and thermal characteristics of a no–insulation HTS coil considering heat generation in steady and transient states,” *IEEE Trans. Appl. Supercond.*, vol. 29, no. 5, Aug. 2019.

[28] H. L. Quach *et al.*, “Analytical and numerical simulation on charging behavior of no–insulation REBCO pancake coil,” *Prog. Supercond. Cryog.*, vol. 20, no. 4, pp. 16–19, Dec. 2018.

[29] X. Wang *et al.*, “Charging behavior in no–insulation REBCO pancake coils,” *IEEE Trans. Appl. Supercond.*, vol. 25, no. 3, Jun. 2015.

[30] Z. Zhang *et al.*, “An experimental investigation of the transient response of HTS non–insulation coil,” *J. Supercond. Nov. Magn.*, vol. 30, no. 2, pp. 387–393, Feb. 2017.

[31] T. Wang *et al.*, “Analyses of transient behaviors of no–insulation REBCO pancake coils during sudden discharging and overcurrent,” *IEEE Trans. Appl. Supercond.*, vol. 29, no. 5, Aug. 2019.

[32] Y. Wang *et al.*, “Study on no–insulation HTS pancake coils with iron core for superconducting DC induction heaters,” *IEEE Trans. Appl. Supercond.*, vol. 25, no. 3, Jun. 2015.

[33] K. R. Bhattarai, K. Kim, S. Kim, S. Lee, and S. Hahn, “Quench analysis of a multiwidth no–insulation 7–T 78–mm REBCO magnet,” *IEEE Trans. Appl. Supercond.*, vol. 27, no. 4, Jun. 2017.

[34] K. L. Kim *et al.*, “Analytical and empirical studies on the characteristic resistances of no–insulation GdBCO racetrack pancake coil under various operating currents,” *Current. Appl. Phys.*, vol. 15, no. 1, pp. 8–13, Jan. 2015.

[35] T. Oki *et al.*, “Evaluation on quench protection for no–insulation REBCO pancake coil,” *IEEE Trans. Appl. Supercond.*, vol. 26, no. 4, Jun. 2016.

[36] S. Noguchi *et al.*, “Experiment and simulation of impregnated no–insulation REBCO pancake coil,” *IEEE Trans. Appl. Supercond.*, vol. 26, no. 4, Jun. 2016.

[37] Y. Li *et al.*, “Feasibility study of the impregnation of a no–insulation HTS coil using solder,” *IEEE Trans. Appl. Supercond.*, vol. 28, no. 1, Jan. 2018.

[38] Y. H. Choi *et al.*, “Partial insulation of GdBCO single pancake coils for protection–free HTS power applications,” *Supercond. Sci. Technol.*, vol. 24, no. 12, Nov. 2011.

[39] Y. H. Choi *et al.*, “The effects of partial insulation winding on the charge–discharge rate and magnetic field loss phenomena of GdBCO coated conductor coils,” *Supercond. Sci. Technol.*, vol. 25, no. 10, Jul. 2012.

[40] D. G. Yang, Y. H. Choi, Y. G. Kim, J. B. Song, and H. G. Lee, “Analytical and experimental investigation of electrical characteristics of a metallic insulation GdBCO coil,” *Rev. Sci. Instrum.*, vol. 87, no. 3, Feb. 2016.

[41] D. H. Kang *et al.*, “Investigation of thermal and electrical stabilities of a GdBCO coil using grease as an insulation material for practical superconducting applications,” *Rev. Sci. Instrum.*, vol. 85, no. 9, Sep. 2014.

[42] H. L. Quach and H. M. Kim, “A study on charging and electrical stability characteristics with no–insulation and metal insulation in form of racetrack type coils,” *Prog. Supercond. Cryog.*, vol. 22, no. 3, pp. 13–19, Sep. 2020.

[43] 2G HTS wire architecture. [Online] Available: http://www.i-sunam.com/wp/sunam1-2/

[44] Y. G. Kim, S. Hahn, K. L. Kim, O. J. Kwon, and H. Lee, “Investigation of HTS racetrack coil without turn–to–turn insulation for superconducting rotating machines,” *IEEE Trans. Appl. Supercond.*, vol. 22, no. 3, Jun. 2012.

[45] D. G. Yang, Y. H. Choi, D. H. Kang, Y. J. Park, H. G. Lee, “Effect of partial insulation winding scheme on discharge characteristics of GdBCO coils,” *Current. Appl. Phys.*, vol. 15, no. 2, pp. 156–162, Feb. 2015.

[46] S. Kim, H. Okusa, K. Tami, and H. Ueda, “Current bypassing and transient stability in a partially insulated HTS coil,” *IEEE Trans. Appl. Supercond.*, vol. 8, no. 3, Apr. 2018.

[47] J. Kim *et al.*, “Effect of resistive metal cladding of HTS tape on the characteristic of no–insulation coil,” *IEEE Trans. Appl. Supercond.*, vol. 26, no. 4, Jun. 2016.

[48] K. Kim *et al.*, “Quench behavior of a no–insulation coil wound with stainless steel cladding REBCO tape at 4.2 K,” *Supercond. Sci. Technol.*, vol. 30, no. 7, May. 2017.

[49] J. Kim *et al.*, “A study on the electrical characteristics of metal–clad GdBCO coils,” *IEEE Trans. Appl. Supercond.*, vol. 28, no. 3, Apr. 2018.

[50] T. S. Lee *et al.*, “The effects of co-wound kapton, stainless steel and copper, in comparison with no insulation, on the time constant and stability of GdBCO pancake coils,” *Supercond. Sci. Technol.*, vol. 27, no. 6, May. 2014.

[51] Y. Wang *et al.*, “Analysis and comparison between no–insulation and metallic insulation REBCO magnet for the engineering design of a 1–MW DC induction heater,” *IEEE Trans. Appl. Supercond.*, vol. 27, no. 4, Jun. 2017.

[52] M. H. Sohn *et al.*, “Controllability of the contact resistance of 2G HTS coil with metal insulation,” *IEEE Trans. Appl. Supercond.*, vol. 28, no. 3, Apr. 2018.

[53] S. Noguchi, R. Miyao, K. Monma, H. Igarashi, and A. Ishiyama, “Numerical investigation of metal insulation technique on turn–to–turn contact resistance of REBCO pancake coils,” *IEEE Trans. Appl. Supercond.*, vol. 27, no. 4, Jun. 2017.

[54] Y. G. Kim *et al.*, "Investigation on quench initiation and propagation characteristics of GdBCO coil co–wound with a stainless steel tape as turn–to–turn metallic insulation," *Rev. Sci. Instrum.*, vol. 87, no. 11, Jul. 2016.

[55] H. L. Quach *et al.*, "Effects of stainless steel thickness and winding tension on electrical and thermal characteristics of metal insulation racetrack coils for 10–MW–class HTS wind generator," *Cryogenics*, vol. 115, Apr. 2021.

[56] J. D. Logan, *A first course in differential equations*, 3rd edition, Springer, Mar. 2015.

[57] S. Ahmad and A. Ambrosetti, *A textbook on ordinary differential equations*, 2nd edition, Springer, Jan. 2015.

[58] W. Y. Yang, W. Cao, T–S. Chung, J. Morris, *Applied numerical methods using MATLAB*, John Wiley & Sons, Jan. 2015.

[59] C. Woodford and C. Phillips, *Numerical methods with worked examples: MATLAB edition*, 2nd edition, Springer, Sep. 2011.

[60] A. Ikeda *et al.*, "Transient behaviors of no–insulation REBCO pancake coil during local normal–state transition," *IEEE Trans. Appl. Supercond.*, vol. 26, no. 4, Jun. 2016.

[61] K. Katsumata *et al.*, "Influence of the turn–to–turn contact electrical resistance on the thermal stability in meter–class no–insulation REBCO pancake coils during a local normal–state transition," *IEEE Trans. Appl. Supercond.*, vol. 27, no. 4, Jun. 2017.

[62] Y. Kakimoto *et al.*, "Evaluation of electromagnetic behavior of no–insulation REBCO pancake coil with multiple defects," *IEEE Trans. Appl. Supercond.*, vol. 29, no. 5, Aug. 2019.

[63] O. J. Kwon *et al.*, "Effects of turn–to–turn compactness in the straight sections of HTS racetrack coils on thermal and electrical characteristics," *Supercond. Sci. Technol.*, vol. 26, no. 8, Jul. 2013.

[64] S–G. Kim *et al.*, "Charge–discharge and thermal–electrical characteristics of GdBCO coils wound with various types of grease as an insulation material," *IEEE Trans. Appl. Supercond.*, vol. 26, no. 4, Feb. 2016.

[65] J–B. Song *et al.*, “Thermal and electrical properties of thermal–grease–insulated REBCO superconducting coils with respect to winding tension,” *Met. Mater. Int.*, Sep. 2017.

[66] D. G. Yang *et al.*, “A study on electrical characteristics of multilayered metallic–insulation coils,” *IEEE Trans. Appl. Supercond.*, vol. 27, no. 4, Jun. 2017.

[67] K. L. Kim *et al.*, “Effect of winding tension on electrical behaviors of a no-insulation ReBCO pancake coil,” *IEEE Trans. Appl. Supercond.*, vol. 24, no. 3, Jun. 2014.

[68] J. H. Kim *et al.*, “3D electromagnetic design and electrical characteristics analysis of a 10–MW–class high–temperature superconducting synchronous generator for wind power,” *Prog. Supercond. Cryog.*, vol. 16, no. 2, Jun. 2014.

[69] J. H. Kim *et al.*, “Characteristic analysis of various structural shapes of superconducting field coils,” *IEEE Trans. Appl. Supercond.*, vol. 25, no. 3, Jun. 2015.

[70] J. H. Kim, “3D electromagnetic design and power analysis of a 10–MW–class high–temperature superconducting synchronous generator for wind power,” M. S. thesis in Jeju National University, Dec. 2013.

[71] S. Faulstich, B. Hahn, and P. J. Tavner, “Wind turbine downtime and its importance for offshore deployment,” *Wind energy*, vol. 14, no. 3, Apr. 2011.

[72] S. Pfaffel, S. Faulstich, and K. Rohrig, “Performance and reliability of wind turbines: A review,” *Energies*, vol. 10, no. 11, Nov. 2017.

CURRICULUM VITAE

Huu Luong Quach

Applied Superconductivity Laboratory

Department of Electrical Engineering

Jeju National University

I. EDUCATION

[1] Sep. 2004 – Sep. 2008

B.S. in Department of Electrical Engineering

Can Tho University, Viet Nam

[2] Sep. 2011 – Sep. 2013

M.S. in Department of Power Systems Engineering

Ho Chi Minh City University of Technology, Viet Nam

[3] Mar. 2017 – Mar. 2022

Ph. D. in Department of Electrical Engineering

Jeju National University, Republic of Korea

II. PUBLICATIONS

International papers (SCI)

[1] J. H. Kim, C. J. Hyeon, **H. L. Quach**, S. H. Chae, J. Lee, H. Jeon, S. Han, T. K. Ko, Y. S. Yoon, H. W. Kim, Y. S. Jo, and H. M. Kim, "Characteristic analysis of a 1–kw–class HTS motor considering armature current information," *IEEE Trans. Appl. Supercond.*, vol. 28, no. 4, Jun. 2018.

[2] C. J. Hyeon, J. H. Kim, **H. L. Quach**, H. W. Kim, S. W. Kim, Y. S. Jo, and H. M. Kim, "Quench behavior of 2G HTS coils with polyimide film and MIT material under over pulse–current," *IEEE Trans. Appl. Supercond.*, vol. 28, no. 4, Jun. 2018.

[3] **H. L. Quach**, J. H. Kim, Y. S. Chae, J. H. Moon, J. H. Ko, S. H. Chae, J. H. Ahn, E. H. Kim, S. H. Kim, Y. G. Jin, H. W. Kim, Y. S. Jo, and H. M. Kim, "Analysis on electrical and thermal characteristics of a no–insulation HTS coil considering heat generation in steady and transient states," *IEEE Trans. Appl. Supercond.*, vol. 29, no. 5, Aug. 2019.

[4] J. H. Kim, **H. L. Quach**, C. J. Boo, Y. S. Yoon, H. Jeon, S. Han, T. K. Ko, H. W. Kim, Y. S. Jo, H. J. Park, J. Lee, H. Lee, and H. M. Kim, "Fabrication and charging test of HTS field windings using HTS contactless rotary excitation device," *IEEE Trans. Appl. Supercond.*, vol. 29, no. 5, Aug. 2019.

[5] **H. L. Quach**, J. H. Kim, C. J. Hyeon, Y. S. Chae, J. H. Moon, C. J. Boo, H. W. Kim, Y. S. Jo, S. W. Kim, and H. M. Kim, "Electrical and thermal analyses of a second generation high temperature superconducting magnet with vanadium III oxide and Kapton polyimide film insulation materials under an over–pulse current," *Supercond. Sci. Technol.*, vol. 32, no. 6, May 2019.

[6] J. H. Kim, C. J. Hyeon, **H. L. Quach**, S. H. Chae, Y. S. Chae, J. H. Moon, C. J. Boo, Y. S. Yoon, J. Lee, H. Jeon, S. Han, Y. G. Kim, H. Lee, and H. M. Kim, "Design, analysis, and fabrication of salient field–pole for a 1–kW–class HTS rotating machine," *Cryogenics*, vol. 97, pp. 126–132, Jan. 2019.

[7] T. D. Le, R. Noumeir, **H. L. Quach**, J. H. Kim, J. H. Kim, and H. M. Kim, "Critical temperature prediction for a superconductor: a variational bayesian neural network approach," *IEEE Trans. Appl. Supercond.*, vol. 30, no. 4, Jun. 2020.

[8] Y. S. Chae, J. H. Kim, **H. L. Quach**, J. H. Moon, H. J. Sung, C. Kim, B. S. Go, M. Park, Y. C. Kim, H. W. Kim, Y. S. Jo, and H. M. Kim, "Design and analysis of HTS rotor–field coils of a 10–MW–class HTS generator considering various electric insulation techniques," *IEEE Trans. Appl. Supercond.*, vol. 30, no. 4, Jun. 2020.

[9] J. H. Kim, Y. S. Chae, **H. L. Quach**, Y. S. Yoon, H. Jeon, S. Han, T. K. Ko, J. Lee, H. W. Kim, Y. S. Jo, H. J. Park, and H. M. Kim, "Frabrication and performance testing of a 1–kW–class high–temperature superconducting generator with a high–temperature superconducting contactless field exciter," *Supercond. Sci. Technol.*, vol. 33, no. 9, Jul. 2020.

[10] **H. L. Quach**, Y. S. Chae, J. H. Kim, J. H. Hong, Y. S. Yoon, and H. M. Kim, "Effects of stainless steel thickness and winding tension on electrical and thermal characteristics of metal insulation racetrack coils for 10–MW–class HTS wind generator," *Cryogenics*, vol. 115, Apr. 2021.

International papers (SCOPUS)

[1] T. D. Le, J. H. Kim, C. J. Hyeon, D. K. Kim, Y. S. Yoon, J. Lee, Y. G. Park, H. Jeon, **H. L. Quach**, and H. M. Kim, "A compactly integrated cooling system of a combination dual 1.5–MW HTS motors for electric propulsion." *Prog. Supercond. Cryog.*, vol. 18, no. 4, pp. 25–29, Dec. 2016.

[2] C. J. Hyeon, J. H. Kim, **H. L. Quach**, S. H. Chae, Y. S. Yoon, J. Lee, S. H. Han, H. Jeon, Y. H. Choi, H. G. Lee, and H. M. Kim, "Conceptual design of cooling anchor for current lead on HTS field coils," *Prog. Supercond. Cryog.*, vol. 19, no. 2, pp. 38–43, Jun. 2017.

[3] J. H. Kim, C. J. Hyeon, **H. L. Quach**, Y. S. Chae, J. H. Moon, C. J. Boo, and H. M. Kim, "Conceptual design and analysis of rotor for a 1–kW–Class HTS rotating machine," *Prog. Supercond. Cryog.*, vol. 19, no. 4, pp. 45–50, Dec. 2017.

[4] **H. L. Quach**, J. H. Kim, C. J. Hyeon, Y. S. Chae, J. H. Moon, and H. M. Kim, "Investigation on stability characteristics of 2G HTS coated conductor tapes with various stabilizer thickness," *Prog. Supercond. Cryog.*, vol. 20, no. 1, pp. 11–14, Mar. 2018.

[5] **H. L. Quach**, J. H. Kim, Y. S. Chae, J. H. Moon, J. H. Ko, H. W. Kim, S. W. Kim, Y. S. Jo, and H. M. Kim, "Analytical and numerical simulation on charging behavior of no–insulation REBCO pancake coil," *Prog. Supercond. Cryog.*, vol. 20, no. 4, pp. 16–19, Dec. 2018.

[6] **H. L. Quach** and H. M. Kim, "A study on charging and electrical stability characteristics with no–insulation and metal insulation in form of racetrack type coils," *Prog. Supercond. Cryog.*, vol. 22, no. 3, pp. 13–19, Sep. 2020.

III. AWARDS

The outstanding paper awards

[1] "Development trends of large scale HTS generators for wind turbine" at 2017 Autumn Conference on Korea Wind Energy Association organized by Korea Wind Energy Association (KWEA).

[2] "Core Technology Development of Superconducting Generator for Wind Turbine" at 2021 Spring Conference on the Korean Society of Mechanical Engineers (KSME).